UNIVERSITY OF TRENTO

Giulia Giuliani

Experimental and numerical analysis of steel frames equipped with repairable dissipative seismic components

October 2023 - Doctoral thesis

Giulia Giuliani

Experimental and numerical analysis of steel frames equipped with repairable dissipative seismic components

Supervisors

Associate Professor, PhD Nicola Tondini, University of Trento
Full Professor, PhD Oreste S. Bursi, University of Trento

Credits of the cover image DISSIPABLE project

*"Ciao Papà, ce l'ho fatta!
Ho fatto un dottorato, come ti avevo detto
fin dal primo giorno di Università.
Grazie per essere stato custode del
mio sogno più grande."*

"Mens Dominatus Potentia"

Ringraziamenti

Questi ringraziamenti sono divisi in cinque parti:

- a tutti i docenti che ho incontrato negli anni di formazioni, che hanno saputo accendere in me la volontà di domandarsi il "perché" prima del "come", la curiosità nei confronti dell'ingengeria, e la passione per la ricerca. Non ultimi il prof. Oreste S. Bursi, per i consigli forniti negli anni, l'ing. Alessio Bonelli, che mi ha accompagnato dalla tesi magistrale fino all'ultimo lavoro del dottorato ed il mio supervisore il prof. Nicola Tondini, che mi ha dato l'opportunità di fare davvero ricerca, insieme hanno saputo tenere sempre viva la sete della comprensione e la fame della conoscenza.

- alle persone che mi sono state a fianco in questi anni, per il sostegno, la pazienza e l'affetto dimostratomi. Grazie a Roberto, per le infinite discussioni tecnico-personali che mi hanno fatto crescere, maturare e imparare a difendere le mie posizioni quando le ritenevo giuste. A Rocco, per essere l'amico inaspettato di cui non pensavo di aver bisogno. Grazie a Fabrizio, per le chiacchierate, le risate e il confronto fatto di audio eterni. A Chiara e Sara, per essere amiche e confidenti prima di colleghe. Ai tecnici di laboratorio, Tiziano, Luca e Ivan, che hanno reso divertenti le lunghe giornate in laboratorio, portando calore e colore in un ambiente grigio.

- alla mia famiglia e agli amici di sempre. Grazie per esserci stati, grazie per essere rimasti, grazie per essere il mio porto sicuro a cui posso sempre tornare.

- a Luca e Luna. A Luna, per ricordarmi ogni giorno cosa è veramente importante. A Luca, per aver intrapreso con me l'avventura più grande, il viaggio di una vita in amore e condivisione.

- ed a me, per aver coronato un sogno, vivendo a pieno l'esperienza del dottorato con passione, impegno e dedizione. Grazie per essermi dimostrata ancora una volta che ce la posso fare.

Acknowledgements

These acknowledgements are divided into five parts:

- To all the teachers I have encountered during my years of education, who have ignited in me the willingness to ask "why" before "how," the curiosity for engineering, and a passion for research. In particular, I would like to thank Prof. Oreste S. Bursi for the advice provided over the years, Ing. Alessio Bonelli, who has accompanied me from my master's thesis to the final work of my PhD, and my supervisor Prof. Nicola Tondini, who has allowed me to engage in research. Together, they have always kept alive my thirst for understanding and hunger for knowledge.

- To those who have been by my side during these years, I express my gratitude for their support, patience, and affection. Thank you to Roberto, for the countless technical and personal discussions that have helped me grow, mature, and learn to defend my positions when I believed them to be right. To Rocco, for being the unexpected friend I didn't realize I needed. Thanks to Fabrizio, for the chats, laughter, and everlasting audio conversations. To Chiara and Sara, for being friends and confidants before colleagues. To the laboratory technicians, Tiziano, Luca, and Ivan, who made the long days in the lab enjoyable, bringing warmth and colour to a grey environment.

- To my family and lifelong friends, thanks for being there, thanks for staying, thanks for being the safe haven I can always return to.

- To Luca and Luna. To Luna, for reminding me every day what is truly important. To Luca, for embarking with me on the greatest adventure, the journey of a lifetime in love and understanding.

- And to myself, for fulfilling a dream and embracing the PhD experience with passion, commitment, and dedication. I thank myself for proving once again that I can do it.

Publications

Journal Papers

- **Giuliani, G.**, Andreotti, R., & Tondini, N. (2023). *"Pseudo-dynamic hybrid tests on a steel frame equipped with dissipative coupled shear walls"*. Bulletin of Earthquake Engineering. To be submitted.

- **Giuliani, G.**, Andreotti, R., Bonelli, A., & Tondini, N. (2023). *"Hybrid simulation on steel frames equipped with dissipative replaceable link frame with High-Strength Steel beams"*. Engineering Structures. To be submitted.

- **Giuliani, G.**, Bonelli, A., & Tondini, N. (2023). *"Numerical and experimental validation of a novel force correction method for hybrid simulation applied to the partitioned G-α algorithm"*. Earthquake Engineering and Structural Dynamics. To be submitted.

- Andreotti, R., **Giuliani, G.**, & Tondini, N. (2023). *"Experimental analysis of a full-scale steel frame with replaceable dissipative connections"*. Journal of Constructional Steel Research, 208: 108036. DOI: 10.1016/j.jcsr.2023.108036.

- Andreotti, R., **Giuliani, G.**, Tondini, N., & Bursi, O. S. (2023). *"Hybrid simulation of a partial-strength steel–concrete composite moment-resisting frame endowed with hysteretic replaceable beam splices"*. Earthquake Engineering & Structural Dynamics, 52(1), 51-70. DOI: 10.1002/eqe.3744.

Conference Papers

- Andreotti, R., **Giuliani, G.**, Tondini, N., & Bursi, O.S. (2021). *"Dynamic Substructuring Tests Of Steel Frames Equipped With*

Easily Repairable Dissipative Seismic Devices". Proceedings of: 17WCEE, Sendai, 27th September - 2nd October 2021.

- Andreotti, R., **Giuliani, G.**, Tondini, N., & Bursi, O.S. (2021). *"Experimental Investigation of Steel Frames Equipped with Easily Replaceable Components"*. Proceedings of: The 9th European Conference on Steel and Composite Structures, Eurosteel 2020. ce/papers, 4(2-4), 1881-1886. DOI:10.1002/cepa.1499.

- Mattei, F., **Giuliani, G.**, Andreotti, R., Caprili, S., & Tondini, N. (2023). *"Experimental and numerical assessment of a steel frame equipped with Dissipative Replaceable Bracing Connections"*. Proceedings of: XIX ANIDIS Conference, Seismic Engineering in Italy. Procedia Structural Integrity, 44, 1204-1211. DOI: 10.1016/j.prostr.2023.01.155.

- **Giuliani, G.**, Andreotti, R., Tondini, N., & Bonelli, A. (2022). *"Experimental investigation of composite moment resisting frames equipped with dissipative replaceable beam splices"*. Proceedings of the Third European Conference on Earthquake Engineering and Seismology - 3ECEES: September 5-September 9, 2022, Bucharest, Romania, pp 2037-2043.

- Andreotti, R., **Giuliani, G.**, Tondini, N., & Bursi, O.S. (2022). *"Experimental investigation of braced steel frames equipped with dissipative replaceable connections"*. Proceedings of the Third European Conference on Earthquake Engineering and Seismology - 3ECEES: September 5-September 9, 2022, Bucharest, Romania, pp 2105-2110.

- **Giuliani, G.**, Andreotti, R., Tondini, N., & Bursi, O. S. (2022). *"Seismic Fragility Curves of Steel Frames Equipped with Easily Repairable Dissipative Devices"*. Proceedings of: The International Colloquium on Stability and Ductility of Steel Structures, SDSS 2022. ce/papers, 5(4), 720-728. DOI: 10.1002/cepa.1812.

- **Giuliani, G.**, Andreotti, R., Tondini, N., & Bonelli, A. (2022). *"Experimental Investigation of Steel Frames Equipped with Dissipative Replaceable Links"*. Proceedings of: The International Colloquium on Stability and Ductility of Steel Structures, SDSS 2022. ce/papers, 5(4), 714-719. DOI: 10.1002/cepa.1811.

Abstract

The conventional design of buildings in seismic zones entrusts energy
dissipation to the structural elements. The capacity design, adopted in the
main national and international design standards, ensures that the forma-
tion of plastic hinges occurs at specific points of the structure to facilitate
a ductile collapse mechanism. Although this strategy allows for design-
ing structures capable of dissipating energy under seismic loading, they
do not guarantee ease of repair after an earthquake, resulting in a long
downtime/business interruption of the structure. Moreover, buildings de-
signed according to these approaches may undergo significant damage,
whose repair work is often not feasible or too expensive. Therefore, re-
ducing damage to structural and non-structural elements after a disaster
is fundamental for costs and functionality.

The work presented in this thesis was developed in the framework
of the project DISSIPABLE, funded by the European Research Fund of
Coal and Steel (RFCS). The project was funded to perform large demon-
stration tests on steel frames equipped with easily repairable seismic dis-
sipative devices, aiming to demonstrate their effectiveness in mitigating
seismic hazard and their ease of substitution/repair. The tested frames
were equipped with three innovative components, namely the dissipative
replaceable link frame (DRLF), the dissipative replaceable beam splices
(DRBeS) and the dissipative replaceable braced connections (DRBrC).
In order to fully characterize the seismic behaviour, the tests were con-
ducted at three limit states of increasing intensity, i.e. damage limitation
(DL), significant damage (SD) and near collapse (NC). Hybrid simula-
tion (HS) and the substructuring technique were exploited, allowing for
reduced experimental costs by testing only part of a full structure yet
providing meaningful and accurate results. Six-storey full-scale frames
were investigated by physically realizing only their first floors and nu-
merically simulating the remainder of the structure, ensuring compat-
ibility between the parts by controlling the displacements and imple-
menting a real-time numerical algorithm, namely Generalised α (G-α)

algorithm. Prior to performing the experimental tests, the stability and accuracy analyses of the G-α algorithm were carried out, also considering possible differences between the estimated and the effective stiffness of the physical subdomain. The study proved that the algorithm is stable and first-order accurate considering the discrepancies in the stiffness matrix estimation.

The laboratory test results highlighted that the dissipative replaceable components successfully protected the irreplaceable parts of the frames, which remained elastic at the design limit state, i.e. SD limit state. The devices dissipated a large amount of energy through wide and stable hysteretic behaviours at both SD and NC limit states. Finally, the damaged components were replaced without any difficulty. Furthermore, the comparison with the predictions of the reference numerical models shows favourable outcomes. Moreover, the novel algorithmic correction implemented in the G-α algorithm in hybrid simulation was validated. Via an extensive investigation, stability and accuracy were studied for the G-α algorithm along with the proposed correction, considering the inherent realistic laboratory sources of error, e.g. delay and noise in the signal. The analyses confirmed that the algorithm is stable and first-order accurate.

Finally, following the results of the tests, high-fidelity models of the structures were developed and calibrated on the results of the experimental campaign. This provided a deeper insight into the seismic behaviour of the structures and allowed for the derivation of reliable experimentally calibrated fragility curves by means of incremental dynamic analyses (IDAs). In particular, frames equipped with the seismic dissipative components developed in DISSIPABLE were compared with a state-of-the-art reference model. It turned out that the frames equipped with the seismic dissipative components, at the same probability of failure, can be repaired more quickly, and they are more cost-effective.

Contents

Contents

List of abbreviations

- RFCS - Research Fund for Coal and Steel.
- DRBeS - Dissipative Replaceable Beam Splices.
- DRBrC - Dissipative Replaceable Brace Connection.
- DRLF - Dissipative Replaceable Link Frame.
- DL - Damage Limitation.
- SD - Significant Damage.
- NC - Near Collapse.
- HS - Hybrid Simulation.
- G-α algorithm - Generalized α algorithm.
- IDA - Incremental Dynamic Analysis.
- MRF - Moment Resisting Frame.
- MSTL - Materials and Structures Testing Laboratory.
- MG-α - Monolothic G-α.
- PG-α - Partitioned G-α.
- FETI - Finite Element Tearing and Interconnecting.
- NS - Numerical Subdomain.
- PS - Physical Subdomain.
- SDoF - Single Degree of Freedom.
- GTE - Global Truncation Error.
- LTE - Local Truncation Error.
- 2DoF - Two Degrees of Freedom.
- RBS - Reduced Beam Section.
- HSS - High Strength Steel.

- DRC - Dissipative Replaceable Component.

- SF - Substructured Frame.

- CBF - Concentrically Braced Frame.

- NRMSE - Normalised Root Mean Square Error.

- NEnErr - Normalised Energy Error.

- PIDR - Peak Interstorey Drift Ratio.

- FE - Finite Element.

- S-Model - Simulink Model.

- IM - Intensity Measure.

- EDP - Engineering Demand Parameter.

- CDF - Cumulative Distribution Function.

- Sa_{T1} - First Period Spectral Acceleration.

Chapter 1

Introduction

1.1 State-of-the-Art

Unpredictable natural disasters like earthquakes can potentially cause devastating environmental and community consequences. These events can result in the complete collapse of buildings and even larger structures like bridges or industrial facilities, leading to substantial economic loss and casualties.

To face this problem and build structures that can withstand the seismic load, the conventional design of buildings relies on energy dissipation mechanisms within the structural elements. Most current codes and guidelines [1–3], widely adopted in national and international contexts for seismic actions, propose a capacity design approach to facilitate a ductile collapse mechanism. This approach ensures the formation of plastic hinges at specific points of the structure. In the case of moment resisting frames (MRF), special attention is given to designing structural details that allow for the creation of plastic hinges at the ends of beams, safeguarding columns and preventing soft storey mechanisms. Various strategies have been proposed to promote plasticisation at the beam ends of MRF, such as weakening the beams at their ends [4, 5]. Research studies have recently investigated the replacement of traditional full-strength connections between beams and columns [6, 7] and column bases [8, 9] with partial-strength joints where energy dissipation concentrates [10–14]. Additionally, the use of dampers in partial-strength joints has been examined [15, 16].

While these strategies enable the design of structures capable of dissipating energy during seismic loading, they do not guarantee easy repair after an earthquake. Consequently, economic losses are associated with the prolonged downtime of the structure. Furthermore, buildings de-

1

signed using these approaches may experience significant damage that is often impractical or too expensive to repair. Therefore, minimising damage to structural and non-structural elements after a disaster is crucial, considering both costs and functionality.

To overcome this problem, researchers have focused their attention on passive control systems such as tuned mass dampers and base isolation. The former strategy entails installing a device within the target structure to induce anti-resonance. Introducing such a device aims to mitigate or suppress resonance phenomena that may occur in the structure under specific dynamic loading conditions by altering the structure's natural frequencies. In particular, several types of tuned mass damper can be identified [17]. This strategy was originally developed for high-rise buildings which can suffer strong wind loads [18, 19]. More recently, its potential application for structural protection against earthquakes has been investigated [20–22]. Concerning the base isolation, the main goal is to decouple the building structure from the earthquake input motion, aiming to minimize the transfer of destructive forces and vibrations [23]. This technique is considered the most effective for seismic protection of buildings and has been a subject of engineering research for many years [24].

These passive strategies have proven effective in mitigating seismic events' impact on structures and have garnered significant attention in engineering research and practice. Nevertheless, they are very expensive systems and, therefore, suitable for use in strategic facilities where the cost-benefit analysis gives a positive outcome.

In this context, researchers directed efforts on solutions that can dissipate energy, concentrating the plasticisation on specific parts of the structures that can be replaceable after a seismic event and are affordable for everyone. This fact is particularly important in the context of structural resilience. Friction connections were investigated since they allow for the dissipation of large amounts of energy without experiencing high damage [25–28]. In particular, friction beam-to-column connections were studied within the framework of the FREEDAM project [29]. The experimental campaign results demonstrated that these innovative solutions could sustain destructive seismic events without causing any damage to the steel components [30]. Slit dampers have been experimentally tested in two structural systems: eccentrically braced frames [31] and moment resisting frames [32]. The slit dampers exhibited a wide and compact hysteretic behaviour in both cases, as observed in the force-displacement and moment-rotation diagrams. This behaviour demonstrates that the slit dampers effectively dissipate energy and provide the desired damping characteristics. Added Damping and Stiffness

(ADAS and TADAS) dampers [33], have also been investigated. These dampers have shown suitable hysteretic behaviour when subjected to natural ground acceleration records, effectively providing additional damping to the structure while preserving the integrity of the main structure.

For rocking structures, supplemental rotational inertia can be employed to control the seismic response [34]. This system utilizes inerters, which are mechanical devices that generate a resisting force in proportion to the difference in acceleration between their terminals.

Buckling-restrained braces (BRB), usually made of a yielding steel core surrounded by a hollow steel shape filled with mortar, have been extensively studied in the last three decades. The protective fill is unconnected from the core, preventing it from buckling and allowing it to undergo axial yielding both in compression and tension [35–37]. However, Kiggins and Uang [38] highlighted that the braces' limited stiffness after yielding increases the susceptibility of the system to significant permanent displacements. The mitigation of residual story drifts is achievable by employing BRBs within dual systems [39]. For braced frames, removable dissipative devices were studied within the DUAREM project [40]. The devices comprised short links that were fastened to the floor beams in eccentrically braced frames. Findings demonstrated that the framework could endure the intended earthquake standards, containing all damage within the seismic links that could be replaced with ease.

In order to ensure that buildings incur minimal damage and thus enhance their structural resilience, a viable strategy is to equip structures with self-centering capability [41]. Moreover, the partial self-centring behaviour of structures also offers advantages in terms of life-cycle costs [42]. Several strategies could be used to reach partial or complete self-centering capability, e.g., for structures equipped with BRB, the core could be modified by inserting parallel connections of steel plates with different yield stress so as to modify the hysteretic response and achieve a second yielding point, thus ensuring the structure can re-centre [43].

1.2   DISSIPABLE Project

In recent years, the scientific community focused on developing systems that could guarantee the dissipation of seismic action and that could be easily replaced if damaged, reducing the material consumption and costs of restoring serviceability. In this context, a series of projects funded by the Research Fund for Coal and Steel (RFCS) were carried out. In particular, the INERD project [44] and the FUSEIS project [45] conceptualized the design and the investigation of the seismic behaviour of

innovative types of devices, capable of dissipating a significant amount of energy and being replaced after a seismic event. In greater detail, the INERD project dealt with energy dissipation in bracing systems [46] by means of semi-rigid ductile brace-to-columns connections. The dissipative connections consisted of two external eye-bars welded or bolted to the column flanges, one or two internal eye-bars welded to the end of the diagonal member and a pin running through the eye-bars. In contrast with conventional frames, in the INERD project, the energy dissipation was concentrated in the connections rather than in the structural members. However, this solution presented some issues, i.e., transverse bending of the steel eye-bars, and bearing capacity reduction at the pin-plates interface because of slippage due to holes ovalization. In the FU-SEIS project, major attention was given to moment resisting frames by conceiving two different devices, namely FUSEIS 1, constituted by two closely spaced strong columns rigidly connected by multiple beams with reduced sections made of open or closed steel profiles [47, 48], and FU-SEIS 2, which introduce a discontinuity on the composite beams and restore the continuity through steel plates bolted or welded to the web and flange of the beam [49].

More recently, the RFCS pilot project DISSIPABLE [50] was funded to provide experimental evidence on the high degree of energy dissipation and the easy replaceability after a major seismic event of dissipative seismic components, so as to enhance structural resilience. Since there is an absence of demonstration regarding the behaviour of structures equipped with dissipative and repairable devices on an appropriate scale, using suitably large components, the project has tested full-scale steel structures. Therefore, as part of the project, full-scale tests were performed both on individual components [51] and on two-dimensional frames by means of a pseudodynamic method at the University of Trento [52, 53]. In addition, scaled 3D frames were tested on a shaking table at the National Technical University of Athens to investigate the effect of eccentricity in mass distribution.

Three different components were investigated starting from the previously described devices. The Dissipative Replaceable Brace Connection Figure 1.1a consists of a pin with a chamfered rectangular cross-section, linked by external and internal plates. The pin is the only dissipative element designed for plastic deformation, while other parts remain elastic. This component represents an improved version of the INERD device. The Dissipative Replaceable Link Frame system Figure 1.1b, which is intended to be used in the perimeter frames of steel or steel-concrete buildings, consists of two strong columns connected by multiple beams whose ends are intentionally weakened to promote plastic

4

hinge formation. The Dissipative Replaceable Beam Splice, depicted in Figure 1.1c, is designed for use in composite steel-concrete moment-resisting frames. Plastic deformations are concentrated in steel plates, near the beam-to-column joint. This is achieved by disrupting the steel profile and concrete slab and reconnecting them with fuse plates on the steel profile's web and flange, which is designed to dissipate energy.

The primary benefit of DISSIPABLE devices is that they are made up of common steel fabrication elements (pins, plates, short beams) and bolted joints. As a result, they do not require specific manufacturers to be commercially mass-produced and are not subject to patenting. All the component systems are carefully designed assemblies of structural steel that any steel fabricator can produce without being subject to any patents.
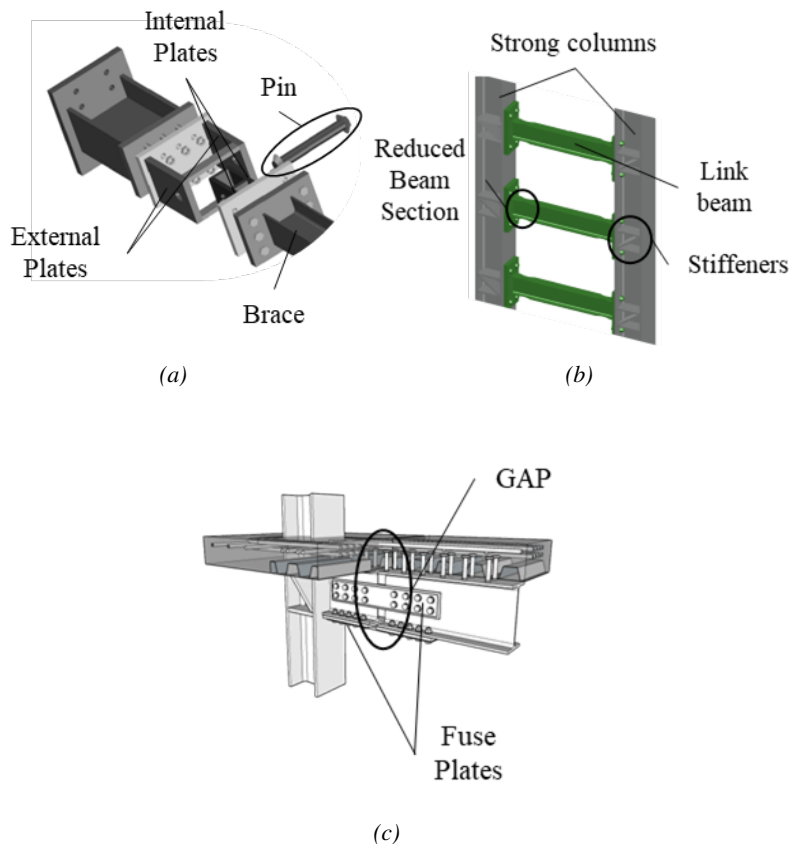

(a) *(b)*

(c)

Figure 1.1: DISSIPABLE components: a) DRBrC, b) DRLF, c) DRBeS

The extensive experimental campaign carried out at the University of Trento consisted of hybrid simulation of five full-scale specimens, (see

Figure 1.2) at different seismic intensity levels, namely Damage Limitation (DL), Significant Damage (SD) and Near Collapse (NC). The main aim was to prove the structure's elastic behaviour during lower levels of earthquakes, and the safeguarding of non-repairable elements (such as beams, columns, and bracings). In order to conduct meaningful tests on whole frames, the substructuring technique was utilised. The method involves physically constructing only a significant part of the structure in the laboratory, while numerically modelling the remaining one. This enabled the verification of low residual displacements and the replaceability of the devices that were substituted following the significant damage limit state test, see 1.1.

(a)
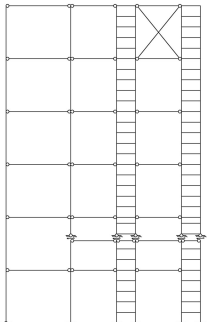

(b)
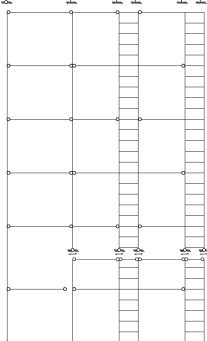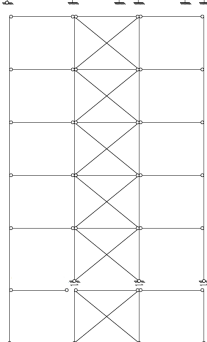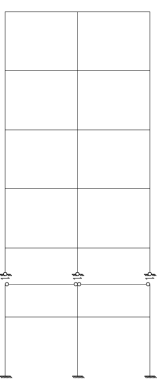
	DL	SD	Substitution Difficulty & Repair Time	NC	Structure Sketch
Test n°1	DRLF - MS	✓	✓	High 6h/man	✓	
Test n°2	DRLF - HSS	✓	✓	High 6h/man	✓	
Test n°3 & n°4	DRBrC - MS DRBrC - HSS	✓	✓	Moderate 4h/man	✓	
Test n°5	DRBeS	✓	✓	Low 2.5h/man	✓	

Table 1.1: Test Matrix

(c)

(d)

Figure 1.2: Physical substructure: a) DRBrC, b) DRLF-mild steel, c) DRLF-HSS, and d) DRBeS frames

1.3 Thesis organization

The thesis highlights the significant and noteworthy research outcomes attained by the author throughout her doctoral program, emphasizing their major contributions and relevance. The manuscript consists of seven chapters, with the central focus on an experimental campaign conducted at the University of Trento, starting from the preliminary analyses and ending with numerical analyses performed on calibrated models. In Figure 1.3, the workflow of the thesis is depicted.

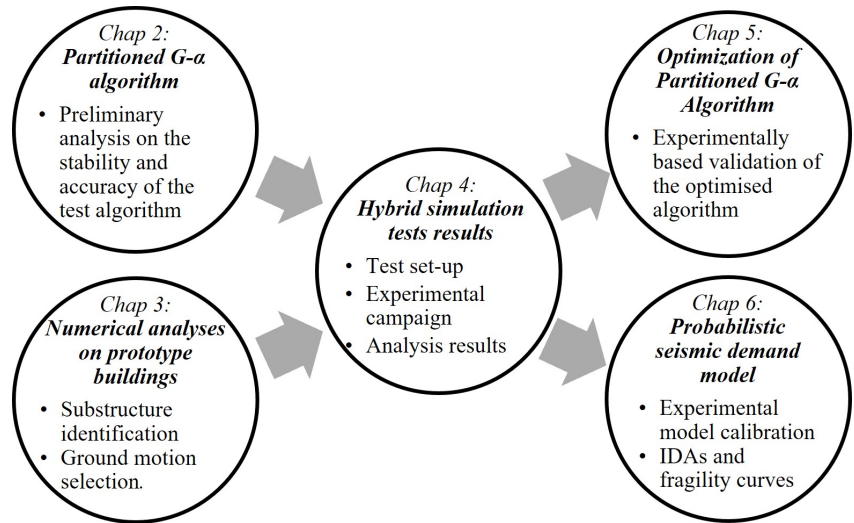Herein, a brief overview of the overall work is provided:

Figure 1.3: Thesis Workflow

Chapter 1 - Introduction

In Chapter 1, the research work is contextualized, and the overall structure of the study is outlined. The chapter introduces the research background and objectives, providing a clear understanding of the motivations behind the study.

Chapter 2 - Partitioned G-α Algorithm

Chapter 2 details the algorithm used for conducting hybrid simulation and comprehensively explains its implementation. The chapter also includes preliminary analyses conducted to assess the suitability of the algorithm. These analyses delve into the stability and accuracy aspects of the algorithm, offering valuable insights into its performance.

Chapter 3 - Numerical analyses on prototype buildings

Chapter 3 focuses on the numerical modelling of the prototype buildings. It provides a detailed depiction of the modelling process, specifically emphasizing the substructuring approach used to define the experimental setup. The chapter elaborates on the step-by-step process for creating the numerical models and thoroughly explains the methodology used to define the experimental configuration.

Chapter 4 - Hybrid simulation tests results

Chapter 4 of the thesis focuses on presenting and discussing the results obtained from the experimental campaign. This chapter provides a comprehensive analysis and interpretation of the data collected during the experimental investigations conducted as part of the research project.

Chapter 5 - Optimization of the Partitioned G-α Algorithm

In Chapter 5, the a posteriori validation of the used algorithm is presented. In particular, stability and accuracy analyses are performed in a model in which every laboratory source of error is accounted for. This Chapter highlights the effectiveness and the validity of the procedure followed for the experimental campaign.

Chapter 6 - Probabilistic seismic demand model

Chapter 6 focuses on the definition of experimentally calibrated fragility curves. In detail, Incremental Dynamic Analyses on experimentally calibrated models were performed to assess the probabilistic behaviour. The Chapter specifically compares the behaviour of the DISSIPABLE frame (equipped with dissipative devices) with a state-of-the-art moment-resisting frame designed based on the capacity design philosophy.

Chapter 7 - Conclusions and future perspectives

Chapter 7 summarised the entire thesis manuscript, recapping the key findings and conclusions. It provides a comprehensive overview of the research conducted and the results obtained. Additionally, this chapter outlines potential future developments and areas of further research related to the overall study.

Chapter 2

Partitioned G-α Algorithm

Hybrid Simulation (HS) was utilised since it allows testing a full-scale frame by only physically building a relevant part while the remaining is numerically simulated. Indeed, HS for experimental tests in civil engineering was proposed in the early '70 [54] and has been successfully applied and validated since then [55–57], in particular in seismic engineering though its use has been extended in recent developments to others fields, e.g., fire engineering [58–60].

This procedure relies on a numerical model of the specimen implemented in the laboratory PC, as shown in Figure 2.1. At each step, the reaction forces of the structure are measured and sent to the PC, which computes the displacements to be imposed on the structure at the next step by solving the equations of motion. Due to laboratory constraints, performing tests in real-time was impossible. Hence, the contributions of mass and damping of the physical and numerical substructure were considered numerically. Indeed, the time-scale factor λ given by Equation 2.1 was employed to expand the time scale to avoid considering the inertia forces on the physical substructure. As shown, λ is given by the ratio between the time integration step used to solve the equation of motion Δt_c and the wall clock time that marks the solution of one-time integration step Δt [61].

$$\lambda = \frac{\Delta t_c}{\Delta t} \qquad (2.1)$$

In the test performed, the value of λ factor varied between 50, for the test at DL limit state, and 100, for NC test. This allowed us to disregard inertial effects, which are typically responsible for instabilities. Indeed, the impact of inertia is proportional to the inverse square of λ: in the most unfavourable scenario of $\lambda = 50$, the specimen's acceleration is only 1/2500 of the actual acceleration. Consequently, the inertial force

is negligible, with a value less than the load cell measurement error (i.e. $3 \cdot 10^2$ N).
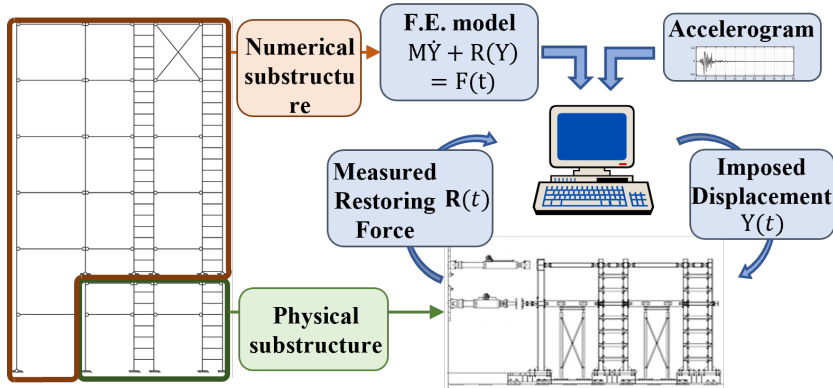

Figure 2.1: Conceptual scheme of hybrid simulation.

In particular, to perform laboratory tests in the Materials and Structures Testing Laboratory (MSTL) of the University of Trento, the partitioned G-α method was employed to solve the equation of motion. This algorithm was adopted since it allows for solving the equation of motion for the numerical and the physical substructure independently, restoring the continuity at the interface by means of Lagrange Multipliers. The actual implementation of numerical algorithms in experimental tests should ensure reliable results regardless of the potential discrepancies with an ideal situation, e.g. source of errors, simplifications, etc. For instance, to maintain a constant time-scaling factor, coupled equations of motion are solved by avoiding iterations or employing a fixed number of iterations. Typically, this is achieved by means of linearly implicit methods [62] that require an estimation of the stiffness matrix, which remained constant during the test. This is a simplification since the stiffness could be affected by the estimation strategy and could not be constant due to non-linearities. This led to considering an initial stiffness different from the actual ones. Therefore, an algorithmic analysis is developed in this chapter taking errors into account in estimating the stiffness used in the computation of operator splitting [63, 64].

This Chapter comprehensively describes the partitioned G-α by which Hybrid Simulations were performed. In particular, the stability and accuracy analyses of both the monolithic and the partitioned algorithms are reported.

2.1   Monolithic G-α method

The specific implementation of the G-α algorithm described by Abbiati
et al. [65] was implemented to perform HS since it allows for considering
the evolution of nonlinearities through time by means of a state vector,
enabling a fast computation of the single time step. The equations of
motion 2.2 are rewritten in a state-space form to integrate them as first-
order equations.

$$\mathbf{M}\dot{\mathbf{Y}} + \mathbf{R}\left(\mathbf{Y}\right) = \mathbf{F}(t) \tag{2.2}$$

where $\mathbf{M}$ is the generalized mass matrix, $\mathbf{Y}$ the generalized displace-
ment vector, $\mathbf{R}$ the generalized restoring force and $\mathbf{F}$ the generalized ex-
ternal load. In particular:

$$\mathbf{Y} = \begin{bmatrix} \mathbf{u} \\ \mathbf{v} \\ \mathbf{s} \end{bmatrix} \quad \mathbf{M} = \begin{bmatrix} \mathbf{I} & \mathbf{0} & \mathbf{0} \\ \mathbf{0} & \mathbf{m} & \mathbf{0} \\ \mathbf{0} & \mathbf{0} & \mathbf{I} \end{bmatrix} \quad \mathbf{R} = \begin{bmatrix} -\mathbf{v} \\ \mathbf{r}(\mathbf{u}, \mathbf{v}, \mathbf{s}) \\ g(\mathbf{u}, \mathbf{v}, \mathbf{s}) \end{bmatrix} \quad \mathbf{F} = \begin{bmatrix} 0 \\ f(t) \\ 0 \end{bmatrix} \tag{2.3}$$

In Equation 2.3, $\mathbf{u}$, $\mathbf{v}$ and $\mathbf{r}$ are the displacement, velocity and restor-
ing force vectors, $\mathbf{s}$ is the additional state vector used to model nonlin-
earities, $\mathbf{I}$ and $\mathbf{m}$ are the identity and mass matrices, respectively, whilst
$g(\mathbf{u}, \mathbf{v}, \mathbf{s})$ is the non-linear function that models the evolution of the ad-
ditional state vector.
In the original work of Jansen et al. [66] introducing the G-α algorithm
for a monolithic domain (MG-α), where monolithic refers to a domain
with no subdivisions, the equation of motion Equation 2.4 is integrated
from t_n to t_{n+1} with a time step $\Delta t = t_{n+1} - t_n$.

$$\mathbf{M}\dot{\mathbf{Y}}_{n+\alpha_m} + \mathbf{R}\left(\mathbf{Y}_{n+\alpha_f}\right) = \mathbf{F}_{n+\alpha_f} \tag{2.4}$$

where:

$$\dot{\mathbf{Y}}_{n+\alpha_m} = (1 - \alpha_m)\,\dot{\mathbf{Y}}_n + \alpha_m\dot{\mathbf{Y}}_{n+1} \tag{2.5a}$$

$$\mathbf{Y}_{n+\alpha_f} = (1 - \alpha_f)\,\mathbf{Y}_n + \alpha_m\mathbf{Y}_{n+1} \tag{2.5b}$$

$$\mathbf{Y}_{n+1} = \mathbf{Y}_n + (1 - \alpha_f)\,\dot{\mathbf{Y}}_n\Delta t + \dot{\mathbf{Y}}_{n+1}\gamma\Delta t \tag{2.5c}$$

The parameters which define the algorithm characteristics, i.e., α_m,
α_f and γ, can be expressed as a function of the infinity spectral radius

ρ_∞ as reported in Equation 2.6.

$$\alpha_m = \frac{3 - \rho_\infty}{2(1 + \rho_\infty)}$$
$$\alpha_f = \frac{1}{1 + \rho_\infty} \tag{2.6}$$
$$\gamma = \frac{1}{2} + \alpha_m - \alpha_f$$

In the former, when $\rho_\infty = 1$, $\alpha_m = \alpha_f = \gamma = 1/2$, the method collapses in the trapezoidal rule, which avoids any algorithmic dissipation whereas, if ρ_∞ is equal to zero, frequencies higher than the sampling frequency are dampened. By exploiting Equation 2.7, which relates the exact and filtered state derivatives (respectively $\dot{Y}_n$, $\dot{Y}_{n+1}$ and V_n, V_{n+1}), it is possible to rewrite the equation of motion as in Equation 2.8.

$$(1 - \alpha_m)V_n + \alpha_m V_{(n+1)} = \dots$$
$$(1 - \alpha_f)\dot{Y}(t_n) + \alpha_f \dot{Y}(t_{n+1}) + o(\Delta t^2) \tag{2.7}$$

$$M\dot{Y}_{n+1} + R(Y_{n+1}) = F_{n+1} \tag{2.8}$$

where:

$$Y_{n+1} = Y_n + V_n(1 - \gamma)\Delta t + V_{n+1}\gamma\Delta t$$
$$V_{n+1} = \dot{Y}_n(1 - \alpha_f)/\alpha_m - V_n(1 - \alpha_m)/\alpha_m \tag{2.9}$$

For an elastic system, in the monolithic case, Equations 2.2, 2.5 and 2.9 can be rewritten in the following form:

$$\mathbf{Z}_{n+1} = \mathbf{A} \cdot \mathbf{Z}_n \tag{2.10}$$

where $\mathbf{A}$ is the amplification matrix of the system. For a single degree of freedom model, a rank four matrix was obtained, see Equation 2.12 considering an undamped system. Defining the spectral radius ρ as the maximum of the eigenvalues λ of the amplification matrix, Equation 2.11, an algorithm is stable when the infinity spectral radius is lower than one. As shown in Figure 2.2a, the stability of the algorithm also depends on the dimensionless frequency Ω given by the product between the algorithmic time-step Δt and the natural frequency of the system ω. By performing the algorithmic analysis, the authors found analogous results to those reported in [65], showing, as depicted in Figure 2.2, that the MG-α method is unconditionally stable and second-order accurate.

$$\rho = max|\lambda_i| \tag{2.11}$$

(a)

(b)
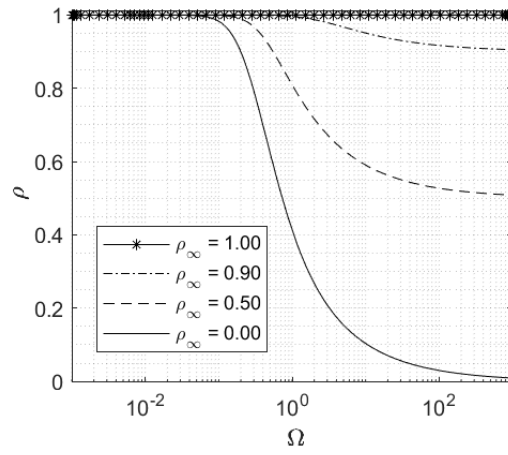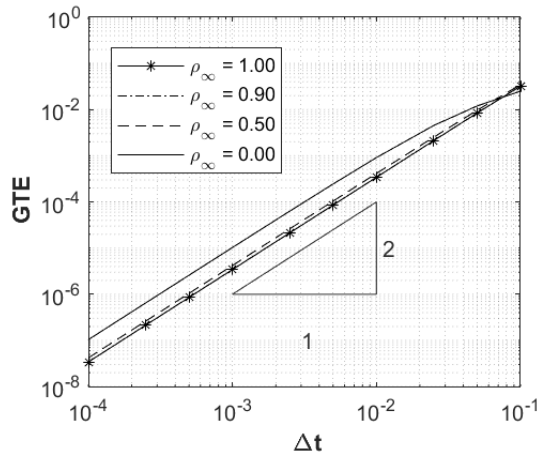
Figure 2.2: MG-α algorithmic analysis: (a) stability and (b) accuracy.

$$A = \frac{1}{\delta} \cdot \begin{bmatrix}
-\beta_1^2\beta_2^2 & -2\beta_1\beta_2\Delta t & -2\frac{2\beta_1\beta_2\rho_\infty\Delta t}{\beta_1\beta_2} & 4\rho_\infty\Delta_t^2 & -\beta_1\beta_2^2\beta_4\Delta t & -2\beta_2\beta_4\Delta t^2 \\[4pt]
\frac{2\beta_1\beta_2\Omega^2}{\Delta t} & \beta_1^2\beta_2^2 & -4\rho_\infty\Omega_2 & -2\beta_1\beta_2\rho_\infty\Delta t & 2\beta_2\beta_4\Omega^2 & -\beta_1\beta_e^2\beta_4\Delta t \\[4pt]
\frac{2\beta_1\beta_2^2\Omega^2}{\Delta t} & \beta_1^2\beta_2^2 & -4\rho_\infty\Omega_2 & -2\beta_1\beta_2\rho_\infty\Delta t & 2\beta_2\beta_4\Omega^2 & -\beta_1\beta_e^2\beta_4\Delta t \\[4pt]
\frac{\beta_1^2\beta_2^2\Omega^2}{\Delta t^2} & \frac{2\beta_1\beta_2\Omega^2}{\Delta t} & \frac{2\beta_1\beta_2\rho_\infty\Omega^2}{\Delta t} & -4\rho_\infty\Omega^2 & \frac{\beta_1\beta_2^2\beta_4\Omega^2}{\Delta t} & 2\beta_2\beta_4\Omega^2 \\[4pt]
-\frac{4\beta_2\Omega^2}{\Delta t} & -2\beta_1\beta_2^2 & \frac{2\beta_1\beta_2^2\rho_\infty}{\beta_1} & 4\beta_2\rho_\infty\Delta t & \beta_1\beta_2^2\beta_3 - 4\rho_\infty\Omega^2 & 2\beta_2^2\beta_4\Delta t \\[4pt]
\frac{2\beta_1\beta_2^2\Omega^2}{\Delta t^2} & \frac{-4\beta_2\Omega^2}{\Delta t} & \frac{4\beta_e\rho_\infty\Omega^2}{\Delta t} & -2\beta_1\beta_2^2\rho_\infty & \frac{2\beta_2^2\beta_4\Omega^2}{\Delta t} & \beta_1\beta_2^2\beta_3 - 4\rho_\infty\Omega^2
\end{bmatrix} \tag{2.12}$$

With $\beta_1 = \rho_\infty - 3$; $\beta_2 = \rho_\infty + 1$; $\beta_3 = 3\rho_\infty - 1$; $\beta_4 = 1 - \rho_\infty$ and $\delta = \beta_1^2\beta_2^2 + 4\Omega^2$.

2.2 Partitioned G-α method

2.2.1 Main Concept

In the partitioned G-α method (PG-α), the spatial domain is partitioned into disconnected subdomains where the compatibility is enforced by means of Lagrange multipliers, as defined by Farhat and Roux on the finite element tearing and interconnecting (FETI) method [67]. The method solves the subdomains separately, deriving the free solutions and imposing the continuity constraint on the interface boundary. The equations of motion are reported in Equation 2.13, where *N* refers to the numerical (NS) and *P* to the physical subdomain (PS). The compatibility between the two subdomains is enforced on the velocity $\dot{\mathbf{Y}}$ by means of Equation 2.14.

$$\begin{cases} \mathbf{M}^N \dot{\mathbf{Y}}_{n+1}^N + \mathbf{R}^N \left(\mathbf{Y}_{n+1}^N \right) = \mathbf{L}^N \mathbf{\Lambda}_{n+1} + \mathbf{F}_{n+1}^N \\ \mathbf{M}^P \dot{\mathbf{Y}}_{n+1}^P + \mathbf{R}^P \left(\mathbf{Y}_{n+1}^P \right) = \mathbf{L}^P \mathbf{\Lambda}_{n+1} + \mathbf{F}_{n+1}^P \end{cases} \tag{2.13}$$

$$\mathbf{G}^N \dot{\mathbf{Y}}_{n+1}^N + \mathbf{G}^P \dot{\mathbf{Y}}_{n+1}^P = 0 \tag{2.14}$$

In the former, $\mathbf{\Lambda}_{n+1}$ are the Lagrange multipliers representing the interfaces forces. $\mathbf{L}$ and $\mathbf{G}$ are Boolean matrices that localise the interfaces' degrees of freedom on the forces and velocity vectors, respectively. The equations of motion can be solved by implementing a predictor-corrector procedure for the two separated subdomains. The state rate vector predictor of the free solution is determined as reported in Equation 2.15, where $\mathbf{D}$ (Equation 2.16) is a matrix operator based on the generalised mass matrix $\mathbf{M}$ and the Jacobian of the restoring force $\nabla_{Y_0}\mathbf{R}$.

$$\dot{\mathbf{Y}}_{n+1}^{free} = \mathbf{D}^{-1} \left(\mathbf{F}_{n+1}^{free} - \mathbf{R} \left(\tilde{\mathbf{Y}}_{n+1}^{free} \right) \right) \tag{2.15}$$

$$\mathbf{D} = \mathbf{M} + \gamma \Delta t \alpha_f / \alpha_m \, \nabla_{Y_0}\mathbf{R} \tag{2.16}$$

If the considered system is linear, the operator can be rewritten as in Equation 2.17.

$$\mathbf{D} = \mathbf{M} + \gamma \Delta t \alpha_f / \alpha_m \, \mathbf{K} \tag{2.17}$$

The Lagrange multipliers are calculated at each time step to compute the link solution, Equation 2.18. In particular, they are determined by means of the so-called Steklov-Poincarè operator, reported in Equation 2.20.

17

$$\dot{\mathbf{Y}}_{n+1}^{link} = \mathbf{M}^{-1}\mathbf{L}\boldsymbol{\Lambda}_{n+1} \tag{2.18}$$

$$\boldsymbol{\Lambda}_{n+1} = -\mathbf{H}^{-1}\left(\mathbf{G}^N\mathbf{Y}_{n+1}^{N,free} + \mathbf{G}^P\mathbf{Y}_{n+1}^{P,free}\right) \tag{2.19}$$

$$\mathbf{H} = \left(\mathbf{G}^N\mathbf{D}^N\mathbf{L}^N + \mathbf{G}^P\mathbf{D}^P\mathbf{L}^P\right) \tag{2.20}$$

In order to minimize the computational burden by avoiding the inversion of the matrix at each time step, the operator $\mathbf{D}$ is calculated once at the beginning of the simulation for both PS and the NS, $\mathbf{D}^P$ and $\mathbf{D}^N$ respectively. While the mass and the stiffness matrices necessary to calculate $\mathbf{D}^N$ are the ones of the numerical model and therefore known, $\mathbf{D}^P$ is computed using a numerically estimated stiffness matrix. To study the stability and accuracy of the algorithm in a more realistic framework, the parameter η was introduced, as suggested by Lamarche et al. [64]. This parameter represents the ratio between the elastic stiffness k^P and the numerically estimated one k_0^P, Equation 2.21.

$$\eta = \frac{k^P}{k_0^P} \tag{2.21}$$

Hence, in the algorithmic implementation, the numerically estimated stiffness is employed to compute the operator splitting $\mathbf{D}^P$, whilst the restoring force $\mathbf{R}$ is physically read from the laboratory PC and therefore accounts for the actual stiffness k^P.

In order to validate the use of the PG-α method in the laboratory framework, stability and accuracy were investigated, implementing the parameter η defined in Equation 2.21 as reported in Equation 2.22.

$$\mathbf{D}^P = \mathbf{M}^P + \gamma\Delta t\alpha_f/\alpha_m\,\eta\mathbf{K}_0^P \tag{2.22}$$

2.2.2 Algorithmic analysis of a single degree of freedom system

The stability and accuracy analyses were initially carried out on a ingle-degree-of-freedom (SDoF) system, as it provides a simple and easy to interpret representation of the problem, which can be easily generalised to multi-degree of freedom problems. However, to confirm the SDoF results, a two-degrees-of-freedom case study was also analysed, the results of which are reported in Section 2.2.3. The case study is depicted in Figure 2.3. Two uniaxial springs, representative of the numerical and the physical stiffness, are connected with a single mass split into a physical and a numerical contribution. In particular, the ratio between the masses

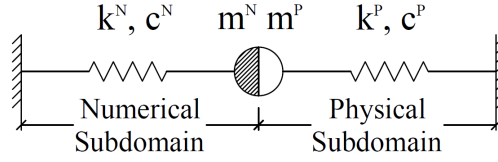has been defined as a variable named b_1, as suggested by Bonelli et al.
[68].

Figure 2.3: SDoF: Case study.

Moreover, the following quantities are defined:

$$m_{tot} = m^N + m^P \tag{2.23a}$$

$$k_{tot} = k^N + k^P \tag{2.23b}$$

$$\frac{m^N}{m^P} = b_1 \tag{2.23c}$$

$$\frac{k^N}{k^P} = \frac{1}{b_1} \tag{2.23d}$$

$$f = {}^1\!/2\pi \sqrt{k_{tot}/m_{tot}} = 1 Hz \tag{2.23e}$$

$$c^N = 0; \quad c^P = 0 \tag{2.23f}$$

As reported in Equation 2.23e, the case study is defined so that the
unitary frequency of the structure is ensured. To investigate the worst
scenario, no damping c is considered for both subdomains since any
damping would be favourable for the stability analysis.

On these premises, a generic time-step of the algorithm has been im-
plemented in the software Mathematica [69] with the aim of computing
the amplification matrix for studying the stability and investigating the
accuracy, both in terms of local and global truncation error. To compute
the truncation errors, the following problem has been taken as a refer-
ence:

$$\omega^2 u + \ddot{u} = 0 \tag{2.24a}$$

$$u_0 = 1, \quad \dot{u}_0 = 0 \quad \text{initial condition} \tag{2.24b}$$

The stability and accuracy, with four different spectral radius values
ρ_∞, i.e. 0.0, 0.5, 0.9 and 1, were studied by choosing the parameters b_1
and η, respectively of 0.1, 1 and 10, and 0.25, 0.50, 0.75, 1.00, 1.25, 1.50
and 1.75. For each combination of these values, stability and accuracy

analyses were performed.

By computing the amplification matrix for the PG-α method applied to an SDoF system, a rank eight matrix was found. The non-null eigenvalues obtained for the investigated parameters are reported with respect to the dimensionless frequency Ω in Figure 2.4. It can be observed that the PG-α algorithm is stable, i.e. $|\lambda| \leq 1$, for any value of b_1 and for $\eta \leq 1$, which means for an actual stiffness k^P lower than the numerically estimated one k_0^P. On the contrary, if η is greater than 1, the algorithm becomes unstable. The only exception lies in the case of an algorithm designed with an infinity spectral radius ρ_∞ lower than 1 and b_1 equal to 10, which represents the case of a numerical mass higher than the physical one. This result implies that a more stable algorithm is obtained when a significantly higher mass on the numerical subdomain and algorithmic damping on the higher modes are considered since lower values of ρ_∞ allow for damping the higher modes.
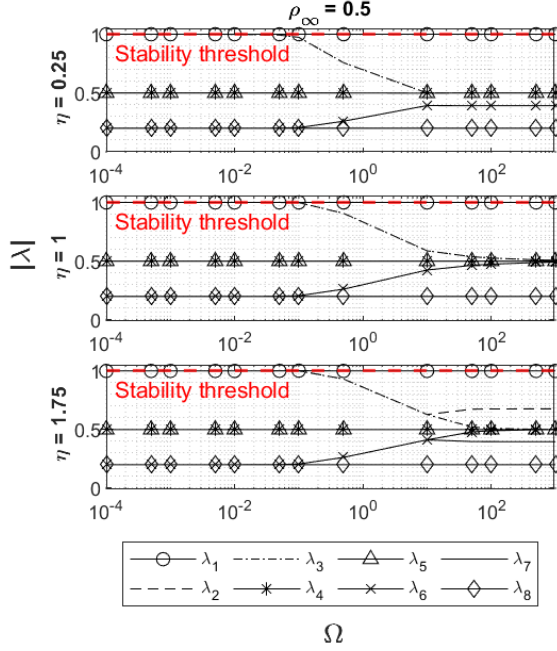

(a)

(b)

(c)

(d)

(e)

(f)
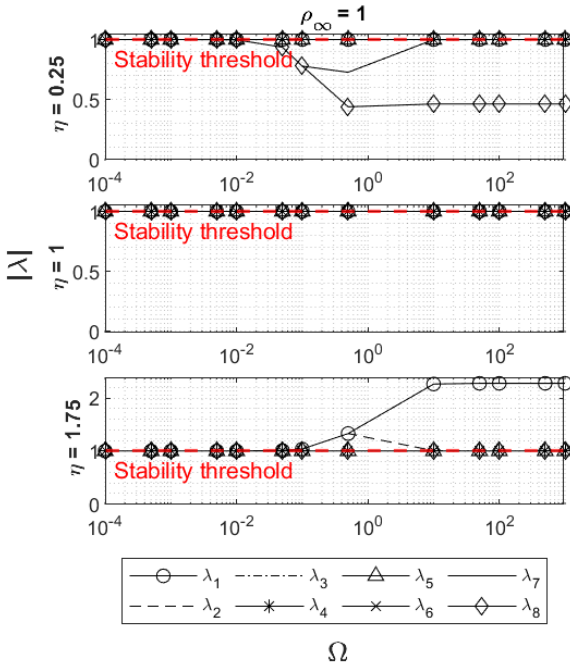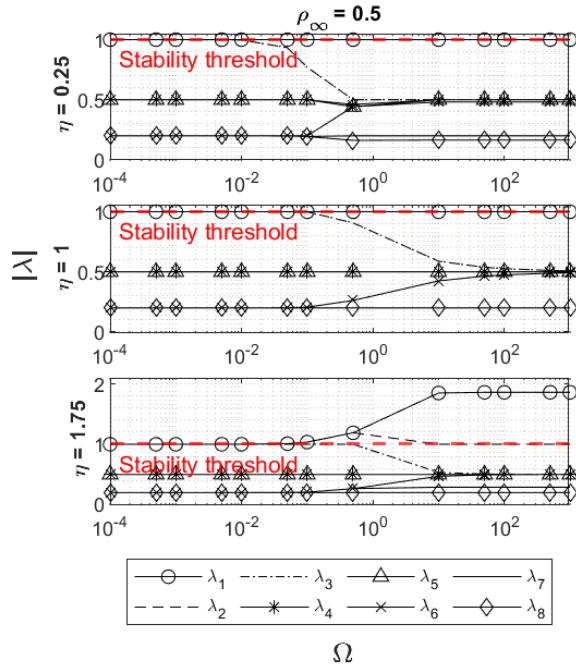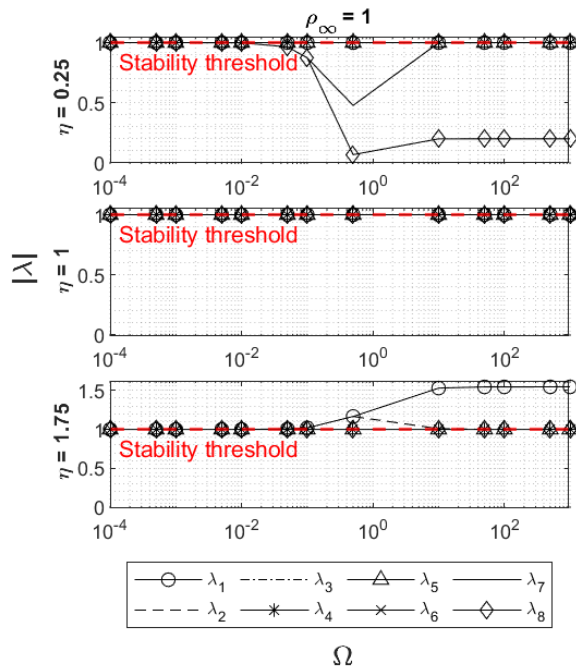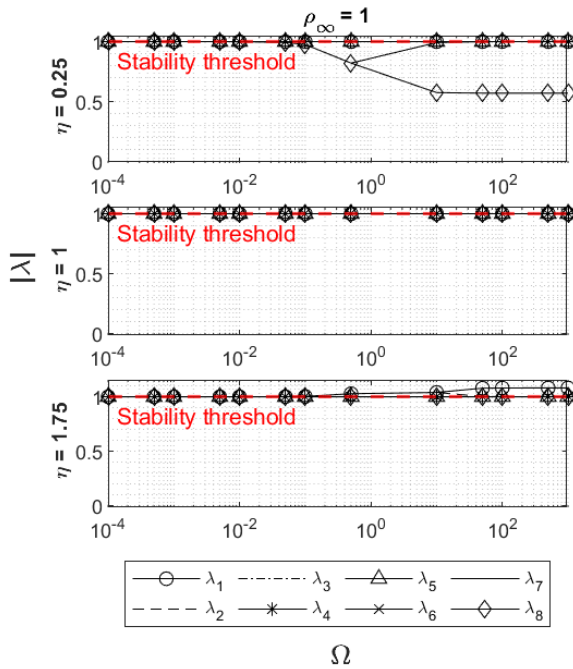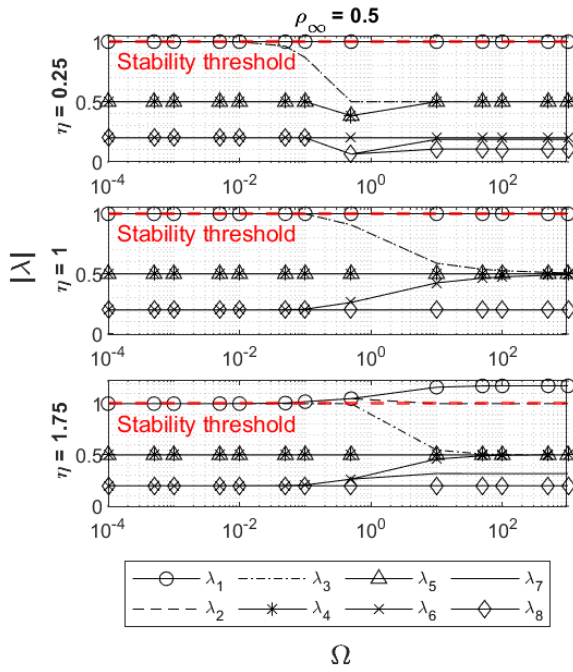
Figure 2.4: SDoF: Stability analysis of the partitioned algorithm: (a-b) $b_1 = 0.1$, (c-d) $b_1 = 1.0$, (e-f) $b_1 = 10$.

Concerning the accuracy analysis, the global truncation error (GTE) is evaluated at a generic time $\bar{t}$ of the analysis as the difference between the algorithmic solution Y and the exact one u, Equation 2.25. In this case, it was chosen to take a time $\bar{t}$ equal to one second.

$$GTE = |Y_{\bar{t}} - u_{\bar{t}}| \qquad (2.25)$$

Instead, the local truncation error (LTE) reported in Equation 2.26 is computed at the first time step for each algorithmic quantity, i.e., displacement, velocity, and acceleration. The order of the algorithm's accuracy is the minimum polynomial degree of the three LTE.

$$LTE = |Y_1 - u_1| \propto \Delta t^p \qquad (2.26)$$

The GTE values reported in Figure 2.5 demonstrate that the algorithm is second-order accurate, as for the monolithic case, only if η is equal to 1, regardless of the value of b_1. As the value of η becomes different from 1, the accuracy decreases to the first order. In Figure 2.5, graphs regarding values of η greater than one are omitted since the algorithm is unstable on such occasions.
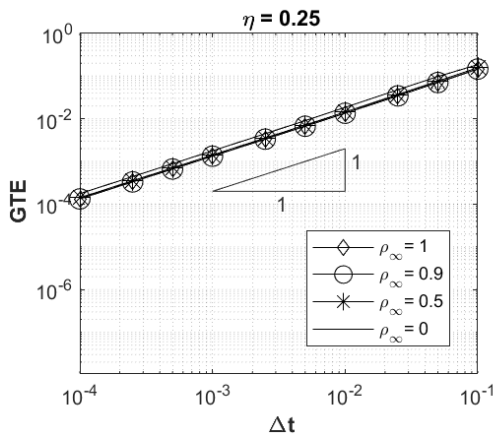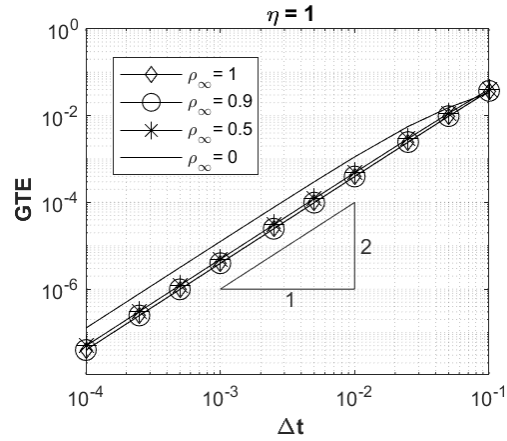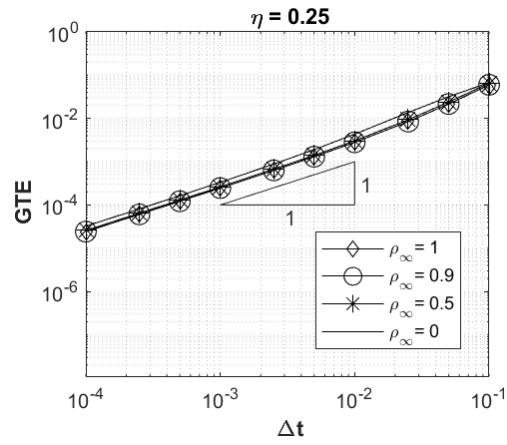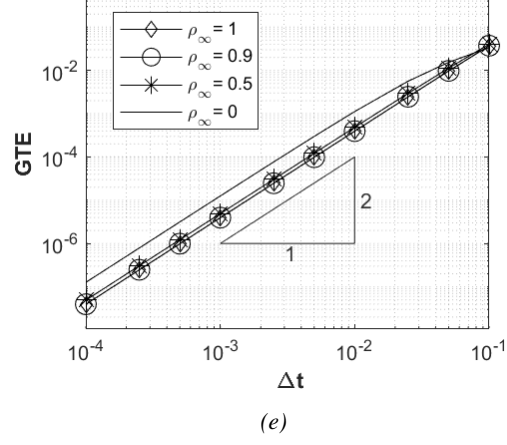
23
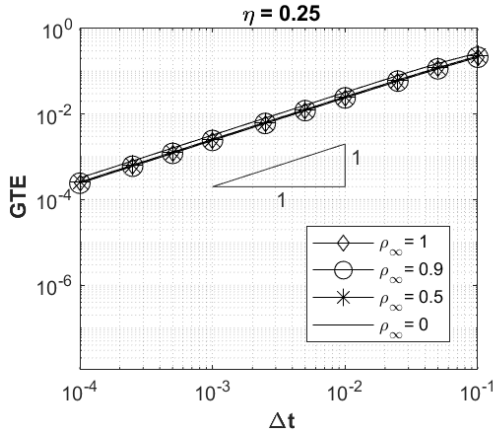
(a)
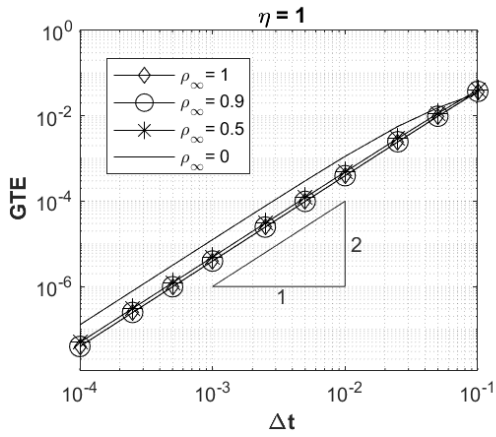
(b)

(c)

(d)

(e)

Figure 2.5: SDoF: Global Truncation Error on the displacement: (a-b) b_1 = 0.1, (c-d) b_1 = 1.0 and (e-f) b_1 = 10.

The local truncation errors in terms of displacement LTE_d, velocity LTE_v and acceleration LTE_a are reported respectively in Equations 2.27 to 2.29. It can be noticed that the order of accuracy strictly depends on the initial conditions. Indeed, using a value of initial acceleration a_0 not in equilibrium with the initial condition on displacement and velocity, the minimum grade of the polynomial is one (see Equations 2.27 to 2.29). However, considering an equilibrated initial acceleration, it can be proven that the order of accuracy becomes equal to two.

$$
\begin{aligned}
LTE_d = {}& \left(-2d_0\pi^2 + \frac{-a_0 + 8d_0\pi^2 - 2a_0\rho_\infty + a_0\rho_\infty^2}{(-3+\rho_\infty)^2(1+\rho_\infty)^2} \right)\Delta t^2 \\
&+ \bigg(-\frac{2\pi^2 v_0}{3} + \frac{16}{(1+b_1)\eta(-3+\rho_\infty)^3(1+\rho_\infty)^3} \cdot \\
&\quad \big(-2\pi^2 v_0 - \pi^2 v_0\eta - 3b_1\pi^2 v_0\eta \\
&\quad -2\pi^2 v_0\eta\rho_\infty - 2b_1\pi^2 v_0\eta\rho_\infty \\
&\quad +\pi^2 v_0\eta\rho_\infty^2 + b_1\pi^2 v_0\eta\rho_\infty^2 \big) \bigg)\Delta t^3 \\
&+ \bigg(\frac{2d_0\pi^4}{3} - \frac{32}{(1+b_1)\,\eta(-3+\rho_\infty)^4(1+\rho_\infty)^4} \cdot \\
&\quad \big(-a_0\pi^2 + 8d_0\pi^4 \\
&\quad -a_0 b_1\pi^2\eta + 8b_1 d_0\pi^4\eta - 2a_0\eta^2\rho_\infty - 2a_0 b_1\pi^2\eta\rho_\infty \\
&\quad +a_0\pi^2\rho_\infty^2 + a_0 b_1\pi^2\eta\rho_\infty^2 \big) \bigg)\Delta t^4 \\
&+ o\left(\Delta t^5\right)
\end{aligned}
$$

$$(2.27)$$

$$
\begin{aligned}
LTE_v = &\left(-4d_0\pi^2 - \frac{-a_0 + 8d_0\pi^2 - 2a_0\rho_\infty + a_0\rho_\infty^2}{(-3 + \rho_\infty)(1 + \rho_\infty)}\right)\Delta t \\
&+ \left(-2\pi^2 v_0 - \frac{1}{(1 + b_1)\eta(-3 + \rho_\infty)^2(1 + \rho_\infty)^2}\cdot\right.\\
&\quad \left(-2\pi^2 v_0 - \pi^2 v_0\eta - 3b_1\pi^2 v_0\eta - 2\pi^2 v_0\eta\rho_\infty\right.\\
&\quad \left.\left. -2b_1\pi^2 v_0\eta\rho_\infty + \pi^2 v_0\eta\rho_\infty^2 + b_1\eta^2 v_0\eta\rho_\infty^2\right)\right)\Delta t^2 \\
&+ \left(\frac{8d_0\pi^4}{3} + \frac{16}{(1 + b_1)\eta(-3 + \rho_\infty)^3(1 + \rho_\infty)^3}\cdot\right.\\
&\quad \left(-a_0\pi^2 + 8d_0\pi^4 - a_0 b_1\pi^2\eta + 8b_1 d_0\pi^4\eta\right.\\
&\quad \left.\left. -2a_0\pi^2\rho_\infty - 2a_0 b_1\pi^2\eta\rho_\infty + a_0\pi^2\rho_\infty^2 + a_0 b_1\pi^2\eta\rho_\infty^2\right)\right)\Delta t^3 \\
&+ \left(\frac{2\pi^4 v_0}{3} + \frac{128}{(1 + b_1)^2\eta^2(-3 + \rho_\infty)^4(1 + \rho_\infty)^4}\cdot\right.\\
\\
&\quad \left(-2\pi^4 v_0 - \pi^4 v_0\eta - 5b_1\pi^4 v_0\eta - b_1\pi^4 v_0\eta^2 - 3b_1^2\pi^4 v_0\eta^2\right.\\
&\quad -2\pi^4 v_0\eta\rho_\infty - 2b_1\pi^4 v_0\eta\rho_\infty - 2b_1\pi^4 v_0\eta^2\rho_\infty \\
&\quad -2b_1^2\pi^4 v_0\eta^2\rho_\infty + \pi^4 v_0\eta\rho_\infty^2 + b_1\pi^4 v_0\eta \\
&\quad \left.\left. \rho_\infty^2 + b_1\pi^4 v_0\eta^2\rho_\infty^2 + b_1^2\pi^4 v_0\eta^2\rho_\infty^2\right)\right)\Delta t^4 \\
&+ o\left(\Delta t^5\right)
\end{aligned}
$$

$$(2.28)$$

27

$$LTE_a = \left(-4\pi^2 v_0 + \frac{4}{(1+b_1)\eta(-3+\rho_\infty)(1+\rho_\infty)} \cdot \right.$$
$$\left(-2\pi^2 v_0 - \pi^2 v_0\eta - 3b_1\pi^2 v_0\eta - 2\pi^2 v_0\eta\rho_\infty \right.$$
$$\left. -2b_1\pi^2 v_0\eta\rho_\infty + \pi^2 v_0\eta\rho_\infty^2 \right.$$
$$\left. \left. +b_1\pi^2 v_0\eta\rho_\infty^2 \right) \right) \Delta t$$
$$+ \left(8d_0\pi^4 - \frac{8}{(1+b_1)\eta(-3+\rho_\infty)^2(1+\rho_\infty)^2} \cdot \right.$$
$$\left(-a_0\pi^2 + 8d_0\pi^4 - a_0 b_1\pi^2\eta + 8b_1 d_0\pi^4\eta - 2a_0\pi^2\rho_\infty \right.$$
$$\left. -2a_0 b_1\pi^2\eta\rho_\infty + a_0\pi^2\rho_\infty^2 \right.$$
$$\left. \left. +a_0 b_1\pi^2\eta\rho_\infty^2 \right) \right) \Delta t^2$$
$$+ \left(\frac{8\pi^4 v_0}{3} - \frac{64}{(1+b_1)^2\eta^2(-3+\rho_\infty)^3(1+\rho_\infty)^3} \cdot \right.$$
$$\left(-2\pi^4 v_0 - \pi^4 v_0\eta - 5b_1\pi^4 v_0\eta - b_1\pi^4 v_0\eta^2 \right.$$
$$\left. -3b_1^2\pi^4 v_0\eta^2 - 2\pi^4 v_0\eta\rho_\infty - 2b_1\pi^4 v_0\eta\rho_\infty - 2b_1\pi^4 v_0\eta^2\rho_\infty \right.$$
$$\left. -2b_1^2\pi^4 v_0\eta^2\rho_\infty + \pi^4 v_0\eta\rho_\infty^2 + b_1\pi^4 v_0\eta\rho_\infty^2 + b_1\pi^4 v_0\eta^2\rho_\infty^2 \right.$$
$$\left. \left. +b_1^2\pi^4 v_0\eta^2\rho_\infty^2 \right) \right) \Delta t^3$$
$$+ \left(-\frac{8d_0\pi^6}{3} + \frac{128}{(1+b_1)^2\eta^2(-3+\rho_\infty)^4(1+\rho_\infty)^4} \cdot \right.$$
$$\left(-a_0\pi^4 + 8d_0\pi^6 - 2a_0 b_1\pi^4\eta + 16b_1 d_0\pi^6\eta - a_0 b_1^2\pi^4\eta^2 \right.$$
$$\left. +8b_1^2 d_0\pi^6\eta^2 - 2a_0\pi^4\rho_\infty - 4a_0 b_1\pi^4\eta\rho_\infty - 2a_0 b_1^2\pi^4\eta^2\rho_\infty \right.$$
$$\left. \left. +a_0\pi^4\rho_\infty^2 + 2a_0 b_1\pi^4\eta\rho_\infty^2 + a_0 b_1^2\pi^4\eta^2\rho_\infty^2 \right) \right) \Delta t^4$$
$$+ o\left(\Delta t^5\right)$$

$$(2.29)$$

In the case of η equal to 1, the minimum order of the polynomials is equal to three when $\rho_\infty = 1$, as reported in Equations 2.30 to 2.32, whilst in all the other cases is equal to two.

$$LTE_d = \frac{\pi^2}{3} v_0\Delta t^3 - \frac{4}{3}\pi^4 d_0\Delta t^4 + o(\Delta t^5) \qquad (2.30)$$

$$LTE_v = -\frac{4}{3}\pi^4 d_0\Delta t^3 - \frac{4}{3}\pi^4 v_0\Delta t^4 + o(\Delta t^5) \qquad (2.31)$$

$$LTE_a = -\frac{4}{3}\pi^4 v_0 \Delta t^3 + \frac{16}{3}\pi^6 d_0 \Delta t^4 + o(\Delta t^5) \qquad (2.32)$$

2.2.3 Algorithmic analysis of two degrees of freedom system

The second case study analysed is the two degrees of freedom (2DoFs) system reported in Figure 2.6. In this case, the ratio between the masses has been defined as a variable named r, as suggested by Bonelli et al. [68] and reported in Equation 2.33b.
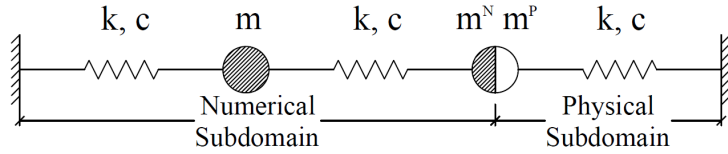


Figure 2.6: 2DoFs: Case study.

$$m = m^N + m^P \qquad (2.33a)$$

$$m^N/m^P = r \qquad (2.33b)$$

$$f_1 = {}^1\!/\!{}_{2\pi}\sqrt{k/m} = 1Hz; \quad f_2 = \sqrt{3}Hz; \quad f_3 = \sqrt{3}Hz \qquad (2.33c)$$

$$c^N = 0; \quad c^P = 0 \qquad (2.33d)$$

The same procedure followed for the single degree of freedom was carried out. Thus, a generic time-step of the algorithm has been implemented in the software Mathematica for computing the amplification matrix **A**. The stability and accuracy were investigated. The algorithm exhibited the same behaviour found for the single degree of freedom, as shown in Figures 2.7 and 2.8. Indeed, the stability analysis highlighted that the algorithm is unstable for values of η greater than one, and the algorithm is second-order accurate if η is equal to 1.
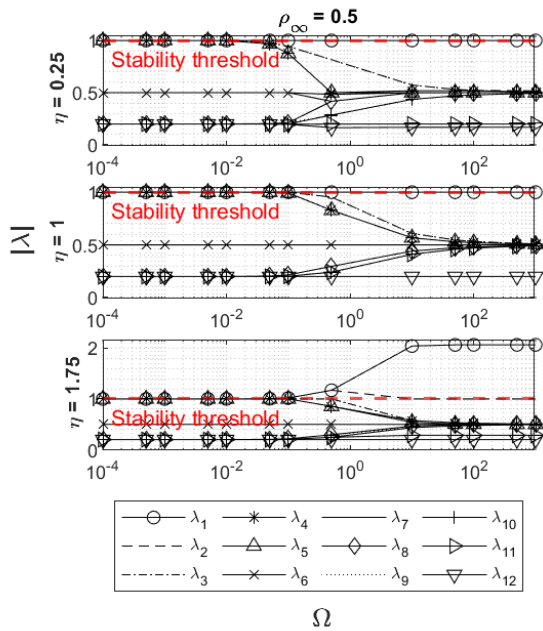
(a)

(b)
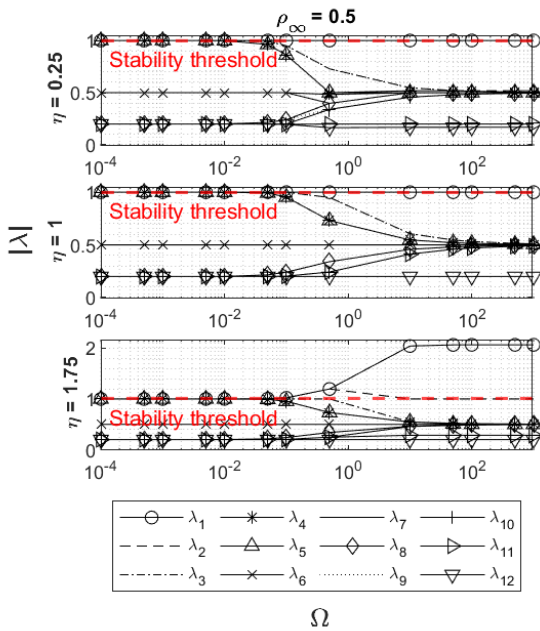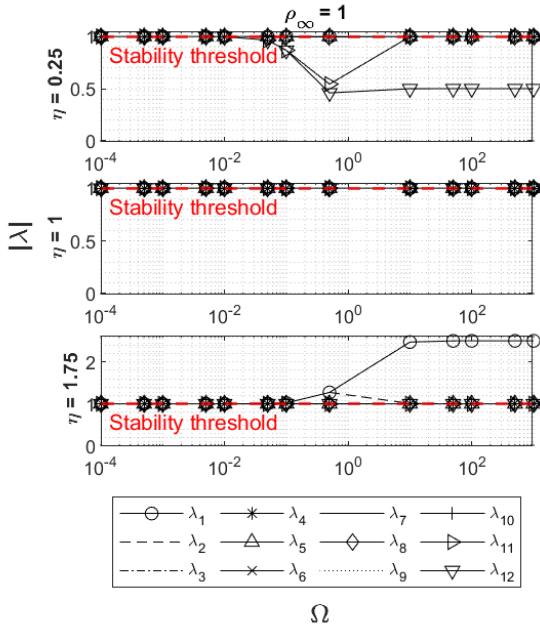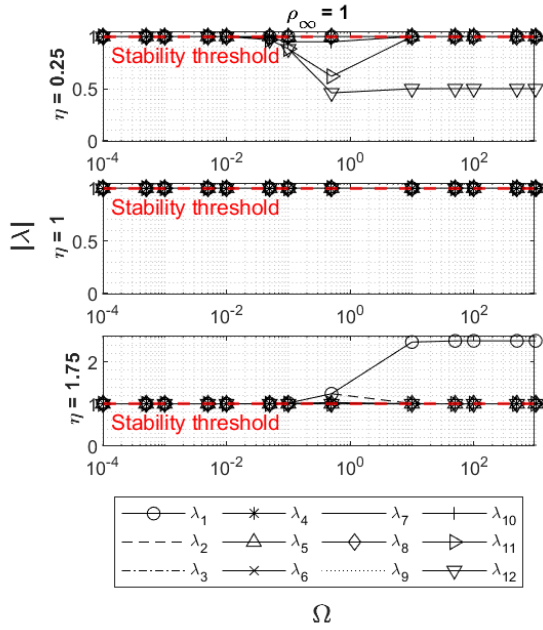
(c)

(d)

(e)
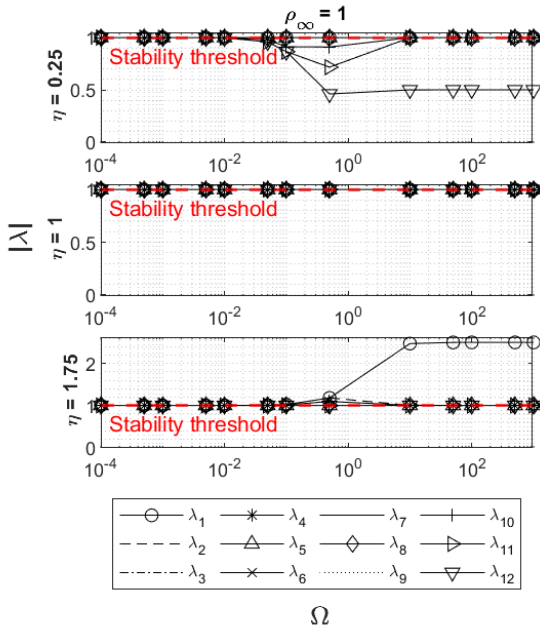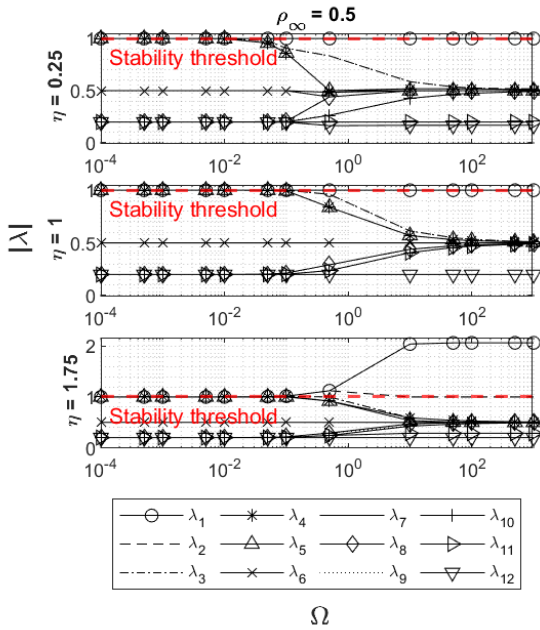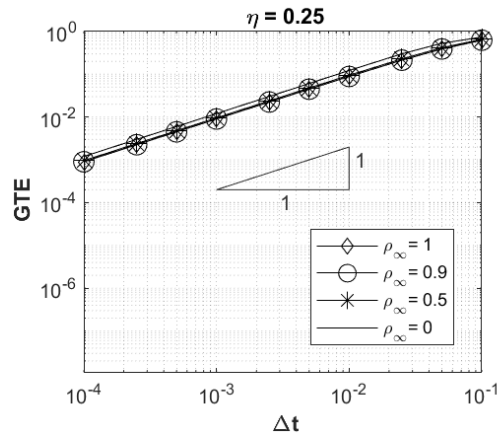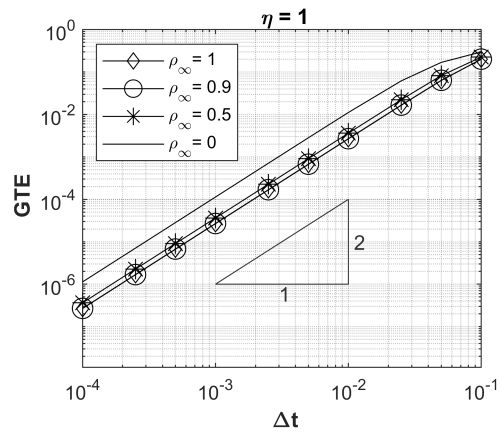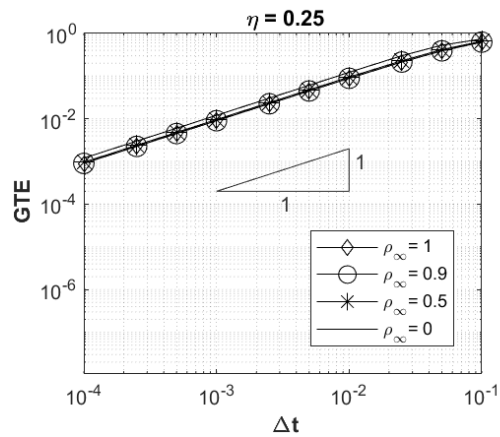

(f)

Figure 2.7: 2DoF: Stability analysis of the partitioned algorithm: (a-b) r = 0.1, (c-d) r = 1.0, (e-f) r = 10.
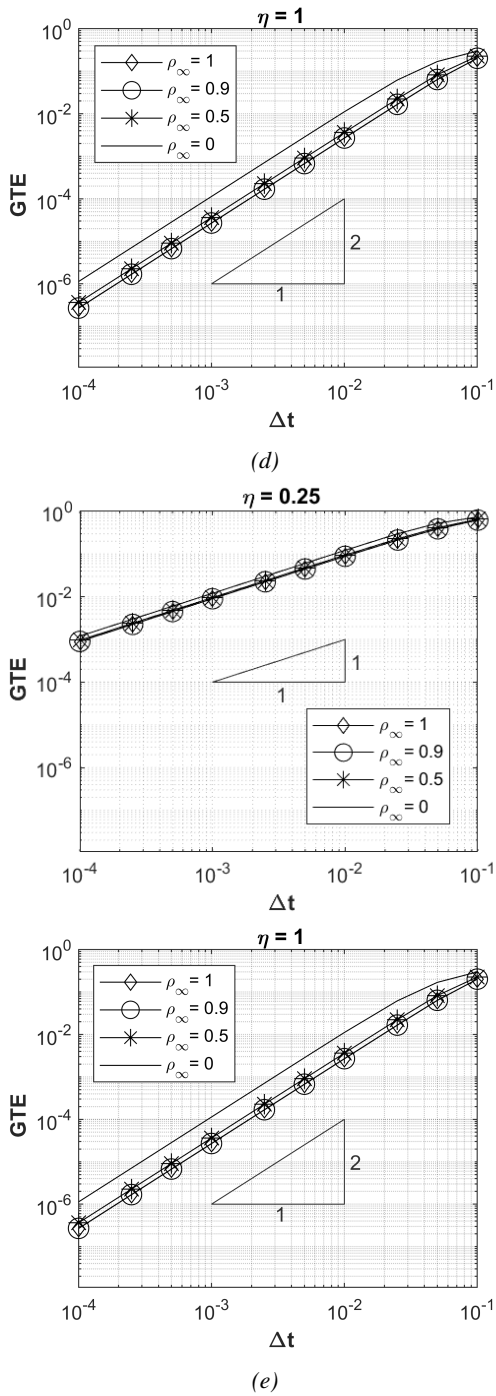
(a)

(b)

(c)

(d)

(e)

Figure 2.8: *2DoF: Global Truncation Error on the displacement: (a-b) r = 0.1, (c-d) r = 1.0 and (e-f) r = 10.*

2.3   Conclusions

This Chapter thoroughly describes an extensive investigation performed
by means of stability and accuracy analyses studied for the generic PG-α
algorithm.

The study proved that the algorithm is second-order accurate, but by
considering possible differences between the initially estimated and the
actual stiffness of the physical subdomain, represented by a factor η, the
order of accuracy decreases to one. Nonetheless, an order of accuracy
of one is sufficient for an algorithm that allows for solving first-order
equations, such as the PG-α algorithm, which rewrites the equation of
motion in a state space form. Regarding the algorithmic stability, it was
proven that the PG-α algorithm is stable until η is lower than one, which
implies that the numerically estimated stiffness is greater than the actual
one. This result is in line with the typical situation in hybrid simulations,
in which the stiffness of the physical subdomain is computed using a
finite element software and therefore is higher than the actual physical
stiffness, owing, for instance, to the presence of gaps and the post-elastic
deformability.

Chapter 3

Numerical analyses on prototype buildings

In this Chapter, the numerical modelling of the components and the preliminary analyses of the prototype buildings under investigation, are described. More emphasis has been given to the description of the DRLF system and the frames equipped with these devices, in line with the main focus of this thesis. Nevertheless, for the sake of completeness, the DR-BrC and DRBeS components have been briefly described since tests on frames equipped with these components were also carried out by the author within the framework of the PhD. Interested readers can find additional details on modelling and testing of these components in the articles [52] and [53] and in Andreotti's PhD thesis [70].

3.1   Description of the components

3.1.1   Dissipative Replaceable Link Frame system

The Dissipative Replaceable Link Frame system, depicted in Figure 3.1, is conceived to be used in the perimeter frames of steel or steel-concrete buildings. It is composed of two rigid neighbouring columns connected by multiple beams so that the whole system works as a Vierendeel beam. The beam links work mainly in bending or in shear, depending on their length, and the columns are subjected to a strong axial force component [71]. The beam is weakened at the ends to force the formation of the plastic hinges at those locations. For this system, replaceability is guaranteed by means of bolted connections between the devices and the columns. Moreover, the beam links are not part of the gravity load-carrying system.

In the tests performed at the University of Trento, IPE sections were employed as beam links and weakened by reducing the gross section following Eurocode 8-3 provisions [72], see Figure 3.2. To guarantee a uniform dissipative behaviour along the structure's height, three different sections were employed in the prototype model of the building, namely IPE 160, IPE 140 and IPE 100. Smaller sections were located at higher storeys where the bending moment on the RBSs induced by earthquake is lower, to ensure a simultaneous plasticization of the sections. This was achieved by minimizing the difference between the overstrength of sections Ω, as defined in Eurocode 8-1. The geometrical characteristics are reported in Table 3.1.

The design of the elements was based on the INNOSEIS recommendations, among others:

- the capacity design shear force V_{Ed} of the beam links was therefore calculated as that resulting from applying the resistant bending moment of the reduced section, according to Equation 3.1.

$$V_{Ed} = \frac{2M_{pl,RBS,Rd}}{l_{RBS}}$$ (3.1)

- to avoid accounting for the shear influence in the computation of the bending plastic resistance of the reduced beam section (RBS), the design shear force should not exceed 0.5 the plastic shear resistance. Combining this with the previous equation for determining the design shear, the length of the beam link should verify the following criteria, Equation 3.2.

$$l_{RBS} < \frac{2M_{pl,RBS,Rd}}{V_{b,pl,Rd}} = \frac{4W_{pl,RBS}}{A_v/\sqrt{3}}$$ (3.2)

- beam-to-column connections and non-dissipative elements were designed to resist the capacity design action effects.

The behaviour of the beams was not governed by lateral-torsional (LT) buckling, as verified according to Eurocode 3 recommendation. Therefore, LT buckling was not explicitly accounted for in the model.

3.1.2 Dissipative Replaceable Bracing Connection

The Dissipative Replaceable Brace Connection is a dissipative component to be used in a concentrically braced frame to connect the frame to the diagonals, designed to avoid buckling in compression. The device
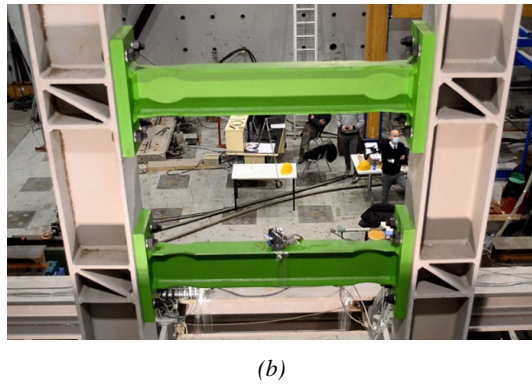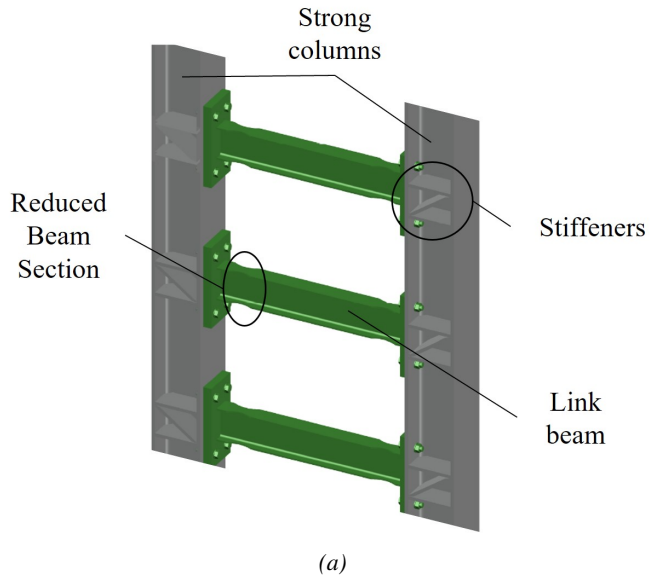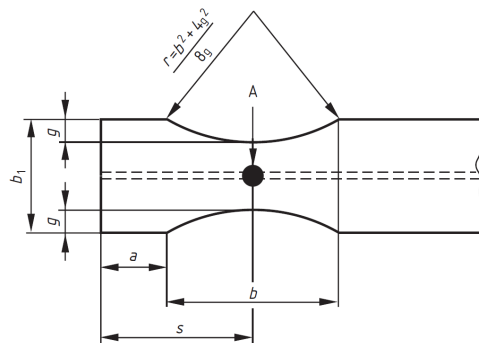
(a)

(b)

Figure 3.1: DRLF: System configuration.

Figure 3.2: Geometry of flange reduction for RBS [72].

	IPE 160	IPE 140	IPE 100
a	49	44	33
b	120	105	75
s	109	96	71
g	16	15	11
r	118	102	69

Table 3.1: DRLF: RBSs geometric characteristics [mm], as depicted in Figure 3.2.

is constituted by a pin with a chamfered rectangular cross-section, connected through two external and two internal plates [46] to a rectangular steel box, as illustrated in Figure 3.3. The pin is the only dissipative component of the system and is designed to achieve plasticisation, while the other elements remain in the elastic range. During the INNOSEIS experimental campaign, a pinching effect was detected. The pinching effect was caused by the clearance between the hole and the eyebar plates, as well as the ovalization of the hole and the out-of-plane flexural behaviour of the supporting eyebar plates. Therefore, in the DISSIPABLE project, an improved solution for the devices was conceived and tested, see Figure 3.3. Enhancements were aimed at both facilitating the replacement and decreasing the pinching effect. Hence an easy-to-demount steel box supporting the pin was conceived. Moreover, as a possible strategy to reduce the ovalization of the holes, the use of high-strength steel (HSS) for realizing the supporting boxes of the DRBrC components was considered.
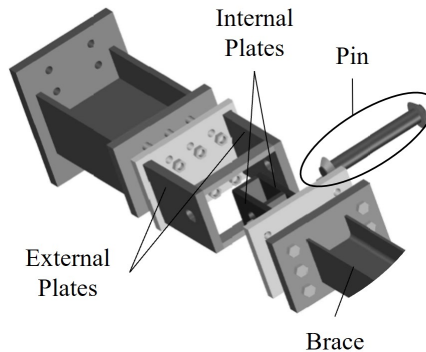

Figure 3.3: DRBrC: Component configuration.

Concerning the mechanical behaviour, the axial force of the bracing

is transferred to the pin through the plates composing the boxes. The
pin behaviour is, therefore, analogous to a four points bending beam.
Referring to Figure 3.4, three different loading conditions can be iden-
tified for the pin: (a) when the external load is applied at first, the pin
is simply supported since the external plates act as pinned connections
and bending actions are concentrated in the middle of the dissipative el-
ement. In the second stage (b), the bending moment increases until the
plastic moment resistance of the pin is achieved, with hinges develop-
ing in correspondence with the internal plates. In the last loading step
(c) plasticity propagates and plastic hinges appear at the ends of the pin.
This mechanical behaviour was simulated with the three linear mono-
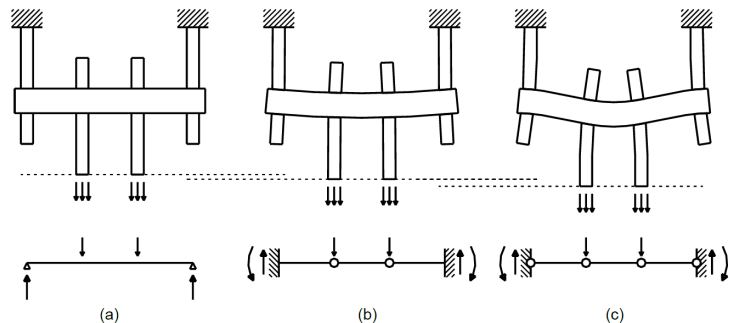tonic curves described in the following Section 3.2.

*Figure 3.4: DRBrC: Stages of loading of the pin and corresponding static model
[71].*

3.1.3 Dissipative Replaceable Beam Splice

The DRBeS component, shown in Figure 3.5, is intended to be used in
composite steel-concrete moment-resisting frames. The design process
is conceived aiming to concentrate plastic deformations in steel plates,
localising the plastic hinges close to the beam-to-column joint. This is
achieved by interrupting the steel profile and the concrete slab and restor-
ing the continuity with fuse plates on the web and the flange of the steel
profile, with the latter designed to dissipate energy [52]. To avoid the
cracking of the concrete slab during a seismic event, two layers of re-
inforcement bars, continuous through the concrete slab gap, are intro-
duced. The reinforcement area is oversized to guarantee the highest de-
formations on the replaceable plates. Therefore, the neutral axis is forced
to lie between the two reinforcement bar layers [49].

Regarding the mechanical behaviour, asymmetry of the moment-
rotation diagram in terms of moments was found due to the strength loss
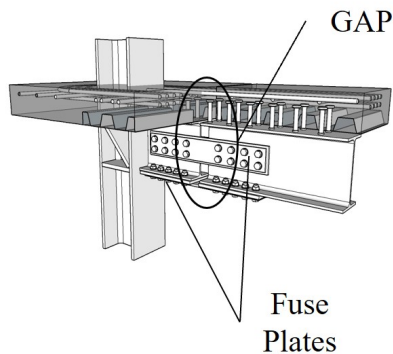
Figure 3.5: DRBeS: Component configuration.

caused by buckling of the fuse plates when subject to hogging bending moment.

3.2 Numerical modelling of the components

The DISSIPABLE component previously described were modelled in the finite element software OpenSees [73]. In this section, the OpenSees tools employed are reported, and the numerical model of each Dissipative Replaceable Component (DRC) is comprehensively described.

3.2.1 OpenSees tools

Elements

In order to model the DRCs in OpenSees, the "twoNodeLink" element was exploited. This element is used to link two nodes through three parallel springs, one for each degree of freedom, see Figure 3.6. The element can have a non-zero length, in which case the transverse and rotational degrees of freedom are coupled. The behaviour of this element is characterised by the three uniaxial constitutive models defined along the three degrees of freedom. For instance, if an elastic behaviour is considered, the stiffnesses for only the three degrees of freedom are needed.

Concerning the non-dissipative elements, "elasticBeamColumn" elements were exploited after verifying the elastic behaviour. The parameters which define the element are listed here:
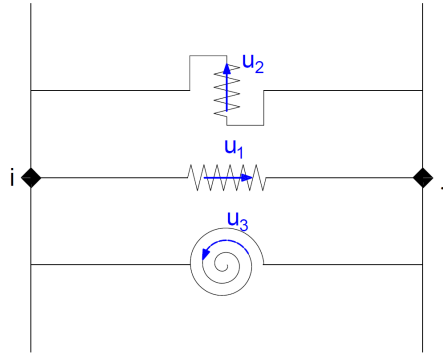
- A, the cross-sectional area of element;

Figure 3.6: Two Node Link element [73].

- E, Young's Modulus;

- I_z, second moment of area about the local z-axis.

Materials

The dynamic non-linear behaviour of the DRCs was modelled in OpenSees
by exploiting two different materials.
Concerning the DRLF system, the Bouc-Wen [74] model was imple-
mented for modelling the evolution of the RBSs non-linear behaviour
through time, as its reliability in hybrid simulation has been extensively
validated [55, 75, 76]. In the model, developed by Wen as an extension
of the Bouc model [77], the restoring force reads:

$$r(t) = \alpha k u(t) + (1 - \alpha) k z(t) \tag{3.3}$$

where α is the ratio between the post-yielding and initial elastic stiff-
ness, k is the initial elastic stiffness and $z(t)$ is the hysteretic displace-
ment whose constitutive law is given as the solution of the following
non-linear differential equation.

$$\dot{z} = \frac{\left[Au - \nu \left(\beta \left| \dot{u} \right| \left| \dot{z} \right|^{n-1} + \gamma \dot{u} \left| z \right|^n \right) \right]}{\eta} \tag{3.4}$$

In the former, A, β, γ and n are parameters that control the shape of
the hysteresis whilst η and ν govern stiffness and strength degradation
phenomena, respectively. In the context of the algorithm implementa-
tion, the hysteretic displacement was selected as the additional state vec-
tor whilst the differential equation Equation 3.4 represents the non-linear

function $g(\dot{u}, z)$ that was implemented in the laboratory PC.

Regarding the DRBeS and DRBrC non-linear behaviour, the Pinching4 uniaxial material was exploited. It represents a "pinched" load-deformation response and exhibits degradation under cyclic loading. Moreover, it allows considering non-symmetric behaviour under cyclic load. The monotonic material curve is defined using sixteen parameters that identify four points for both positive and negative branches. The shape of the hysteretic loop is specified with six non-dimensional parameters. The other parameters to be defined are the ones regarding the degradation of both stiffness and strength, either in the unloading and reloading branches, see Figure 3.7.
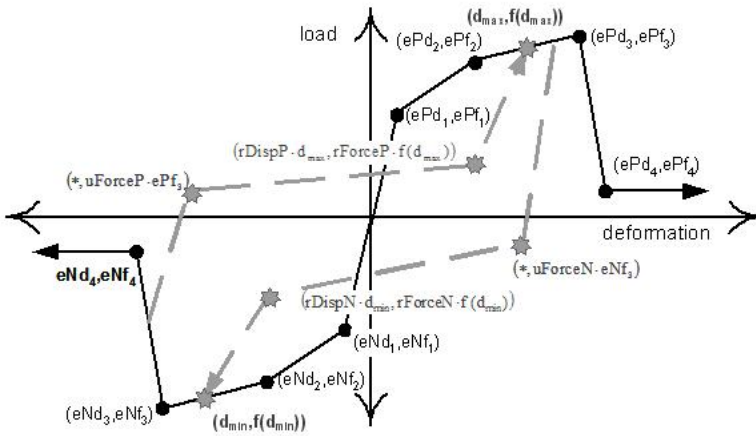

Figure 3.7: Pinching4 material [73].

3.2.2 Component modelling

DRLF system

The DRLF component was numerically modelled in the FE software OpenSees. A single beam link was modelled by subdividing the beam into five parts with different characteristics, as shown in Figure 3.8. The RBSs were modelled with the twoNodeLink element, whilst the remaining parts were elastic beam elements with the mechanical properties of the gross section. At both ends of the beam, a rigid link was inserted for a length equal to half the column section height to avoid considering additional flexibility. Indeed, the rigid link reproduced the moment-resisting connection between the beams and the column, whose stiffness

was classified as rigid, according to Eurocode 3 part 1-8 [78]. Moreover,
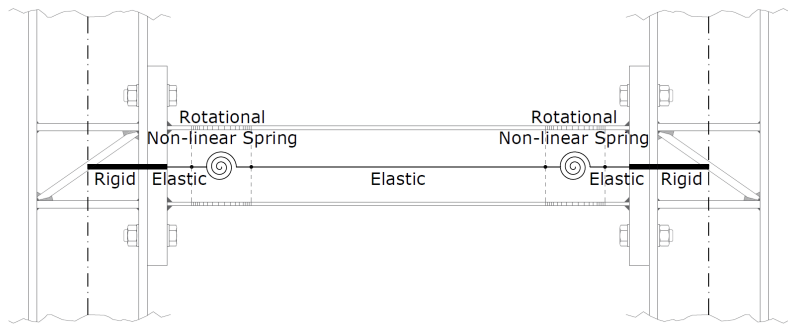this allowed modelling DRLF beam links with the actual physical length
[71].

Figure 3.8: DRLF: Beam link numerical model.

The Bouc–Wen model was chosen for the rotational degree of free-
dom of the twoNodeLink element as it was affected by non-linearity.
The parameters were determined by means of the tool Multical [79] by
minimizing the difference between the numerical and calibrated cycles
both in terms of energy dissipation and monotonic envelope. Two differ-
ent modelling strategies for the DRLF system were implemented for two
different structures, namely DRLF-MS building and DRLF-HSS build-
ing which will be explained in detail in the following paragraphs, Sec-
tions 3.3.1 and 3.3.2. Concerning the DRLF - MS building, the numer-
ical curves were obtained from the model of the RBSs developed in the
finite element software ABAQUS [80]. In this respect, the numerical
model of the RBSs implemented for the tests is shown in Figure 3.9.
The parameters adopted for the three sections are reported in Table 3.2.
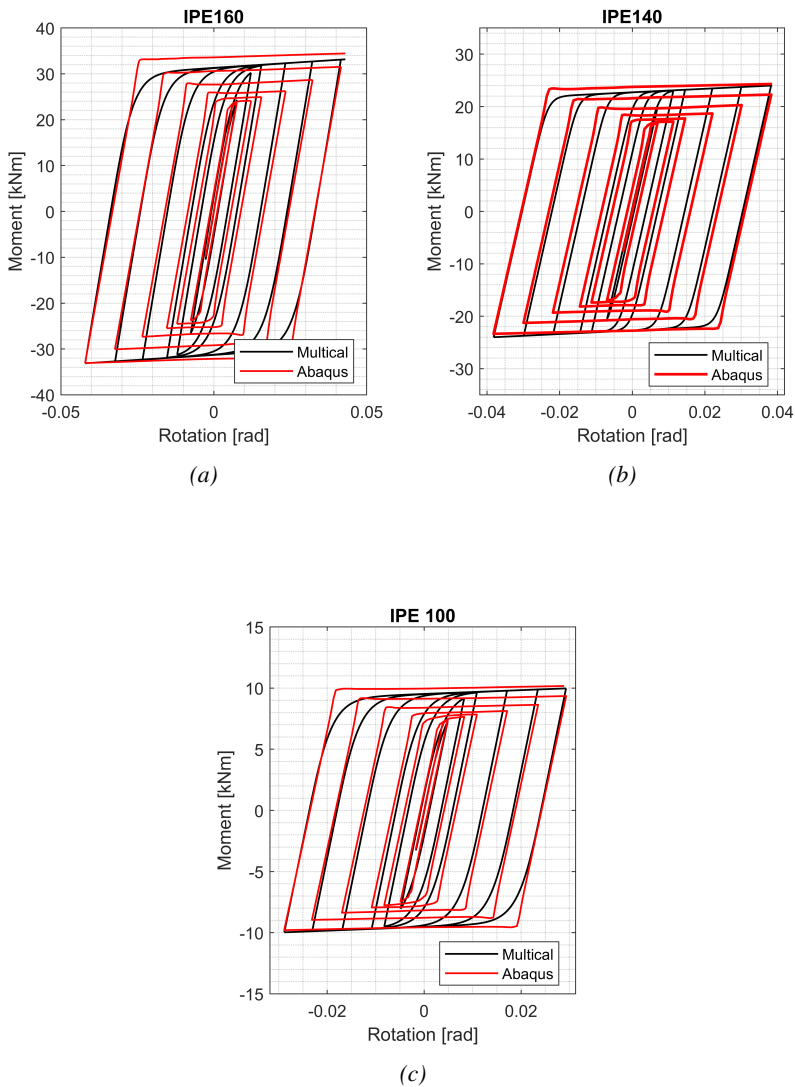
(a)

(b)

(c)

Figure 3.9: DRLF: RBSs numerical modelling.

Conversely, for the DRLF - HSS building, the model parameters for the IPE160 were calibrated on the results of tests conducted on the DRLF - MS building and reported in Section 4.2.3. To reduce the computational burden, equivalent shear springs were implemented, as depicted in Figure 3.10. The non-linear parameters were calibrated on the results of a numerical cyclic test performed on the single beams, to reproduce the behaviour of the whole link beam, Table 3.3.

Parameter	IPE160	IPE140	IPE100
$\alpha(-)$	0.023	0.013	0.008
$k_0(Nm/rad)$	$3.74 \cdot 10^6$	$3.26 \cdot 10^6$	$1.79 \cdot 10^6$
$n(-)$	4.58	2.33	3.99
$\gamma(-)$	$1.01 \cdot 10^9$	$7.44 \cdot 10^4$	$8.51 \cdot 10^8$
$\beta(-)$	$4.91 \cdot 10^9$	$7.50 \cdot 10^4$	$1.21 \cdot 10^9$
$A_0(-)$	1	1	1
$\delta A(-)$	0	0	0
$\delta\nu(-)$	0	0	0
$\delta\eta(-)$	0	0	0

Table 3.2: DRLF-MS: Bouc-Wen parameters of rotational springs.
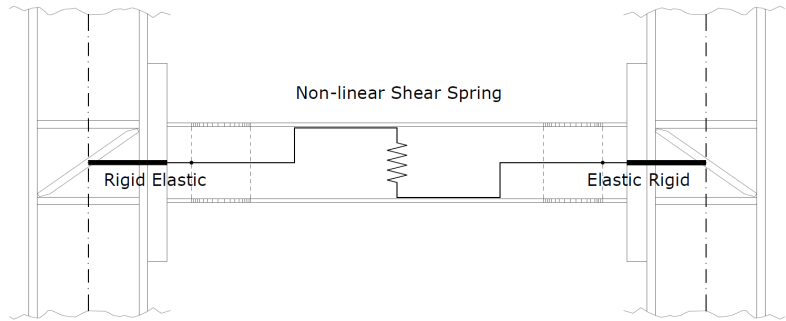
Figure 3.10: DRLF-HSS: Condensed beam link numerical model.

Parameter	IPE160	IPE140	IPE100
$\alpha(-)$	0.044	0.025	0.050
$k_0(Nm/rad)$	$2.08 \cdot 10^7$	$1.34 \cdot 10^7$	$4.28 \cdot 10^6$
$n(-)$	8.20	3.24	2.79
$\gamma(-)$	$1.78 \cdot 10^{20}$	$5.47 \cdot 10^6$	$1.92 \cdot 10^6$
$\beta(-)$	$1.97 \cdot 10^{20}$	$5.47 \cdot 10^6$	$1.92 \cdot 10^6$
$A_0(-)$	1	1	1
$\delta A(-)$	0	0	0
$\delta\nu(-)$	0	0	0
$\delta\eta(-)$	0	0	0

Table 3.3: DRLF-HSS: Bouc-Wen parameters of the shear springs.

DRBrC Component

The non-linear behaviour of the DRBrC was modelled in the software OpenSees with a twoNodeLink element where the axial material adopted was the Pinching4 material. The parameters describing the monotonic backbone curve and the hysteretic loop shape of the DRBrC were calibrated based on cyclic experimental curves obtained by IST Lisbon [81]. In Figure 3.11, one of the curves resulting from the Lisbon experimental campaign is superimposed with the calibrated hysteretic curves. The reported experimental curve was selected since it provides the behaviour of a component with the same pin dimensions as the one employed in the experimental campaign in Trento. This curve was obtained from a constant amplitude cyclic test and was particularly suited for calibrating the non-linear parameters. Subsequently, the parameters found were validated with experimental curves obtained with an ECCS test protocol, which were used to verify the behaviour of the devices for structures located in high seismic areas. The calibration procedure of the OpenSees constitutive models was performed by means of the software Multical. The parameters defining the monotonic behaviour of the component are listed in Table 3.4.
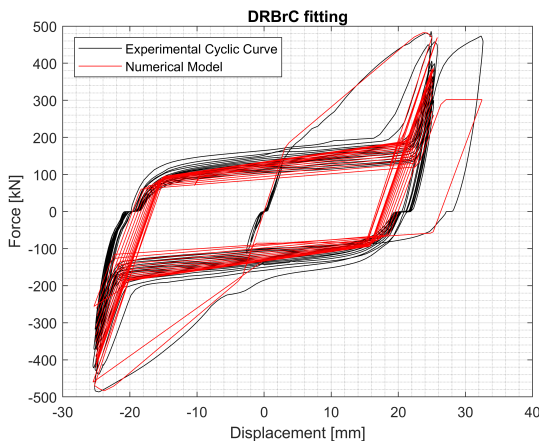

Figure 3.11: DRBrC: Comparison between the experimental results and the calibrated hysteretic behaviour.

Parameter	Pin dimensions 45x35 [mm]	Pin dimensions 45x25 [mm]	Pin dimensions 45x20 [mm]
ePd1 [mm]	2.79	2.45	2.09
ePd2 [mm]	19.83	17.9	15.15
ePd3 [mm]	21.12	18.77	16.02
ePd4 [mm]	22.54	19.79	16.91
ePf1 [N]	$1.23 \cdot 10^5$	$8.89 \cdot 10^4$	$5.62 \cdot 10^4$
ePf2 [N]	$3.36 \cdot 10^5$	$2.34 \cdot 10^5$	$1.53 \cdot 10^5$
ePf3 [N]	$3.47 \cdot 10^5$	$2.40 \cdot 10^5$	$1.58 \cdot 10^5$
ePf4 [N]	$3.38 \cdot 10^5$	$2.34 \cdot 10^5$	$1.53 \cdot 10^5$
eNd1 [mm]	-2.79	-2.45	-2.09
eNd2 [mm]	-19.83	-17.9	-15.15
eNd3 [mm]	-21.12	-18.77	-16.02
eNd4 [mm]	-22.54	-19.79	-16.91
eNf1 [N]	$-1.23 \cdot 10^5$	$-8.89 \cdot 10^4$	$-5.62 \cdot 10^4$
eNf2 [N]	$-3.36 \cdot 10^5$	$-2.34 \cdot 10^5$	$-1.53 \cdot 10^5$
eNf3 [N]	$-3.47 \cdot 10^5$	$-2.40 \cdot 10^5$	$-1.58 \cdot 10^5$
eNf4 [N]	$-3.38 \cdot 10^5$	$-2.34 \cdot 10^5$	$-1.53 \cdot 10^5$

Table 3.4: DRBrC: Pinching4 parameters defining monotonic behaviour.

49

DRBeS Component

The DRBeS behaviour was modelled in the software OpenSees by means of the Pinching4 material, due to the asymmetric behaviour in the moment-rotation relation and the strong pinching effect. Experimental curves obtained by previous experimental campaigns [71, 82] representing the cyclic loading of an actual component were exploited to reproduce the hysteretic behaviour in terms of moment-rotation. As for other devices, also for the DRBeS component the material parameters were calibrated through Multical. The calibrated numerical behaviour is shown in Figure 3.12. Three different geometric configurations of the device were employed in the building equipped with DRBeS component. The plate dimensions are listed in Table 3.5 whilst the Pinching4 parameters are reported in Table 3.6.
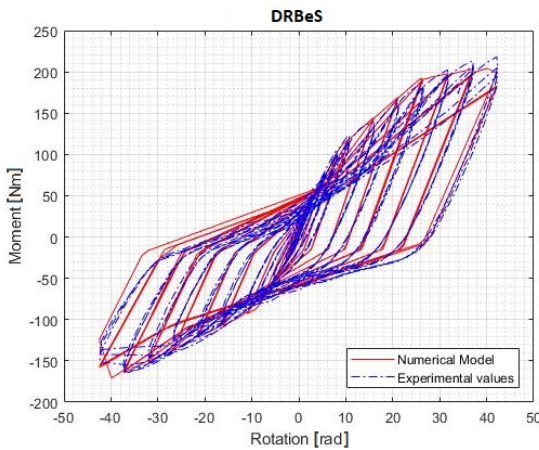
Figure 3.12: *DRBeS: Comparison between the experimental results and the calibrated hysteretic behaviour.*

Type	Flange plate	Web plate [mm]
A	120 x 10	100 x 6
B	100 x 10	100 x 6
C	100 x 8	100 x 6

Table 3.5: *DRBeS: Width and thickness dimensions of flange and web plates [mm].*

Parameter	Type A	Type B	Type C
ePd1 [rad]	$7.58 \cdot 10^{-3}$	$8.89 \cdot 10^{-3}$	$6.27 \cdot 10^{-3}$
ePd2 [rad]	$2.20 \cdot 10^{-2}$	$2.58 \cdot 10^{-2}$	$1.82 \cdot 10^{-2}$
ePd3 [rad]	$3.39 \cdot 10^{-2}$	$3.98 \cdot 10^{-2}$	$2.81 \cdot 10^{-2}$
ePd4 [rad]	$6.47 \cdot 10^{-2}$	$7.58 \cdot 10^{-2}$	$5.35 \cdot 10^{-2}$
ePf1 [Nmm]	$1.35 \cdot 10^{5}$	$1.48 \cdot 10^{5}$	$1.21 \cdot 10^{5}$
ePf2 [Nmm]	$2.40 \cdot 10^{5}$	$2.64 \cdot 10^{5}$	$2.16 \cdot 10^{5}$
ePf3 [Nmm]	$2.62 \cdot 10^{5}$	$2.88 \cdot 10^{5}$	$2.35 \cdot 10^{5}$
ePf4 [Nmm]	$2.14 \cdot 10^{5}$	$2.36 \cdot 10^{5}$	$1.92 \cdot 10^{5}$
eNd1 [rad]	$-5.19 \cdot 10^{-3}$	$-7.02 \cdot 10^{-3}$	$-4.38 \cdot 10^{-3}$
eNd2 [rad]	$-3.33 \cdot 10^{-2}$	$-4.24 \cdot 10^{-2}$	$-1.84 \cdot 10^{-2}$
eNd3 [rad]	$-3.37 \cdot 10^{-2}$	$-4.29 \cdot 10^{-2}$	$-1.86 \cdot 10^{-2}$
eNd4 [rad]	$-6.02 \cdot 10^{-2}$	$-7.66 \cdot 10^{-2}$	$-3.33 \cdot 10^{-2}$
eNf1 [Nmm]	$-9.22 \cdot 10^{4}$	$-1.17 \cdot 10^{5}$	$-8.45 \cdot 10^{4}$
eNf2 [Nmm]	$-1.59 \cdot 10^{5}$	$-2.02 \cdot 10^{5}$	$-1.46 \cdot 10^{5}$
eNf3 [Nmm]	$-1.32 \cdot 10^{5}$	$-1.68 \cdot 10^{5}$	$-1.21 \cdot 10^{5}$
eNf4 [Nmm]	$-1.32 \cdot 10^{5}$	$-1.68 \cdot 10^{5}$	$-1.21 \cdot 10^{5}$

Table 3.6: DRBeS: Pinching4 parameters defining monotonic behaviour.

3.3   Numerical modelling of the building prototypes

In this Section, the building prototypes and the substructuring procedure
to define the tested frame are thoroughly described. In particular, four
different three-dimensional models were developed in the finite element
software SAP2000 [83], each composed of two spans in the transversal
X-direction, three spans in the longitudinal Y-direction and six storeys.
The design was carried out by means of Eurocode 8-1 design spectrum,
with peak ground acceleration equal to 0.36g, which corresponds to the
significant damage limit state and soil type A while the building design
life was taken equal to 50 years. For defining the bi-dimensional frame
to be tested, the first frames in the X-direction of the building were con-
sidered. The reduction of the model from a 3D building to a 2D frame
was carried out under the hypothesis of the same distribution between
base-shear and masses among the different frames. Therefore, by using
three distinct accelerograms, the base shear of the 3D building was cal-
culated and compared to the single frame.
To determine the substructured configuration, the laboratory constraints
were considered. Indeed, a maximum of two actuators could be com-
manded simultaneously and only the horizontal degree of freedom could

be efficiently controlled in the laboratory. On these premises, aiming to obtain results that were consistent with the analyses performed on the 2D frame, preliminary analyses were conducted, simulating the presence of the actuators by means of continuity constraints between the numerical and experimental substructures. After an iterative procedure, the best position where to subdivide the structure has been identified for each structure.

Global imperfections were not included in the model as it was established in the design phase that the structure was not susceptible to second-order effects. Regarding local imperfections, the possible buckling phenomena of structural elements subjected to significant compressive stresses, e.g. columns, under the seismic load combination did not govern the response of the structure. Indeed, preliminary analyses confirmed the negligible impact of local imperfections on the results. For instance, to induce dissipation in the components, the bracings were designed to behave in the elastic range without any buckling involved. Therefore, in view of the complexity of the hybrid simulation tests, it was preferred to keep the numerical models as simple as possible and the local imperfections were consequently not included. Finally, an S355 steel grade was chosen for all the non-dissipative members, whilst DRCs were made of S235.

3.3.1 DRLF - MS building

The prototype building under investigation was composed of two spans in the transversal X-direction, three spans in the longitudinal Y-direction and six storeys. In the Y-direction, the horizontal carrying load capacity relied on two external braced frames, equipped with Dissipative Replaceable Bracing Connection. In the X-direction instead, two parallel DRLF systems were employed and coupled employing bracing elements at the top floor to reduce the building deformability.

As depicted in Figure 3.13, the columns were pinned in the longitudinal direction, where braced frames were employed, whilst fixed column bases were considered in the transversal direction where the lateral load was withstood by DRLF system. Since a rigid diaphragm constraint was adopted, it was possible to consider lumped masses on each floor. The masses were located at the centre of gravity and no eccentricity was considered since 2D tests were planned. The initial modelling of the 3D building was developed in SAP2000, and the structure was designed by means of liner dynamic analysis, according to Eurocode 8-1 [84] and Eurocode 8-3 [72], as suggested by Pinkawa et al. [85].
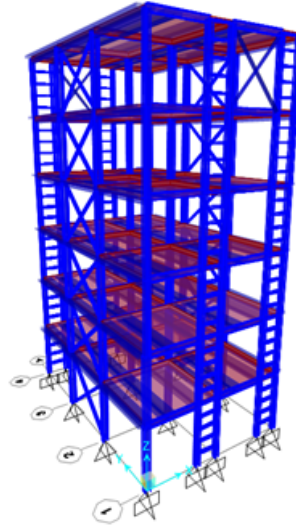
Figure 3.13: DRLF-MS: SAP2000 Model.

The non-linear model was developed in OpenSees, and consistency
with the SAP2000 analyses was checked comparing the modal proper-
ties, see Tables 3.7 and 3.8. For modelling beams and columns, as well as
the bracing system, ElasticBeamElements were employed. The assump-
tion of elastic behaviour under increasing intensity of seismic events was
verified afterwards by means of detailed numerical analyses. Moreover,
as aforementioned the DRLF system was modelled concentrating the
non-linear behaviour on the RBSs of the beam links.

Mode	OpenSees Periods [s]	SAP2000 Periods [s]	Error
1	1.52	1.49	2%
2	1.01	1.00	1%
3	0.87	0.84	1%

Table 3.7: DRLF-MS: 3D SAP2000 and OpenSees Model Periods.

To investigate the inelastic behaviour, push-over and time history
analyses were performed, the latter by means of accelerograms at sig-
nificant damage and near collapse limit states. Figure 3.14 shows the
hysteretic behaviour of RBSs installed in the building subjected to one
SD accelerogram. For brevity, only four moment-rotation diagrams at
each floor level of the first frame are presented. The structure experi-

Mode	Participant mass along X	Participant mass along Y	Participant mass along Z
1	**79%**	0%	0%
2	0%	**71%**	0%
3	0%	0%	**73%**

Table 3.8: DRLF-MS: Partecipant masses.

enced large and uniformly distributed hysteretic behaviour, with the only exception of the 6th floor where the components remained almost elastic due to the additional stiffness provided by the braces. As a consequence, rigid translation of the top floor is predominant during seismic activity. This behaviour results in a low seismic demand on the devices, since the beam links are activated by the columns' inflection, i.e. Vierendeel mechanism.
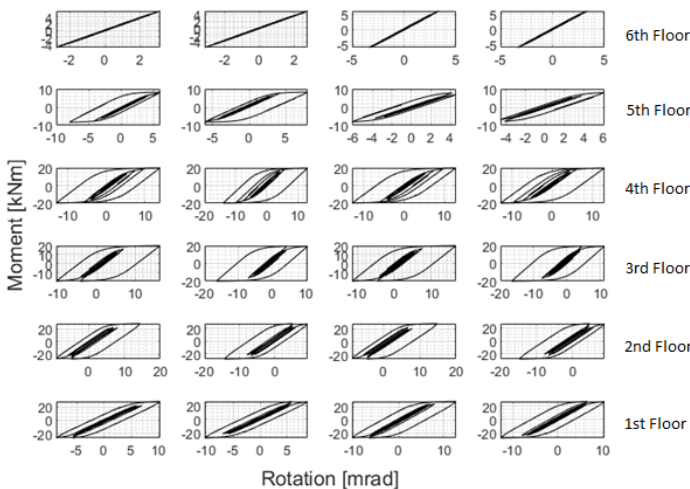
Figure 3.14: DRLF-MS: Hysteretic behaviour of RBSs at SD limit state.

To define the bi-dimensional frame to be tested, the base shear of the single frame was calculated considering three distinct accelerograms. In Table 3.9 the shear undergone by each frame is reported as a percentage of the total shear of the structure. The negative values, present for the internal frames, were given by the continuity of the gravity frame column, which provides the internal frames with a slight resistance to horizontal actions. To consider this effect, a lumped column [86] was introduced in the bi-dimensional model. The modulus of inertia of this column was

calculated, floor by floor, as the sum of the modulus of inertia of all the
columns of the gravity frame closer to the DRLF frame. Half of the total
mass was assigned to the frame and concentrated in one node on each
floor, placed at the top of the central column and connected to the others
by means of rigid links. The model of the studied frame is depicted in
Figure 3.15.

	1° frame	2° frame	3° frame	4° frame
1° accelerogram	50.50%	−1.20%	−1.00%	51.70%
2° accelerogram	52.60%	−2.70%	−2.60%	52.70%
3° accelerogram	53.20%	−4.90%	−5.50%	57.20%
Mean	52.10%	−2.90%	−3.10%	54.00%

*Table 3.9: DRLF-MS: Single frame base shear variation with respect to the 3D
building model.*

The procedure to define the substructured configuration led to di-
viding the structure at the midpoint of the second-floor columns, which
corresponds to the inflection point, as shown in Figure 3.16. Horizon-
tal internal constraints were introduced at the substructuring point to re-
produce the laboratory set-up, implying that the displacement applied
at the top of the physical subdomain columns is the same as the base
of the numerical subdomain, i.e. continuity condition between the two
subdomains. In addition, vertical restraints were imposed at the base
of the numerical subdomain to avoid an ill-conditioned problem, i.e.,
a floating domain. The influence of these simplifications on the struc-
tural behaviour was investigated by comparing the response of the two
structures, namely 2D frame and substructured frame, in terms of modal,
pushover and time-histories analyses, as shown hereafter.
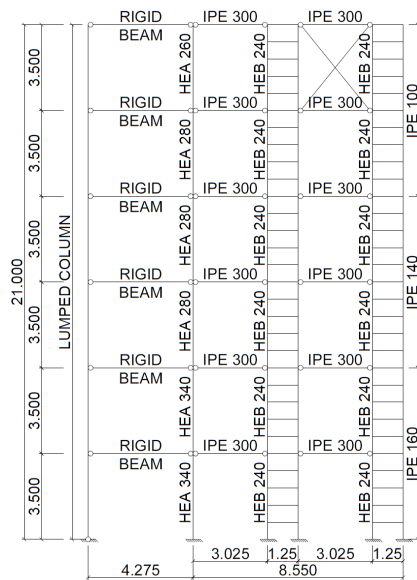
Figure 3.15: DRLF-MS: 2D frame.
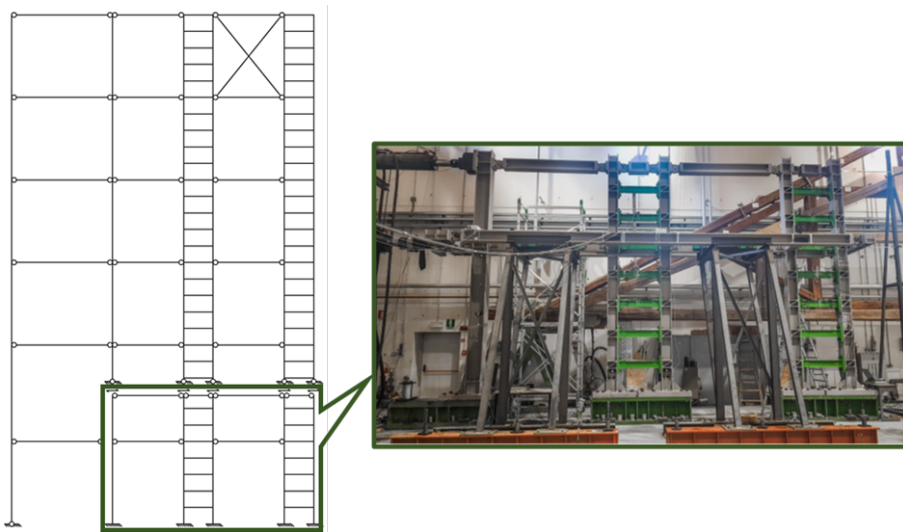
Figure 3.16: DRLF-MS: Substructured frame.

A summary of the comparison between the modal proprieties of the 3D building, the 2D frame and the Substructured Frame (SF), referring respectively to the structures in Figures 3.13, 3.15 and 3.16. is provided in Tables 3.10 to 3.12. In Tables 3.11 and 3.12, the comparisons between

the vibration mode shapes are investigated by using the modal assurance criterion (MAC) [87]. As shown, the two models had the same initial elastic behaviour, as demonstrated by the small discrepancy, lower than the 15%, between the models' periods. Moreover, since the numbers on the diagonal of the MAC matrix are close to 1, it can be stated that the vibration modes matched.

Mode	3D Periods [s]	2D Periods [s]	SF Periods [s]	Error 3D-2D	Error 2D-SF
1	1.52	1.55	1.39	2%	11%
2	0.38	0.39	0.40	1%	1%
3	0.19	0.19	0.19	1%	0%

Table 3.10: DRLF-MS: Modal comparison between 3D building, 2D frame and Substructure.

		2D Frame		
	Mode	**1**	**2**	**3**
3D Building	**1**	1.00	0	0
	4	0	0.99	0
	8	0	0	1.00

Table 3.11: DRLF-MS: MAC matrix between 3D Building and 2D Frame.

		Substructured Frame		
	Mode	**1**	**2**	**3**
2D Frame	**1**	1.00	0	0
	2	0	1.00	0
	3	0	0	0.99

Table 3.12: DRLF-MS: MAC matrix between 2D Frame and Substructured Frame.

As shown in Figure 3.17, pushover analyses highlighted that the non-linear behaviour of the 2D frame and the substructured one are congruent after the yielding of the devices whilst the initial stiffness turns out to be

different, due to the introduction of the discontinuity and the vertical re-
straint on the numerical substructure. Time history analyses were there-
fore performed to investigate the behaviour of the substructure further.
As reported in Figure 3.18, in these analyses the maximum error, eval-
uated as normalized root mean square error (NRMSE) on the bending
moment of the devices is limited for both the transition between three-
dimensional and bi-dimensional and between 2D and the substructured
frame.
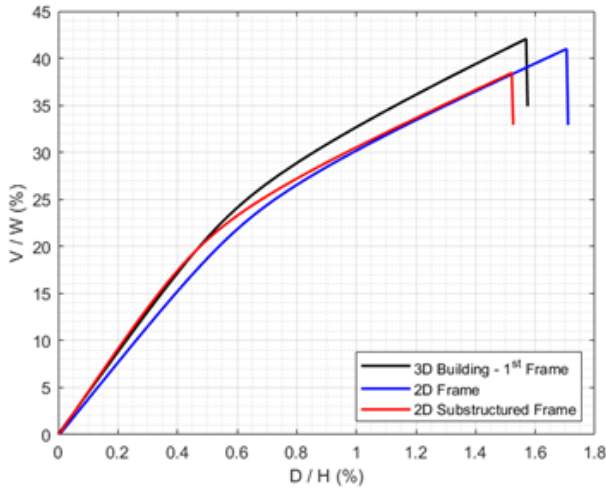
Figure 3.17: DRLF-MS: Push-over comparison.
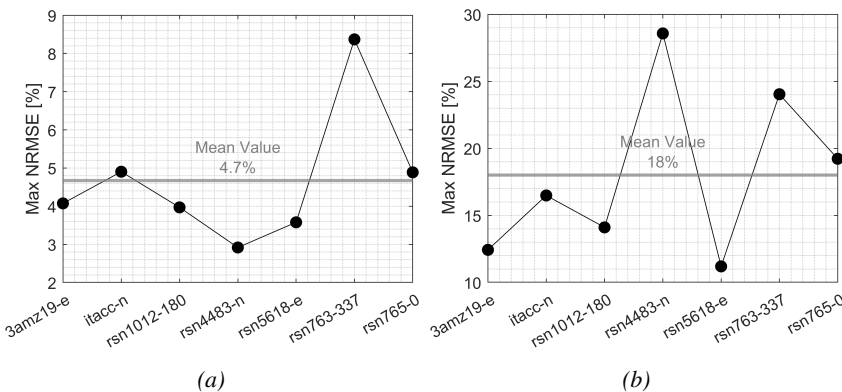
Figure 3.18: DRLF-MS: Maximum NRMSE on the bending moment of the RBSs between (a) 3D-2D and (b) 2D-Substructure.

Aiming to lower the computational burden, the DRLF model was re-

duced to a simplified one. The condensation was performed under the
assumption of shear-type deformation of the structure which led to con-
sidering a system with only seven horizontal degrees of freedom. These
DoFs represented the displacements at each floor level and the one at the
substructuring level. Lumped masses, connected by means of non-linear
shear springs, were located on each DoF. In order to calibrate the non-
linear spring parameters, a displacement control analysis was performed
on the substructures frame by imposing a cyclic displacement at the top
floor of the reference model.
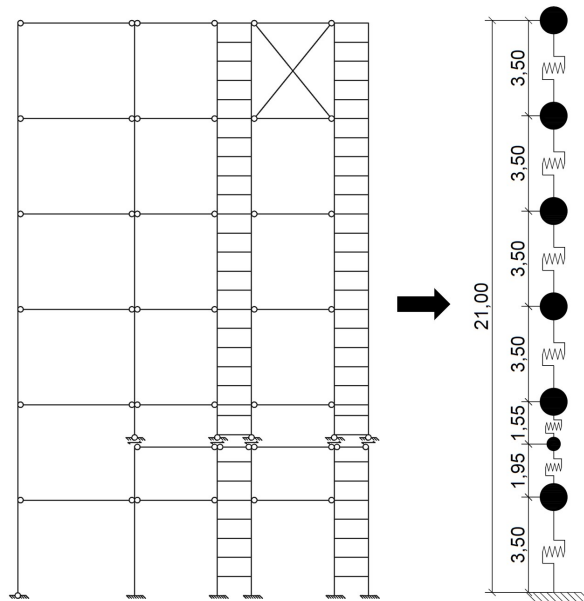
Figure 3.19: DRLF-MS: Model reduction.

3.3.2 DRLF - HSS Building

The prototype building was characterized by a two-span moment resist-
ing frame and a three-span concentrically braced frame scheme in the
two main directions, respectively, equipped with two parallel DRLF sys-
tems and DRBrC components. With the purpose of reducing the system
deformability, high-strength steel beams alternately fixed to the columns,
see Figure 3.20a, were employed in the transversal direction, as sug-
gested in [85, 88, 89]. The investigation examined the use of high-
strength steel for these components due to the high seismic strength de-
mand of the coupling beams, which is required to link two DRLF sys-
tems. Additionally, once the beam links undergo plastic deformation,

the contribution of the coupling beams to the overall stiffness increases, further increasing the demands on the beams.

As for the DRLF-MS building, the design was performed at SD limit state by means of linear dynamic analysis on a finite element model developed in SAP2000.

The dissipative components were designed according to Eurocode 8-3 whilst the non-dissipative elements were checked referring to Eurocode 8-1 and INNOSEIS provisions. To investigate the non-linear behaviour, a reference 3D model was developed in OpenSees. Beams and columns were modelled by means of elasticBeamElements whilst the link beams were modelled, as previously described, concentrating the non-linear behaviour in the RBSs of the beams. To exploit hybrid simulation, the substructuring technique was employed. Following the same procedure of DRLF-MS, the final substructured configuration found was the one depicted in Figure 3.20b. The comparison in terms of modal characteristics between the three level of modelling is reported in Tables 3.13 to 3.15, whilst the non-linear behaviour was compared with a push-over analysis, see Figure 3.21. Both comparisons highlighted a good agreement between models.

Mode	3D Periods [s]	2D Periods [s]	SF Periods [s]	Error 3D-2D	Error 2D-SF
1	1.33	1.26	1.21	5%	4%
2	0.42	0.41	0.42	1%	1%
3	0.21	0.21	0.22	0%	1%

Table 3.13: DRLF-HSS: Modal comparison between 3D building, 2D frame and Substructure.

		2D Frame		
	Mode	1	2	3
3D Building	1	1.00	0	0
	4	0	1.00	0
	8	0	0	1.00

Table 3.14: DRLF-HSS: MAC matrix between 3D Building and 2D Frame.
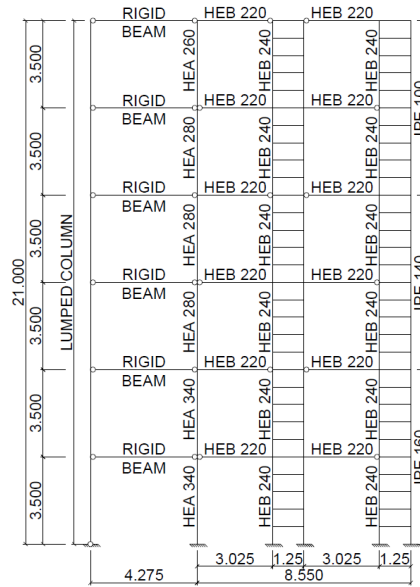
(a) 2D Frame
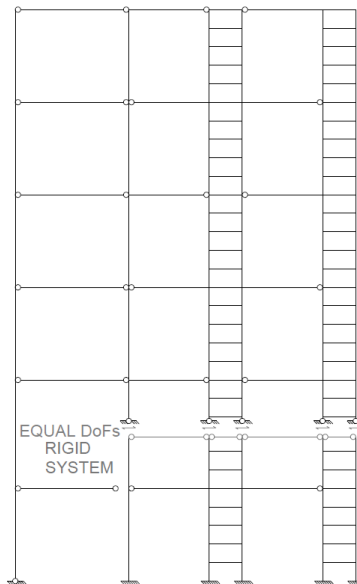
(b) Substructured Frame

Figure 3.20: DRLF-HSS: Bi-dimensional frame: (a) designed profile and (b) substructured.

		Substructured Frame		
	Mode	1	2	3
2D Frame	1	1.00	0	0
	2	0	0.99	0
	3	0	0	1.00

Table 3.15: DRLF-HSS: MAC matrix between 2D Frame and Substructured Frame.
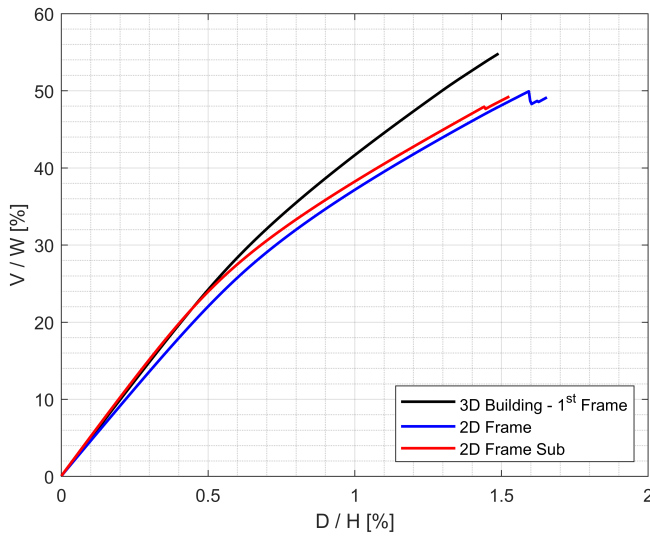
Figure 3.21: DRLF-HSS: Push-over comparison.

As described in Section 3.2.2, the link beams were firstly condensed into shear springs. Subsequently, to further decrease the computational burden, the shear springs of each floor were condensed into one, as depicted in Figure 3.22. The results in terms of push-over curves and time-history analyses at the NC limit state on the three structures are illustrated in Figures 3.23 and 3.24.
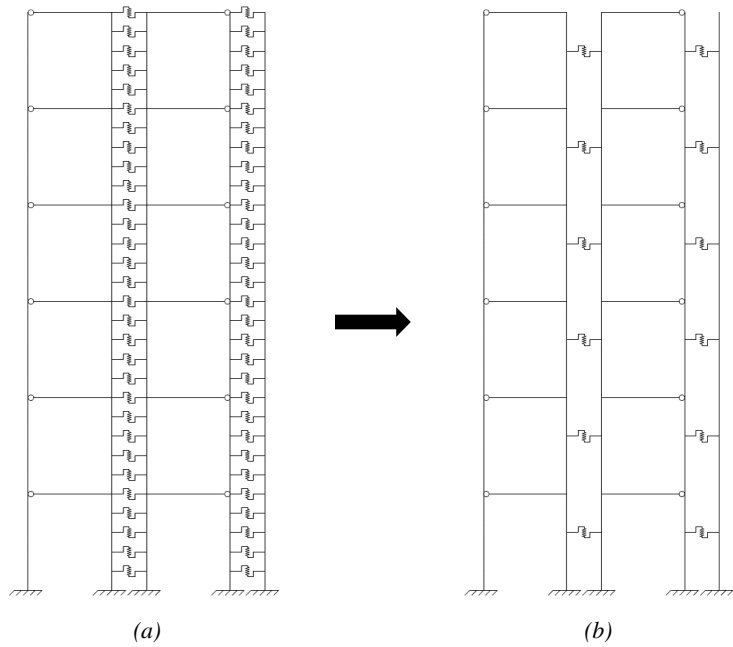
*Figure 3.22: DRLF-HSS: Reduced models: (a) condensed beam links model
and (b) condensed model.*
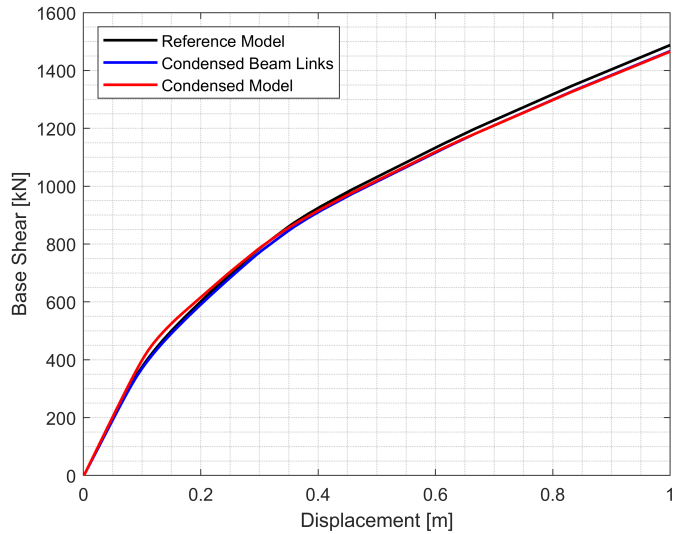
*Figure 3.23: DRLF-HSS: Push-over comparison between reference and re-
duced models.*
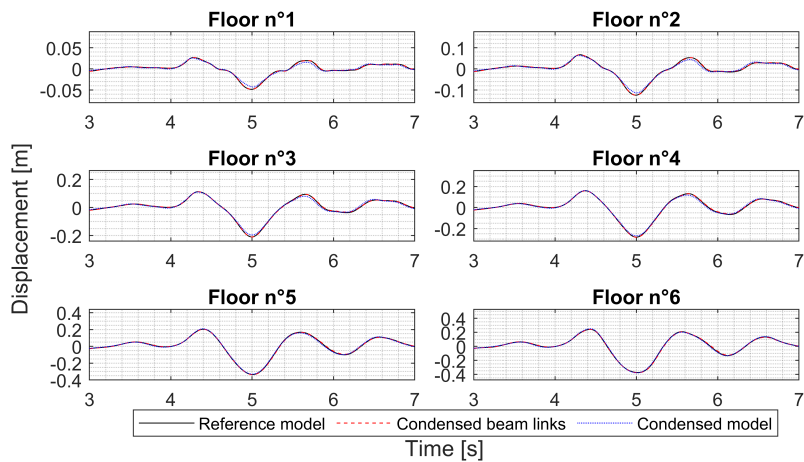
Figure 3.24: DRLF-HSS: Near collapse peak displacement comparison between reference and reduced models.

3.3.3 DRBrC building

The prototype building was characterized by a two-span concentrically braced frame (CBF) equipped with DRBrC and a three-span moment-resisting frame equipped with DRBeS components. The floor was designed as a concrete deck connected through shear studs to the beams of the MRFs, to develop the composite action in the transversal direction. The building was designed according to INNOSEIS provisions, for the dissipative replaceable components, and to the European standards for all the non-dissipative members. In the OpenSees model, elastic beam-column elements were adopted for the beams, columns and braces. In contrast, the DRBrC components were modelled exploiting twoNodeLinks elements in which the axial material assigned was the Pinching4 material. As for the previous prototypes of buildings, for validating the different steps of modelling, i.e. 3D building, 2D frame and 2D substructured frame, comparisons in terms of modal analyses, reported in Table 3.16, and push-over analysis were performed. As depicted in Figure 3.25c, the 2D frame was divided for substructuring at the first-floor level since the bending moment in continuous columns of CBFs is negligible.
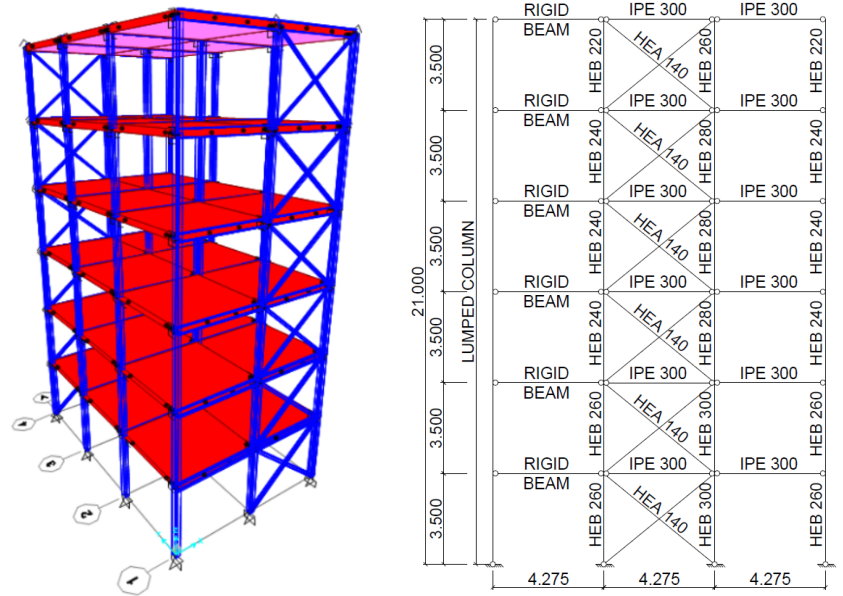
(a) 3D Building.

(b) 2D Frame.
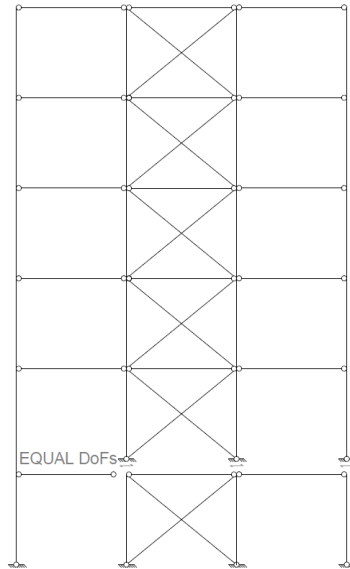
(c) Substructured Frame.

Figure 3.25: DRBrC: (a) 3D model, (b) 2D frame and (b) substructured frame.

Mode	3D Periods [s]	2D Periods [s]	SF Periods [s]	Error 3D-2D	Error 2D-SF
1	0.99	0.99	0.90	0%	9%
2	0.32	0.33	0.33	3%	0%
3	0.20	0.20	0.20	0%	0%

Table 3.16: DRBrC: Modal comparison between 3D building, 2D frame and Substructure.

3.3.4 DRBeS building

The prototype building is composed of six storey and two-span moment-resisting frame equipped with DRBeS components and a three-span concentrically braced frame equipped with DRBrC. At the moment resisting frame direction, composite beams were employed where the beams were made of an IPE270 steel section and a concrete slab 150 mm thick with a C25/30 strength class. The steel sheeting adopted was a 55 mm high corrugated. To obtain the composite action, Nelson studs were exploited, ensuring a full shear connection between the steel profile and the composite slab. The transverse reinforcements of the composite slab, with a diameter of $\phi = 16$ mm, as well as the shear studs, whose diameter was found equal to $\phi = {}^5\!/_8$ in were designed according to Eurocode 4 [90]. Finally, as it can be noticed from Figures 3.26b and 3.26c, no lumped column was needed in this specific case since DRBeS devices were mounted on each longitudinal frame.

Mode	3D Periods [s]	2D Periods [s]	SF Periods [s]	Error 3D-2D	Error 2D-SF
1	1.42	1.38	1.32	10%	3%
2	0.44	0.44	0.42	0%	5%
3	0.24	0.25	0.25	4%	0%

Table 3.17: DRBeS: Modal comparison between 3D building, 2D frame and Substructure.

(a) 3D Building.

(b) 2D Frame.

(c) Substructured Frame.
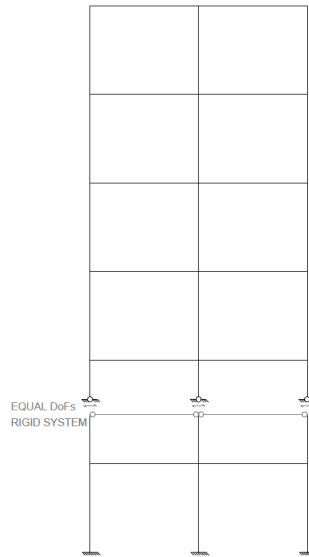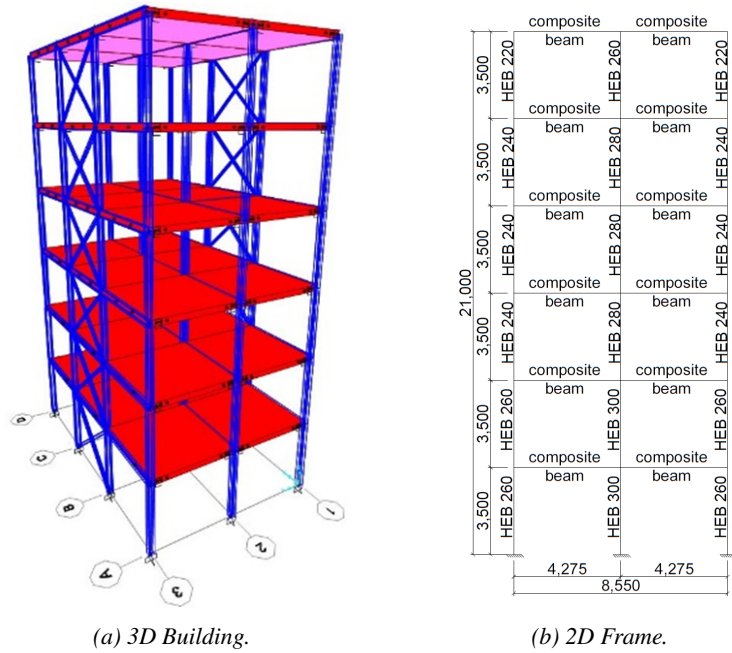
Figure 3.26: DRBeS: (a) 3D model, (b) 2D frame and (b) substructured frame.

3.3.5 Implementation for experimental environment

Since the hybrid test technique implies physically testing only a part of the prototype structure, the numerical model of the remainder of the structure was required. The latter can experience non-linear behaviour, and thus, accurate modelling of such non-linearities is needed. Moreover, it was impossible to extract from OpenSees mass, stiffness and damping matrices of the structures which were required to perform hybrid tests.

In this respect, a finite element software specifically conceived for hybrid testing was developed by the University of Aarhus and the University of Trento in the MATLAB [91] environment in order to exploit the Simulink package to control the actuators. The existing library already presents elastic and non-linear beam elements. To accurately reproduce the cyclic behaviour of the DRCs, the implementation of twoNodeLink elements similar to the one available in OpenSees was deemed necessary.

This element, called by analogy two-node link, is defined with three springs, each of which acts along a different degree of freedom. Since the element has a non-zero length, coupling between the transversal and the rotational degrees of freedom is needed to achieve the equilibrium of the element. The element was implemented in the two-dimension environment by defining a stiffness matrix of size 6x6, indicated in Equation 3.5.

$\mathbf{K} =$

$$
\begin{bmatrix}
K_A & 0 & 0 & -K_A & 0 & 0 \\
0 & K_S & K_S \dfrac{l}{2} & 0 & -K_S & K_S \dfrac{l}{2} \\
0 & K_S \dfrac{l}{2} & K_M + K_S \dfrac{l^2}{4} & 0 & -K_S \dfrac{l}{2} & -K_M + K_S \dfrac{l^2}{4} \\
-K_A & 0 & 0 & K_A & 0 & 0 \\
0 & -K_S & -K_S \dfrac{l}{2} & 0 & K_S & -K_S \dfrac{l}{2} \\
0 & K_S \dfrac{l}{2} & -K_M + K_S \dfrac{l^2}{4} & 0 & -K_S \dfrac{l}{2} & K_M + K_S \dfrac{l^2}{4}
\end{bmatrix}
$$

$$(3.5)$$

In addition, an explicit implementation of the Bouc-Wen hysteretic displacement was needed for the finite element software in MATLAB environment, see Equation 3.6. In order to use the two-node link element, tangent stiffness should also be evaluated as reported in Equation 3.7 where the hysteretic tangent stiffness k_{bw} is computed in Equation 3.8.

$$z_{i+1} = z_i + \frac{1 - \nu \, |z_i|^n \, [\beta \, sign \, (z_i \, du_i) + \gamma]}{\eta} du_i \tag{3.6}$$

$$k_{i+1} = \alpha \, k_0 + k_{bw(i+1)} \tag{3.7}$$

$$k_{bw(i+1)} = (1 - \alpha) \, k_0 \, \frac{1 - \nu \, |z_{i+1}|^n \, [\beta \, sign \, (z_{i+1} \, du_i) + \gamma]}{\eta} \tag{3.8}$$

Finally, the four structures were implemented in the in-house finite element software to obtain mass, stiffness and damping matrices. The new models were compared with the OpenSees once through modal and push-over analyses to ensure consistency.

3.4   Ground motion selection

The seismic response of the frame was investigated through a series of hybrid tests with increasing return periods of the seismic actions, which correspond to three different limit states, namely damage limitation, significant damage and near collapse. Table 3.18 summarizes the main characteristics of the accelerograms.

Limit state	a_g [g]	T_R [years]
DL	0.200	60
SD	0.360	475
NC	0.504	1600

Table 3.18: Limit State characteristics.

The test programme was conducted as follows:

- Test at DL limit state. After the test, the elastic behaviour of dissipative components and the structural members was checked.

- Test at SD limit state. After the test, the elastic and inelastic behaviour of structural members and the dissipative components respectively were checked.

- The beam links were replaced with new ones. The self-centring capacity of the prototype building was verified, and the residual inter-storey drift was measured.

69

- Test at NC limit state. After the test, the inelastic behaviour of structural members and dissipative components, respectively, were checked.

A set of seven triaxial accelerograms was analysed for each limit state, to choose the most suited to conduct the test. The criteria of consistent structural performance and minimizing the errors between monolithic, i.e. the full frames with no substructuring, and substructured frames were considered. Moreover, spectral compatibility, in accordance with the provisions of the new Eurocode 8-1 draft [84], was checked, i.e.:

- the compatibility is checked among the period ranges $[0.2T_{1x} - 1.5T_{1x}]$ and $[0.2T_{1y} - 1.5T_{1y}]$, being T_{1x} and T_{1y} the fundamental periods of the 3D building along the two main directions.

- in these ranges, the average of the 5% damped GM response spectra shall fall between 0.75 and 1.3 times the target spectrum, considered as the elastic spectrum defined by Eurocode 8-1;

- in the same ranges, the average value of the ratio between the average of the GMs and the target spectrum shall be greater than 0.95;

- in the same ranges, the 5% damped GM response spectrum of each accelerogram shall not fall below 50% of the target spectrum;

where GM is defined as in Equation 3.9 in which $S_{e,X}$ and $S_{e,Y}$ are, respectively, the X and Y spectral acceleration components of the ground motion.

$$GM = \sqrt{S_{e,X} \cdot S_{e,Y}} \qquad (3.9)$$

Furthermore, errors between the response of the monolithic frame and the substructured frame for each of the selected accelerograms were considered to quantify the discrepancies. The following were computed for each record:

- percentage error on the total hysteretic energy dissipated by the structure;

- statistical indicators on bending moment history on reduced beam sections.

The aforementioned error indicators are computed as indicated in Equations 3.10 to 3.12.

$$Energy\ Error = \frac{|E_i - E_j|}{E_j} \tag{3.10}$$

$$NRMSE = \frac{\|x_i - x_j\|_2/\sqrt{N}}{x_{j,max} - x_{j,min}} \tag{3.11}$$

$$NEnErr = \left| \frac{\|x_i\|_2 - \|x_j\|_2}{\|x_j\|_2} \right| \tag{3.12}$$

The energy error in Equation 3.10 is a percentage difference between
two scalar quantities, i.e., the hysteretic energy dissipated by the devices.
The parameters reported in Equations 3.11 and 3.12, both expressed in
terms of percentage, compare two datasets, i and j, in which the j dataset
is taken as a reference. The normalised root mean square error (NRMSE)
is sensitive to frequency while the normalised energy error (NEnErr) to
amplitude [92].

3.4.1   DRLF Frames

To evaluate the structural performance, the maximum rotation achieved
by RBSs was considered, see Figure 3.27 for MS frame and Figure 3.28
for HSS frame. For each limit state, consistency was checked, e.g., all
the RBSs attained a maximum rotation lower than the yielding rotation
for the DL limit state, Figures 3.27a and 3.28a. Moreover, a uniform
dissipative behaviour in addition to a maximum rotation of the sections
compatible with the considered limit state was achieved for both the SD
and the NC limit states, see Figures 3.27b and 3.28b and Figures 3.27c
and 3.28c. It should also be highlighted that for for the frame with mild
steel beams, (MS), the increase in stiffness given by the bracing system
caused small rotations of the last floor RBSs.
The mean errors among all the devices for the selected accelerogram are
listed in Tables 3.19 and 3.20.

Lastly, for each limit state, the spectral compatibility was satisfied as
illustrated in Figures 3.29 and 3.30. From both Figures 3.29c and 3.30c,
it can be noted that the selected ground motion for NC limit state was a
pulse-like record and did not respect the imposed limits within the sig-
nificant range of periods. However, Eurocode 8-1 draft allows for the
use of such accelerograms, hence it was employed to obtain structural
damage substantially different from the one at the SD limit state.

(a)   *(b)*

(c)
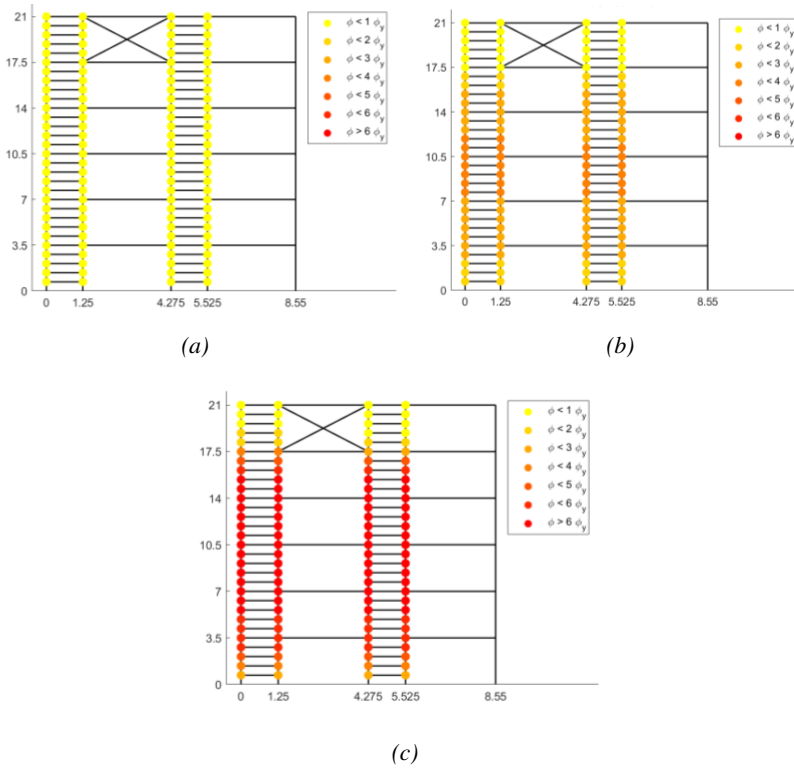
Figure 3.27: DRLF-MS: Maximum RBSs rotation for chosen accelerograms at (a) DL, (b) SD and (c) NC limit state.

Parameters [%]	DL	SD	NC
Energy Error	/	57.28	29.09
NRMSE Bending Moment	13.55	11.38	4.37
NEnErr Bending Moment	25.78	15.27	30.46

Table 3.19: DRLF-MS: Parameters error between monolithic and substructured frame responses.

72

(a) *(b)*

(c)
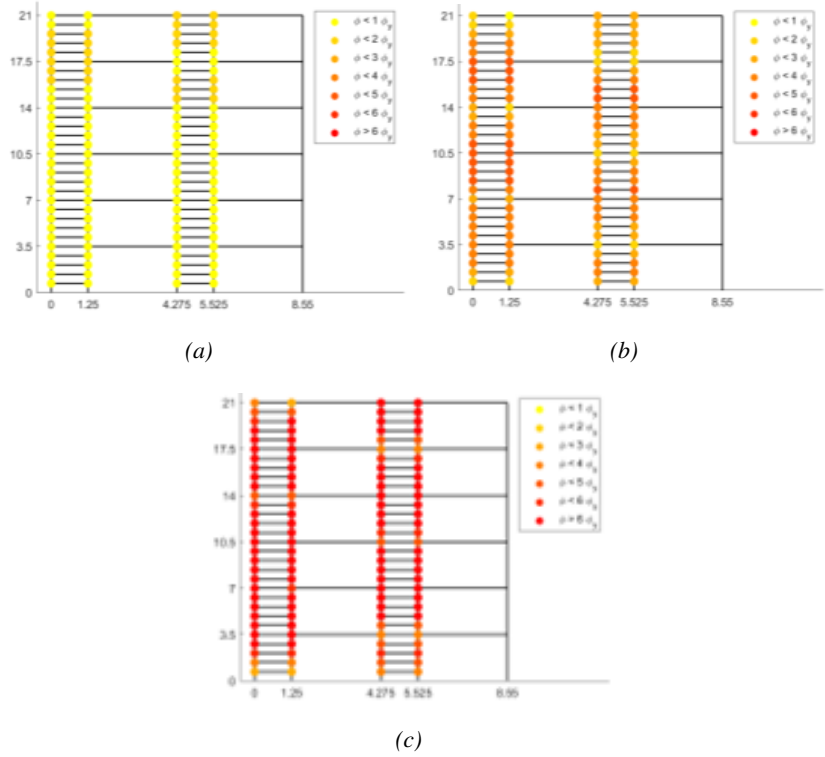
*Figure 3.28: DRLF-HSS: Maximum RBSs rotation for chosen accelerograms at
(a) DL, (b) SD and (c) NC limit state.*

Parameters [%]	DL	SD	NC
Energy Error	/	47.64	27.42
NRMSE Bending Moment	7.43	13.40	8.17
NEnErr Bending Moment	5.37	9.52	16.85

*Table 3.20: DRLF-HSS: Parameters error between monolithic and substruc-
tured frame responses.*
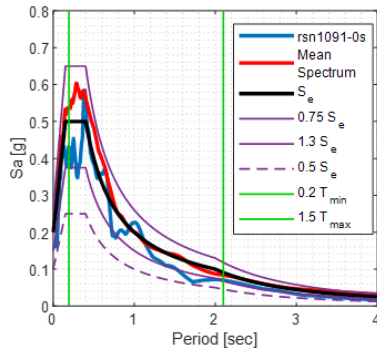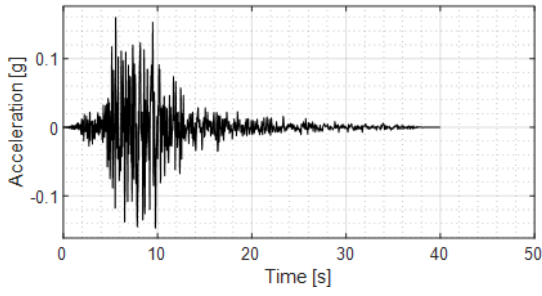
(a) DRLF-MS: DL accelerogram – rsn763-s.
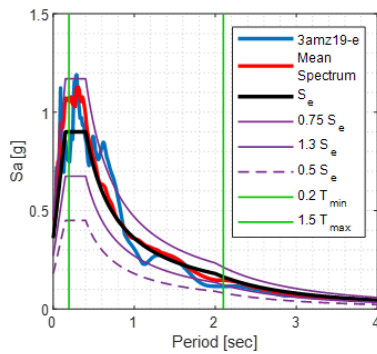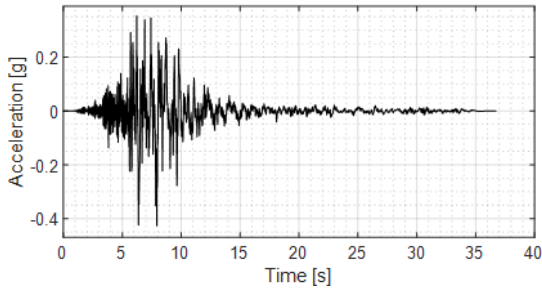
(b) DRLF-MS: SD accelerogram – rsn4483-e.
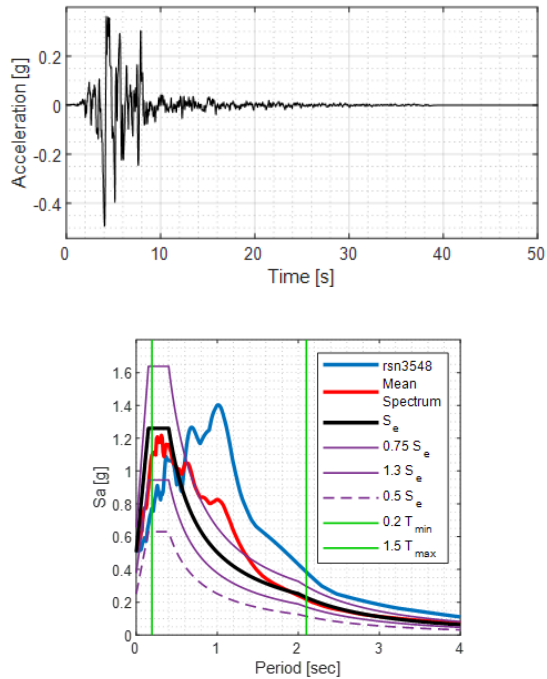
(c) DRLF-MS: NC accelerogram - rsn3548-N.

Figure 3.29: DRLF-MS: Selected accelerograms and spectro-compatibility.
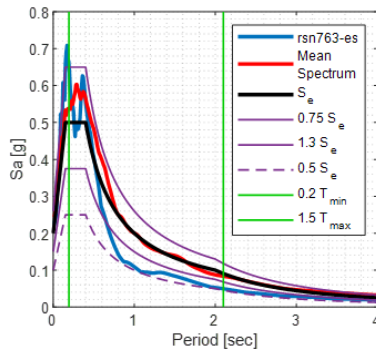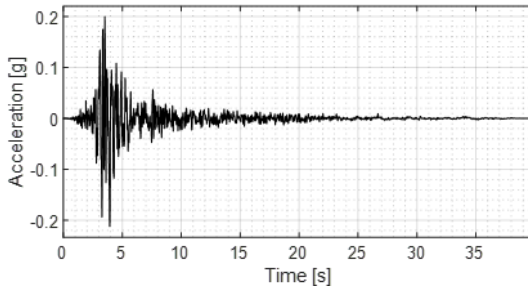
(a) DRLF-HSS: DL accelerogram – rsn1091-90s.
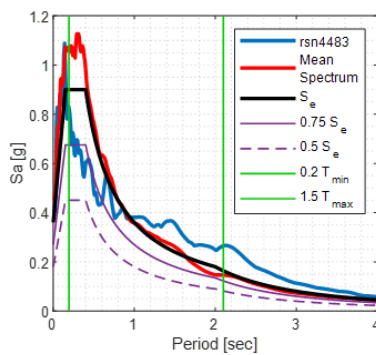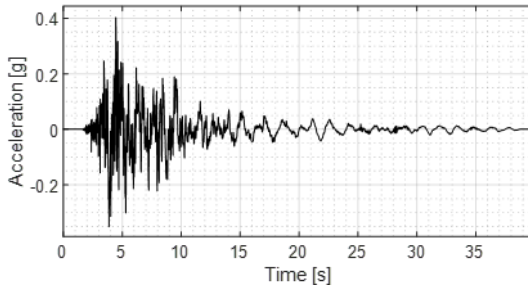
(b) DRLF-HSS: SD accelerogram – 3amz19-e.
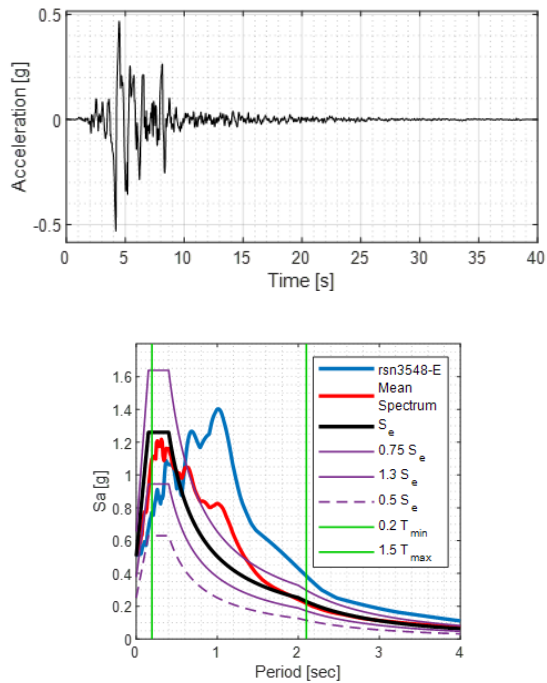
(c) DRLF-HSS: NC accelerogram - rsn3548-E.

Figure 3.30: DRLF-HSS: Selected accelerograms and spectro-compatibility.

3.4.2 DRBrC Frame

The selected accelerograms for hybrid tests on DRBrC structures are depicted in Figure 3.31. The discrepancy between the 2D monolithic frame and the 2D substructured frame in this specific case was quantified by means of Equations 3.10 to 3.12 considering:

- the total base shear history;

- the axial force history in the DRBrC components on the first floor;

- the horizontal displacement history of the first. floor

Concerning the criteria of the consistent structural performance, the maximum axial loads obtained for each DRBrC connection at the first floor were considered, see Table 3.21. This was compared with the yield load, i.e. $P_y = 123.3$ kN for evaluating the structural performance at each limit state. At DL limit state, the yield limit is slightly exceeded, 7.6%, while for both SD and NC limit states, the axial forces are such to induce significant plastic deformations.
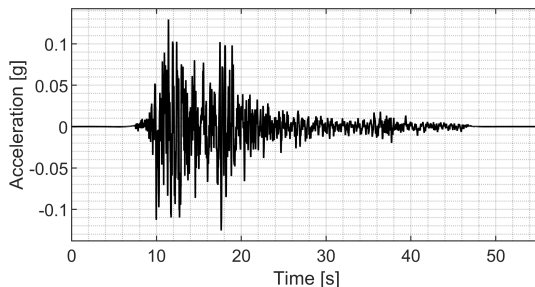
(a) DRBrC: DL accelerogram – euula-ns.
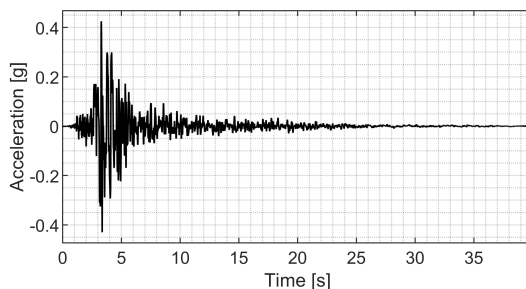
(b) DRBrC: SD accelerogram – rsn763-067.
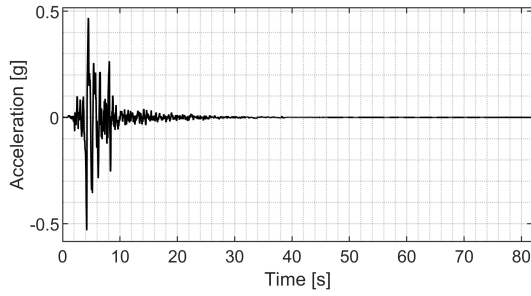
(c) DRBrC: NC accelerogram - rsn3548-E.

Figure 3.31: DRBrC: Selected accelerograms.

Axial Forces	DL	SD	NC
1st Device	132.41	234.75	339.28
2nd Device	132.34	234.83	339.35
3rd Device	132.66	234.79	339.32
4th Device	132.37	234.79	339.33

Table 3.21: DRBrC: Maximum estimated axial force in kN on the 1st floor.

3.4.3 DRBeS Frame

For the DRBeS structure, the selected accelerograms are reported in Figure 3.32. In this case, the differences between the 2D frame and the substructured one were computed with the respect to:

- the total base shear history;

- the bending moment history on the connections on the first floor;

- the horizontal displacement history of the first floor.
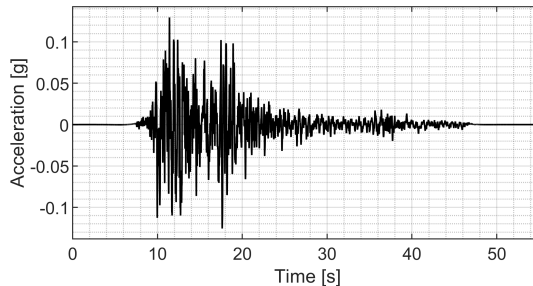
(a) DRBeS: DL accelerogram – euula-ns.

79
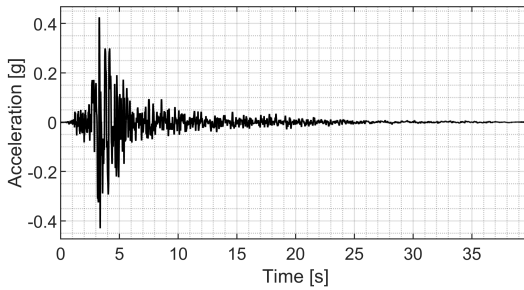
(b) DRBeS: SD accelerogram – rsn763-067.
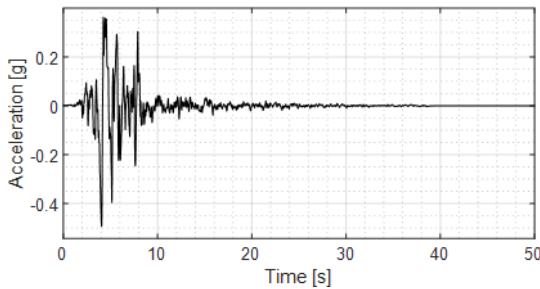
(c) DRBeS: NC accelerogram - rsn3548-E.

Figure 3.32: DRBeS: Selected accelerograms.

3.5 Conclusions

In this Chapter, the investigated devices were thoroughly described concerning their geometrical and mechanical characteristics. Moreover, the numerical models exploited for performing preliminary analyses on the prototype buildings were comprehensively illustrated.

In addition, the numerical models of the prototype buildings were shown together with the results of the preliminary analyses. As shown from modal, pushover and time history analysis, the 2D frame well represents the global behaviour of the 3D building. Since only two actuators could be activated simultaneously, the substructuring method was exploited, allowing for reducing the number of degrees of freedom to control. To study the substructured configuration, a hinge and a vertical constraint had to be inserted in the actuator position. The analysis results showed that the identified substructures well represent the behaviour of the bi-dimensional frames.

Finally, the procedure for choosing the most suited accelerograms for performing hybrid simulations was described.

Chapter 4

Hybrid simulation tests results

This Chapter describes the results of the experimental campaign at the University of Trento carried out on five specimens equipped with three types of DRCs. The prototype buildings investigated were extensively described in Chapter 3. As for the previous Chapter, more importance has been given to the results of frames equipped with DRLF systems. However, outcomes of tests on DRBrC and DRBeS frames were also briefly presented, while additional information can be found in the articles [52] and [53] and in Andreotti's PhD thesis [70].

4.1 General considerations

As mentioned in Chapter 2, in this work, the PG-α algorithm was implemented to solve the equation of motion. Since the pseudo-dynamic method was used, different values of time scale factor λ, Equation 2.1, were chosen for the three different limit states. In particular, 50 was selected for the test at DL limit state, whilst 100 was for SD and NC tests. To impose the same displacement at the top of each column, beams with high axial stiffness were placed at the level of the top actuator. Furthermore, since applying a relevant axial force on the devices would have affected their response, two rigid axial beams were laterally placed at the floor level, as depicted in Figure 4.1. This allowed also to replicate a rigid diaphragm. In addition, a truss system was adopted to brace the frame and prevent any out-of-plane instability.

The computational model of the physical substructure was condensed to single or two degrees of freedom, respectively, for DRBrC frames and

all other structures, depending on the number of actuators used to per-
form the tests. The degrees of freedom corresponded to the horizontal
displacements controlled by the actuators.
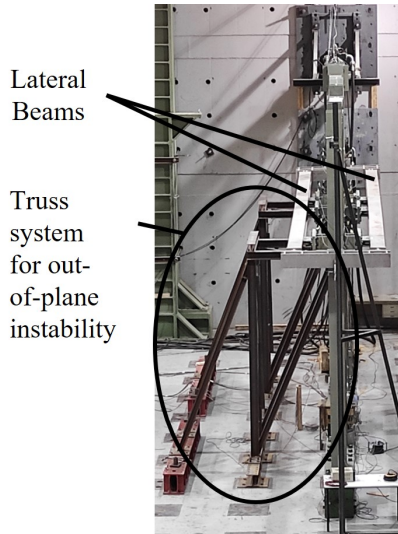
(a)
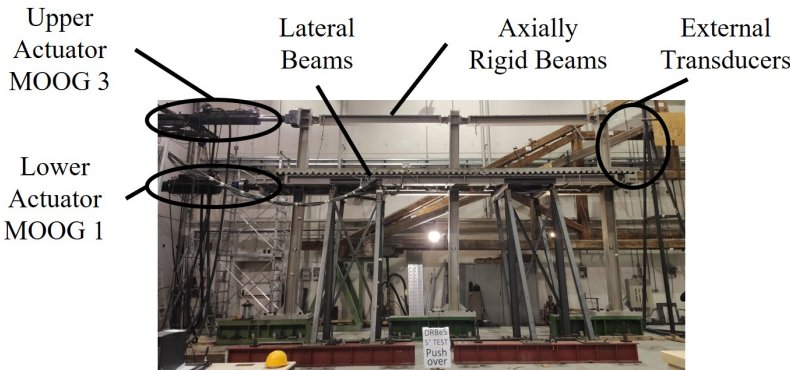
(b)

Figure 4.1: Experimental test set-up: (a) lateral and (b) front view.

4.2   DRFL - MS Frame

In this Section, the outcomes of the tests conducted on DRLF mild steel
frame are thoroughly presented. In particular, the test setup is first de-
scribed, and subsequently, the results of the tests at the three different

limit states are illustrated.

4.2.1 Hybrid test configuration

As mentioned in Section 3.3.1, the selected substructured configuration involved using two actuators in the test set-up. The physical substructure of the frame, depicted in Figure 4.2, was composed of five columns in which the left one was not part of the DRLF systems whilst the others, coupled with the link beams, constituted the two shear walls that carry the horizontal loads.
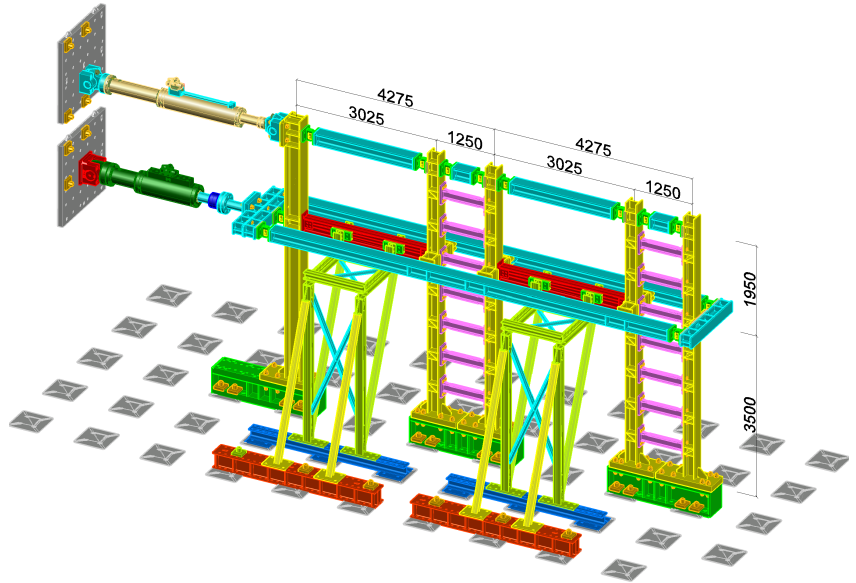
Figure 4.2: DRLF-MS: Experimental test set-up.

Figure 4.3 depicts the instrument configuration: eleven sections were instrumented by means of both strain gauges and displacement transducers. The former were positioned outside the dissipative zone, in an elastic region near the RBS, to estimate the bending moment. In this respect, the upper and the lower edge of the section were instrumented to measure the strain. Indeed, the curvature could be calculated by assuming plane sections as the ratio between the total deformation of the section, i.e., the difference between the strains measured at the top ε_{top} and the ones measured at the bottom ε_{bot}, and the height of the cross-section H_{sec}.

$$\chi = \frac{\varepsilon_{top} - \varepsilon_{bot}}{H_{sec}} \tag{4.1}$$

An estimate of the bending moment on each instrumented section

could be obtained using the Euler-Bernoulli beam theory. In the following formula, I_{beam} is the modulus of inertia of the gross section, and E_s is Young's steel modulus.

$$M = E_s \, I_{beam} \, \chi \tag{4.2}$$

By assuming the prevalence of the seismic actions with respect to the gravity loads on the devices, it was possible to assume a linear bending moment diagram and thus obtain the bending moment at RBSs by linear interpolation from the bending moments in the elastic range. Moreover, the rotation of the reduced beam sections was calculated from the measurements of the displacement transducers:

$$\varphi = \frac{\Delta_{top} - \Delta_{bot}}{H_{sec}} \tag{4.3}$$

where Δ_{top} and Δ_{bot} are, respectively, the top and the bottom relative displacements of the RBSs. Finally, two inclinometers were applied on the first column to calculate the base bending moment and to evaluate whether the column remained in the elastic range.

(a)   *(b)*

(c)
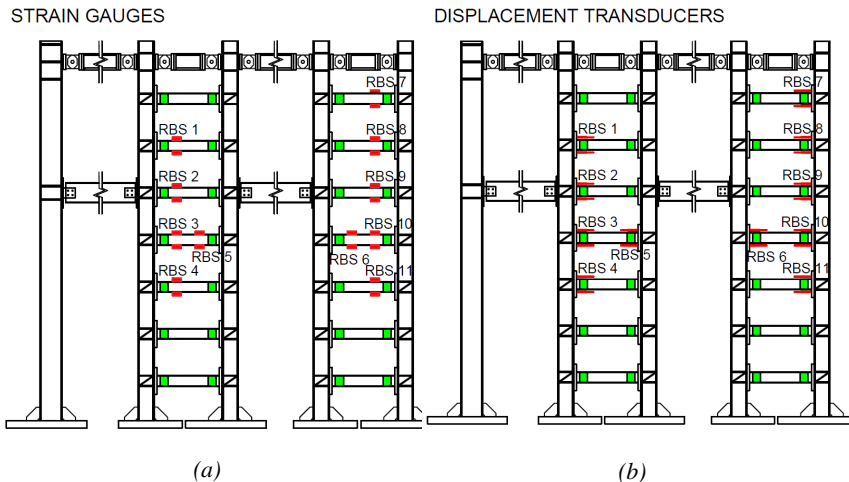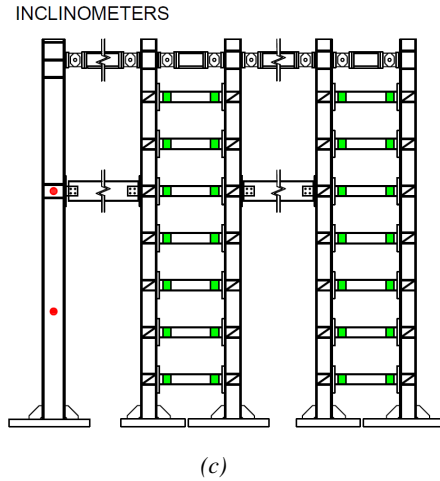
*Figure 4.3: DRLF-MS: Configuration of instrumentation system (a) strain
gauges, (b) displacement transducers and (c) inclinometers locations.*

Figure 4.4: DRLF-MS: Pictures of the instrumentation system.

4.2.2   Description of the results

Damage Limitation limit state

At the Damage Limitation limit state, the elastic behaviour of the structure was verified for both the primary elements and the dissipative components. Indeed, the instrumentation on the beam's sections highlighted that the maximum bending moment attained during the test was the 37.5% of the yielding limit, as depicted from Figure 4.5.

Since the first column of the frame did not belong to the DRLF system, it was the one that suffered the highest bending moment at its base. Moreover, it was also part of the primary elements that could not be replaced after an earthquake. For these reasons, the bending moment at the base of the column was computed from the inclinometers' measures. As
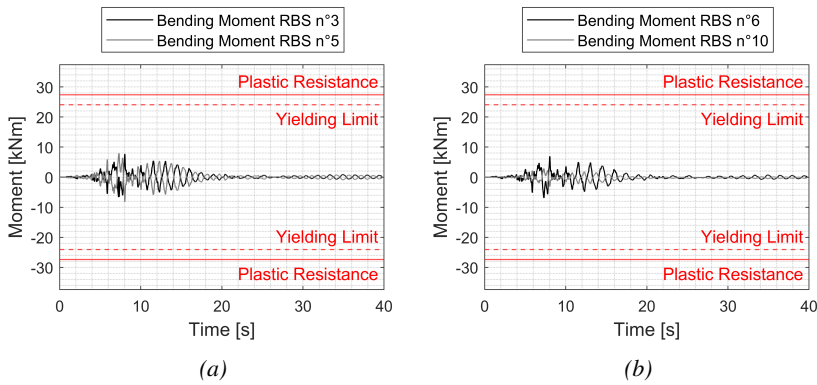
Figure 4.5: DRLF-MS: DL - Bending moment of the RBSs on the first floor at the (a) first beam link (b) second beam link.

depicted in Figure 4.6, the maximum bending moment did not exceed the yielding limit, confirming that it remained in the elastic range.
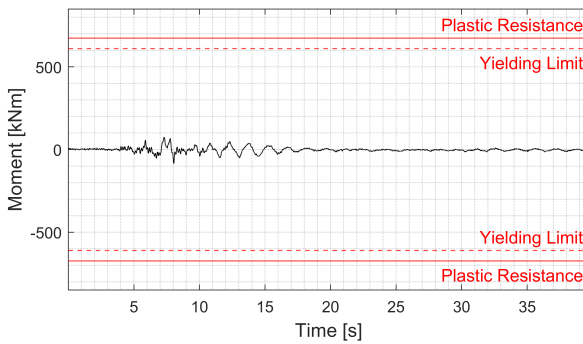
Figure 4.6: DRLF-MS: DL - Bending moment at the base of the first column.

Significant Damage limit state

For the Significant Damage limit state, the structure suffered plastic deformation localized on the RBSs of the beam links. The results in terms of displacement of the two actuators are reported in Figure 4.7. The maximum displacement attained at the floor level was 19.79 mm, corresponding to a peak interstorey drift ratio (PIDR) of 0.57%, whereas the residual displacement after the test was equal to 1.33 mm. This value corresponds to the 0.04% of PIDR, which demonstrates the re-centring capability of the structure and, as an important consequence, the easy replacement of the beam link. Indeed, the physical beam links were ac-

tually replaced after the SD limit state test. Owing to residual drifts,
local usage of jacks was needed to obtain sufficient spacing to substi-
tute the elements. The repair/substitution phase was completed by three
technicians in a working time of 18h (6 hours/men). The bending mo-
ment time-history of the first column, depicted in Figure 4.8, shows that
the yield limit was not exceeded even for the SD limit state, confirming
that the column remained elastic, which is a favourable outcome of the
project. Indeed, the structure was designed for the SD limit state. This
result confirms the DISSIPABLE components' capability to protect the
frame's irreplaceable parts, i.e., beams and columns.

The local behaviour of selected RBSs is reported in terms of bending mo-
ment time histories: it can be noticed that most of the sections yielded
at SD limit state, see Figures 4.9a to 4.9c, nevertheless, some RBSs re-
mained elastic, Figure 4.9d. Finally, since an out-of-plane rotation of the
RBSs was detected, an additional transducer was employed to quantify
this phenomenon for the Near Collapse limit state test.
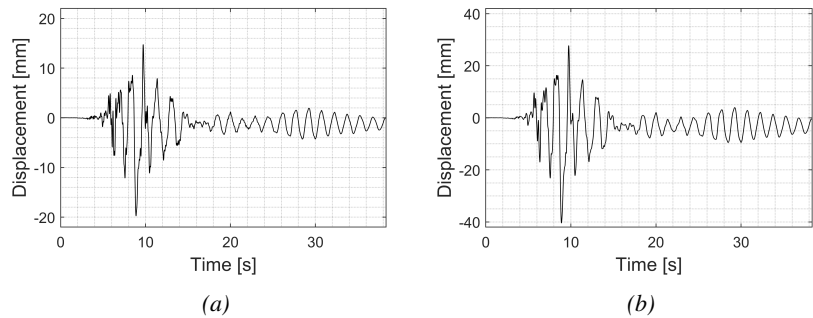
*Figure 4.7: DRLF-MS: SD - Actuator's displacements: (a) MOOG1 (b)
MOOG3.*

Near Collapse limit state

A marked non-linearity for the Near Collapse limit state characterized
the structural behaviour. As demonstrated by the moment-rotation dia-
gram reported in Figure 4.10, the RBSs underwent a significant plastic
deformation, with a 5 mrad residual rotation. Moreover, strength degra-
dation can be noticed by the cycles. This could be due to the interaction
between the bending moment along the strong axis M_y and the bend-
ing moment along the weak axis M_z. As Figure 4.11 shows, the dis-
placements at the top flange of RBS n°10 are different on the two edges,
demonstrating the presence of an out-of-plane rotation. The history over
time of the bending moments M_y and M_z is reported in Figure 4.12
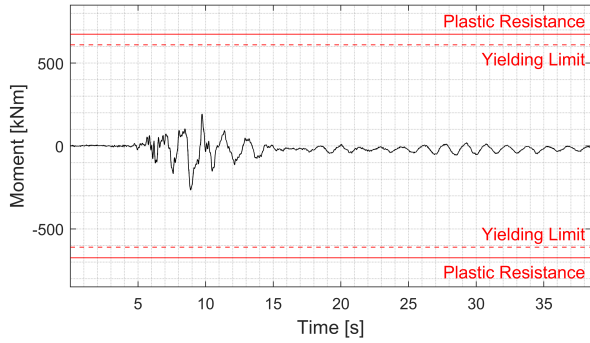
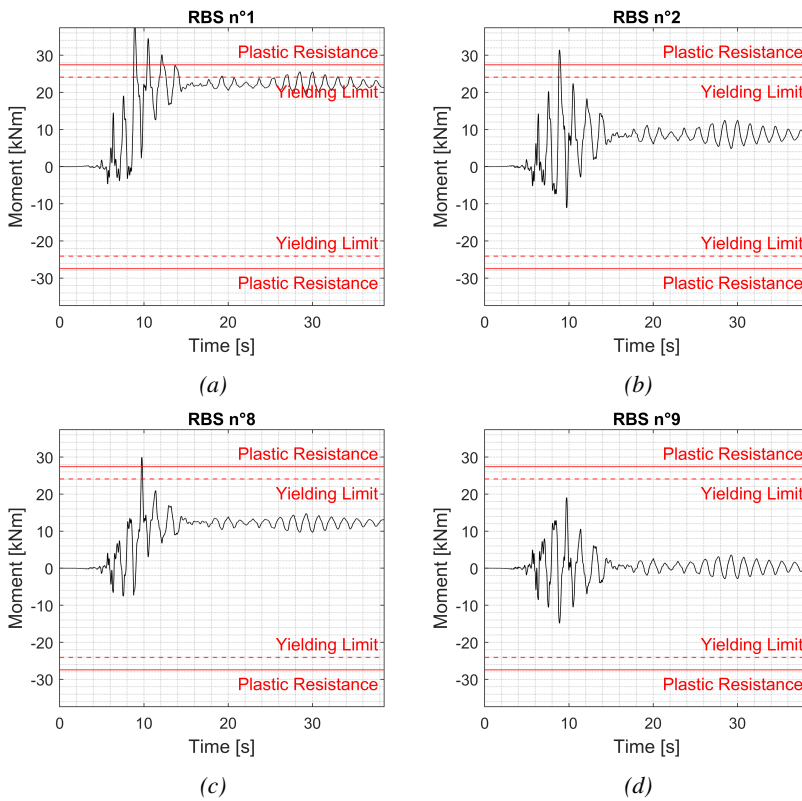*Figure 4.8: DRLF-MS: SD - Bending moment at the base of the first column.*

Figure 4.9: DRLF-MS: SD - Bending moment on selected RBSs.

where the resisting plastic bending moments along the two axes were
computed without considering the interaction. It can be noticed that the
maximum value of both M_y and M_z exceeded the plastic resistance, even
without considering the reduction of resistance due to the interaction. In
Figure 4.13, the evolution of the (M_z, N, M_y) state for the hybrid test at
NC limit state, is compared with the interaction domain, as defined in
Eurocode 3 [93].
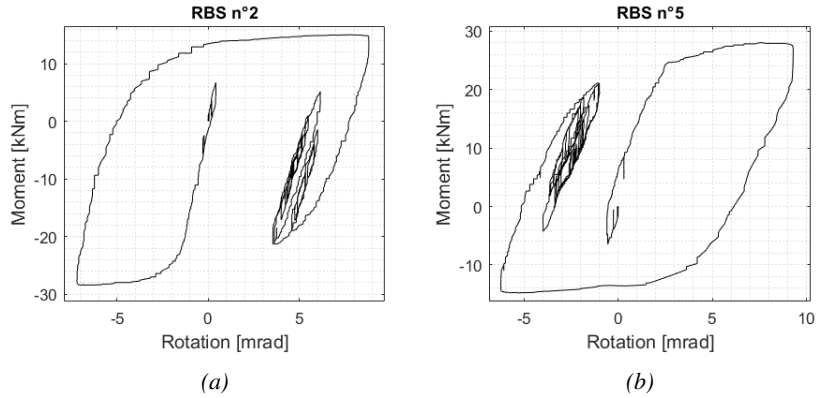
Figure 4.10: DRLF-MS: NC - Bending moment on RBS (a) n°2 and (b) n°5.
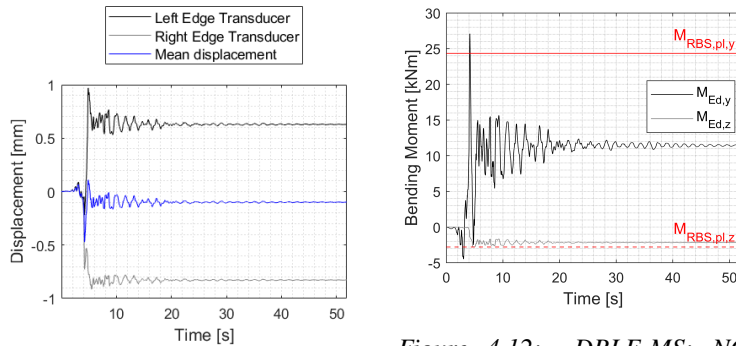
*Figure 4.11: DRLF-MS: NC - Out-
of-plane displacement recorded.*

*Figure 4.12: DRLF-MS: NC -
Bending moment along the two
principal axes.*

Concerning the displacement of the two actuators, reported in Fig-
ure 4.14, the maximum displacement achieved at the floor level was
31.61 mm, corresponding to PIDR of 0.90%. From Figure 4.15, which
shows the bending moment history at the base of the first column, it can
be appreciated that the bending moment did not exceed the plastic limit
for the NC limit state test. This emphasizes the protection the devices
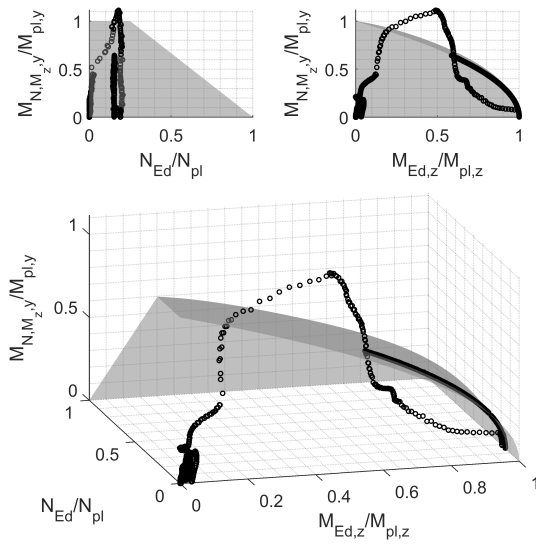
Figure 4.13: DRLF-MS: NC - N-Mz-My Interaction domain according to Eurocode 3.

provide to the structure in case of higher earthquake intensity than the design one.
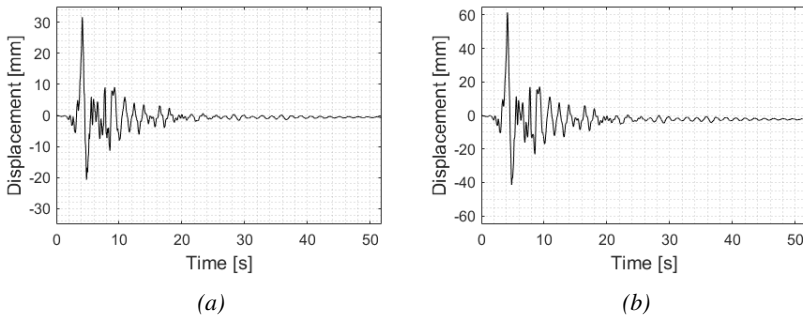
Figure 4.14: DRLF-MS: NC - Actuator's displacements: (a) MOOG1 (b) MOOG3.
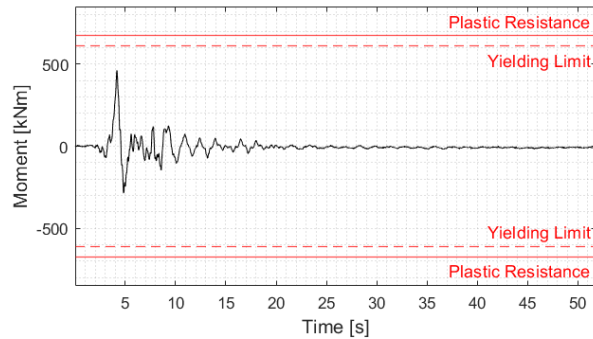
Figure 4.15: DRLF-MS: NC - Bending moment at the base of the first column.

4.2.3 Experimental-based calibration of the non-linear spring models

In the preliminary phase of the work, aiming to choose the ground motion records and to perform the test, a non-linear finite element (FE) model of the structure was developed. Thereafter, the results of the experimental tests previously described have been employed to have a more accurate calibration of the non-linear springs that models the response of the RBSs. The calibration was carried out through the tool Multical which allowed for finding the best combination of parameters matching the experimental response. Moreover, in the tool, the user can choose the set of parameters to be calibrated, e.g., for the Bouc-Wen model, the elastic stiffness, the α, β, γ parameters etc. It was chosen to manually estimate the elastic stiffness and the hardening ratio whilst the non-linear Bouc-Wen constants were found using Multical. The stiffness parameters for the calibration were based on three reliable RBS hysteretic loops at the Near Collapse limit state. For each loop, an elastic and a hardening stiffness were evaluated for both the positive and the negative branches. The stiffness values were determined considering the linear part of the cycles, as depicted in Figure 4.16. The model was calibrated employing the mean values of elastic and hardening stiffness, reported in Table 4.1. The additional parameters of the Bouc-Wen model were calibrated on RBS hysteretic loops at near collapse and are reported in Table 4.2.
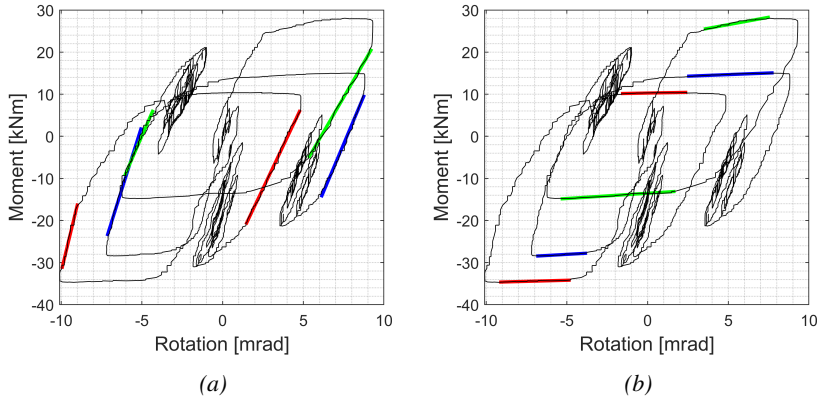
Figure 4.16: DRLF-MS: (a) elastic and (b) hardening stiffness calibration on near collapse cycles.

Parameter	Value
Elastic Stiffness K_{el} $[^{Nm}/_{rad}]$	$1.01 \cdot 10^7$
Hardening Stiffness K_{ha} $[^{Nm}/_{rad}]$	$2.48 \cdot 10^5$
Hardening ratio $[\%]$	2.45

Table 4.1: DRLF-MS: Estimated stiffness parameters.

Parameter	IPE160	Parameter	IPE160
$\alpha\ [\%]$	2.45	$A_0(-)$	1
$k_0\ [N/rad]$	$1.01 \cdot 10^7$	$\delta A(-)$	0
$\eta(-)$	5	$\delta\nu(-)$	0
$\gamma(-)$	$7.07 \cdot 10^{12}$	$\delta\eta(-)$	0
$\beta(-)$	$7.07 \cdot 10^{12}$		

Table 4.2: DRLF-MS: Calibrated Bouc-Wen parameters.

Following the calibration, time-history analyses on the updated model
were carried out using the same set of ground motion records employed
for the hybrid simulation. The match between the results of the finite el-
ement model and the experimental test rose, achieving good agreement.
Indeed, as can be observed in Tables 4.3 and 4.4 in which the errors in
terms of global seismic response are listed, the inaccuracy did not ex-
ceed 20% in terms of NRMSE and 25% for the difference on the peak
response. The exception lies in the MOOG3 values: the lower accuracy,
in this specific case, may be attributed to the position of the actuator.
Since it was located at the interface node, it was more affected by errors
due to the substructuring. Moreover, it can be noticed that the discrep-
ancies decrease as the earthquake intensity increases (DL, SD and NC),
mainly because errors are calculated with respect to the experimental val-
ues. Thus, the same experimental error in absolute terms (kN or mm)
implies lower errors when higher forces or displacements are measured.
The model parameters were updated to obtain a high-fidelity model. In
addition, the calibrated numerical models of the monotonic and hys-
teretic behaviour of the reduced sections were employed in the following
experimental campaign, which took place at the laboratory of the Uni-
versity of Trento and concerned a moment-resisting frame equipped with
DRLF systems coupled with high-strength steel beams.

		DL NRMSE [%]	SD NRMSE [%]	NC NRMSE [%]
DISP	Top Floor	18.21	11.00	4.15
	MOOG1	14.66	11.29	11.97
	MOOG3	15.46	11.96	12.29
SHEAR	Base	16.42	12.42	6.74
	MOOG1	18.51	12.73	6.73
	MOOG3	21.94	21.04	19.97

Table 4.3: DRLF-MS: NRMSE between the test and the calibrated model results.

			DL			SD			NC		
			Test	Simul.	Error	Test	Simul.	Error	Test	Simul.	Error
DISPLACEMENT [mm]	Top Floor	Max	68.64	65.92	4%	162.85	162	1%	304.49	282.81	7%
		Min	-32.06	-40.23	25%	-200.14	-169.48	15%	-412.75	-390.88	5%
	MOOG1	Max	5.77	5.44	6%	14.77	11.02	25%	31.61	29.74	6%
		Min	-6.16	-5.46	11%	-19.79	-19.07	4%	-20.7	-22.96	11%
	MOOG3	Max	11.63	9.11	22%	27.79	19.05	31%	61.55	57.76	6%
		Min	-10.09	-9.42	7%	-40.47	-36.12	11%	-41.46	-44.41	7%
SHEAR [kN]	Base	Max	164.61	205.68	25%	436.57	365.68	16%	587.39	519.28	12%
		Min	-183.21	-224.64	23%	-411.36	-414.22	1%	-496.95	-443.86	11%
	MOOG1	Max	141.97	152.83	8%	374.11	341.74	9%	507.14	492.11	3%
		Min	-129.33	-190.05	47%	-387.64	-385.76	0%	-459.64	-441.94	4%
	MOOG3	Max	86.75	189.89	119%	167.25	384.82	130%	177.44	442.91	150%
		Min	-105.11	-153.04	46%	-214.94	-341.06	59%	-248.08	-492.95	99%

Table 4.4: DRLF-MS: Errors between the peak response of test and the calibrated model

95

4.3 DRFL - HSS Frame

In this Section, the outcomes of the tests conducted on DRLF HSS frame are thoroughly presented. In particular, the test setup is first described, and subsequently, the results of the tests at the three different limit states are illustrated.

4.3.1 Hybrid test configuration

As previously described, the test set-up involved the employment of two actuators, namely MOOG1 and MOOG3, located respectively at the floor level and in the mid-height of the first floor, Figure 4.17.
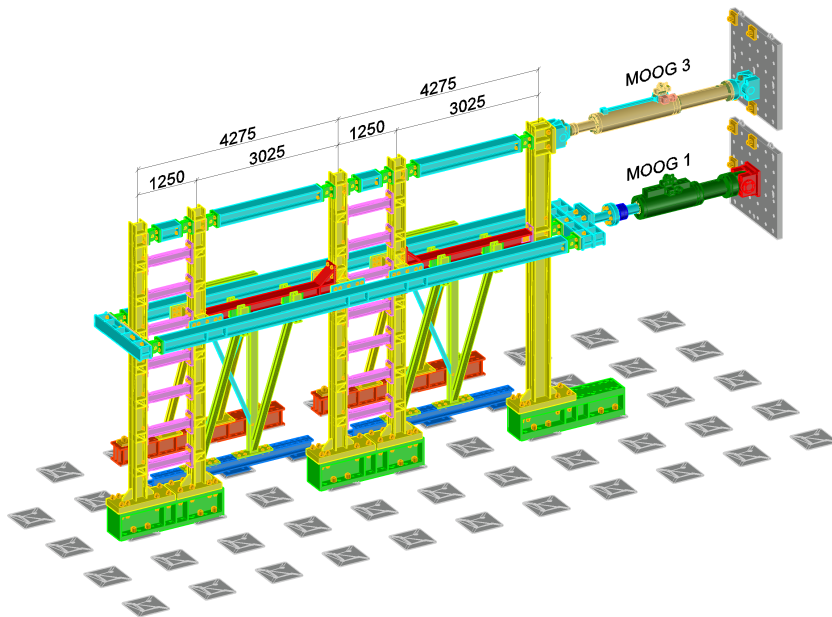
Figure 4.17: DRLF-HSS: Experimental test set-up.

The instrumentation configuration is schematically illustrated in Figure 4.18. Two link beams were fully instrumented through displacement transducers, and strain gauges in an elastic region near the RBS. The former were installed to estimate the bending moment, while the latter were to compute the rotation of the reduced beam section. The instrumentation location is depicted in Figure 4.19: to get an accurate measurement of the out-of-plane deformation, on each beam link section strain gauges were located at the upper and the lower edge and the left and right edge of the section. The displacement transducers were installed at a distance

l_{bar} equal to 300 mm diagonally to amplify the displacements read by the instruments. Moreover, the HSS beams were instrumented by strain gauges and inclinometers placed respectively in an elastic region to estimate the bending moment at the beam-to-column joint and on the beams, three on the first one and two on the second, to estimate the rotations.

(a)

(b)
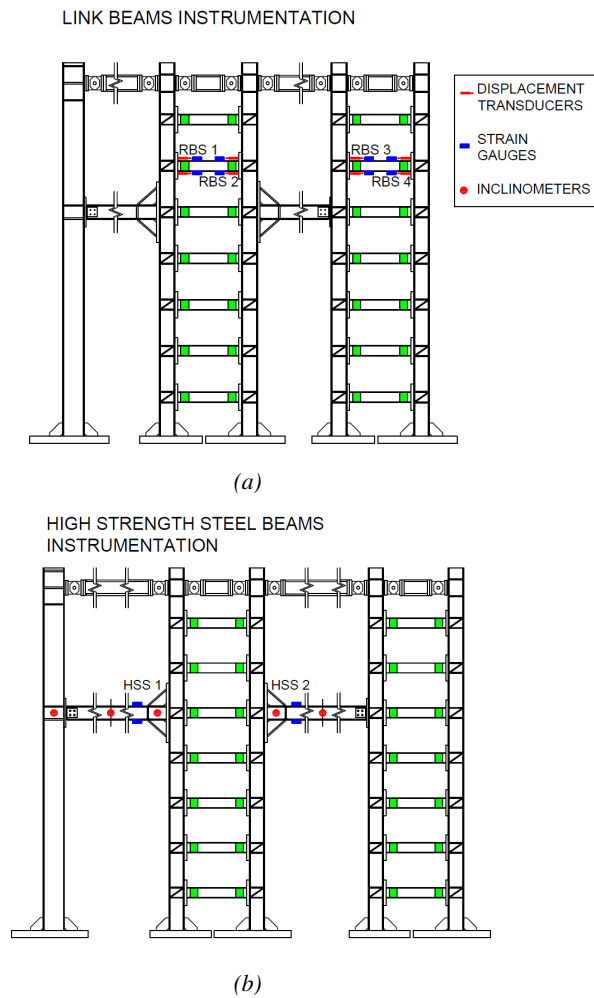
Figure 4.18: DRLF-HSS: Configuration of instrumentation system on (a) link beams and (b) HSS beam.
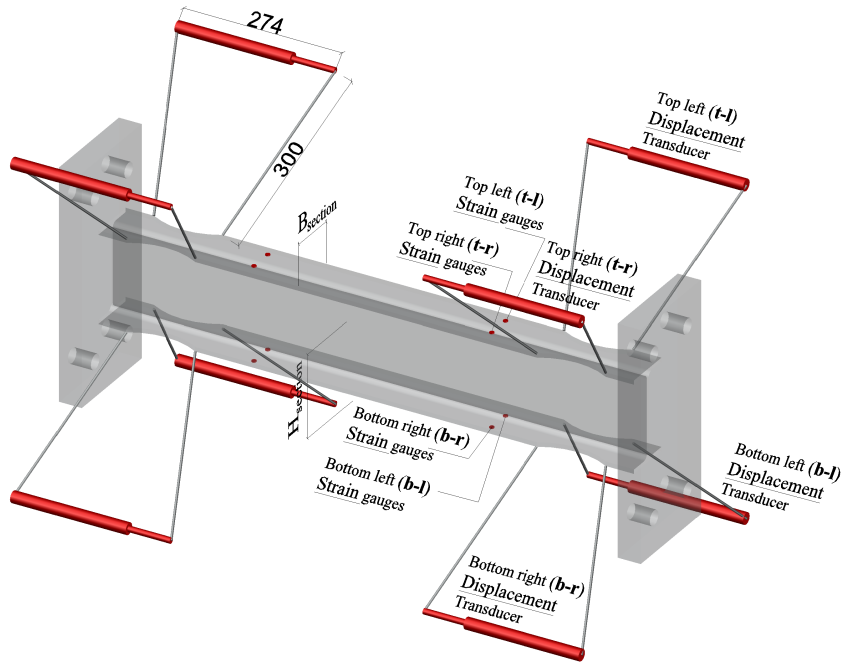
Figure 4.19: DRLF-HSS: Strain gauges location and displacement transducer location.

In this respect, both the in and out-of-plane curvatures were calculated by assuming plane sections are reported in Equation 4.4 where all the subscripts refer to Figure 4.19.

$$
\begin{aligned}
\chi_y &= \frac{\left(\varepsilon_{t,l} + \varepsilon_{t,r}\right)/2 - \left(\varepsilon_{b,l} + \varepsilon_{b,r}\right)/2}{H_{sec}} \\
\chi_z &= \frac{\left(\varepsilon_{t,l} + \varepsilon_{b,l}\right)/2 - \left(\varepsilon_{t,r} + \varepsilon_{b,r}\right)/2}{B_{sec}}
\end{aligned}
\tag{4.4}
$$

An estimation of the bending moment on each instrumented section, located in the elastic range, could be then obtained by means of the following formulae, in which $I_{*,beam}$ are the modulus of inertia of the gross section and E_s is Young's steel modulus.

$$
\begin{aligned}
M_y &= E_s \, I_{y,beam} \, \chi_y \\
M_z &= E_s \, I_{z,beam} \, \chi_z
\end{aligned}
\tag{4.5}
$$

The bending moment along both the strong and the weak axis at the RBS could be derived by linear interpolation from the bending moments

obtained in the elastic range of the beam. The rotation of the RBSs was
calculated as follows:

$$
\begin{aligned}
\varphi_y &= \frac{\left(\Delta_{t,l} + \Delta_{t,r}\right)/2 - \left(\Delta_{b,l} + \Delta_{b,r}\right)/2}{H_{sec} + 2\left(l_{bar}\sqrt{2}/2\right)} \\
\varphi_z &= \frac{\left(\Delta_{t,l} + \Delta_{b,l}\right)/2 - \left(\Delta_{t,r} + \Delta_{b,r}\right)/2}{B_{sec} + 2\left(l_{bar}\sqrt{2}/2\right)}
\end{aligned}
\tag{4.6}
$$

4.3.2 Description of the results

Damage limitation limit state

At DL limit state, the elastic response of the structures was verified. The
bending moment time-histories of the three RBSs depicted in Figure 4.20
highlight the elastic behaviour: the maximum value attained was lower
than the elastic resisting moment. The latter corresponds to the onset
of yielding at the extreme fibre from an elastic stress distribution, that
was estimated equal to 19.34 kNm, based on the reduced cross-section
properties. Unfortunately, one of the RBS n°2 strain gauges got damaged
during the erection process of the frame and could not be replaced, so
that no accurate information can be obtained for this section.
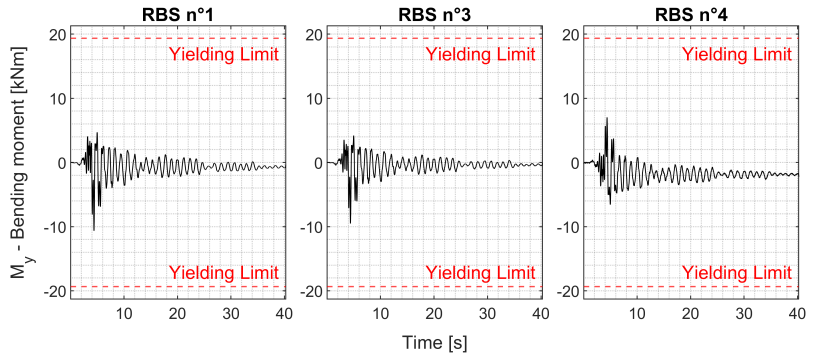
Figure 4.20: DRLF-HSS: DL - Bending moment of RBSs.

The elastic behaviour is also confirmed by looking at the maximum
displacement, depicted in Figure 4.21, achieved among the floors, which
corresponds to a peak interstorey drift ratio of 0.35%, as reported in Ta-
ble 4.5. This value is significantly lower than the conventional limit for
DL limit state of 0.7%, as suggested by FEMA356 [94]. Moreover, the
table highlights a residual maximum interstorey drift of 0.01%. In Fig-
ure 4.22, the time-histories on the displacement and the force at the ac-
tuators level are reported.

Figure 4.21: DRLF-HSS: DL - Maximum displacement of the six floors.

Table 4.5: DRLF-HSS: DL – Peak interstorey drift ratio [%].
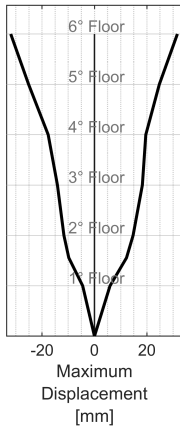
Floor	Maximum	Minimum	Residual
1st	0.17	-0.13	0.00
Sub. point	0.35	-0.28	0.01
2nd	0.18	-0.13	0.01
3rd	0.32	-0.34	0.00
4th	0.19	-0.25	0.00
5th	0.22	-0.21	0.00
6th	0.22	-0.21	0.00
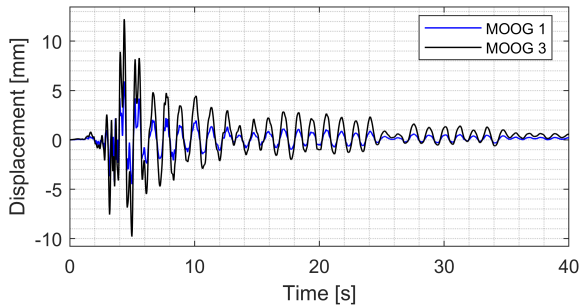
(a)
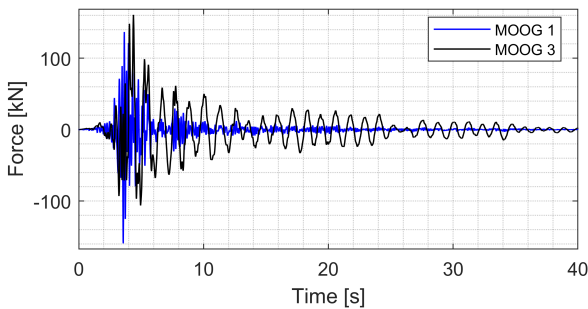
(b)

Figure 4.22: DRLF-HSS: DL - Time histories of the (a) displacements and (b) forces of the two actuators.

Significant Damage limit state

For the Significant Damage limit state, the structure suffered plastic deformation localized on the RBSs of the beam links. The inelastic behaviour is underlined in Figure 4.23, which shows the bending moment history of the RBSs. Indeed, during the test, the bending moment in the devices exceeded the plastic bending moment. Figure 4.24 shows the hysteretic cycles of the RBSs, confirming the yielding of the reduced section of the beam links.
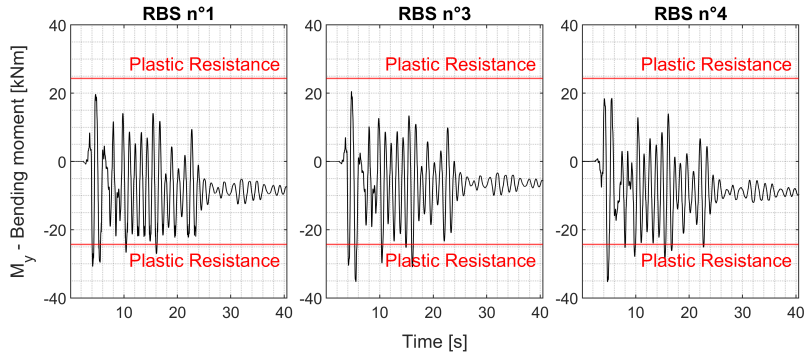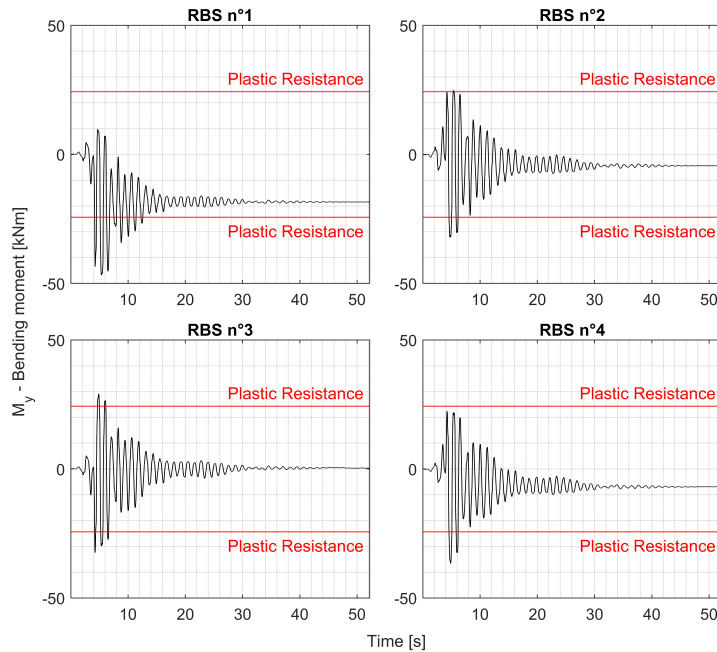

Figure 4.23: DRLF-HSS: SD - Strong axis bending moment of RBSs.
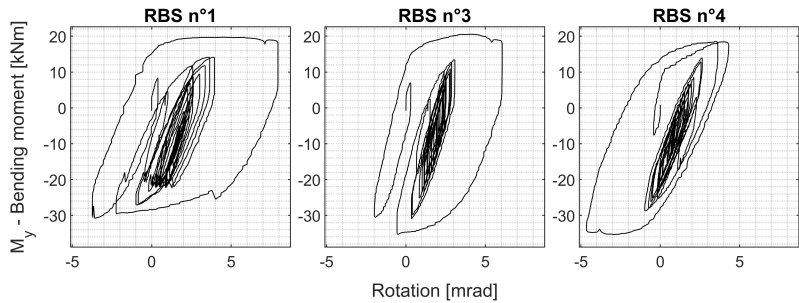
*Figure 4.24: DRLF-HSS: SD - Moment-rotation diagrams of RBSs.*

In Figure 4.25, the displacement and force histories of the actuators are reported, and the maximum values attained during the test are reported in Table 4.7.

By computing the PIDR, it has been found that the maximum value attained during the test for the physical substructure was 1.50% while for the numerical was 1.95%, as reported in Table 4.6. Moreover, the figure highlights a residual interstorey drift of 0.01%, which ensures the components' replaceability after an earthquake of medium intensity.

(a)

(b)
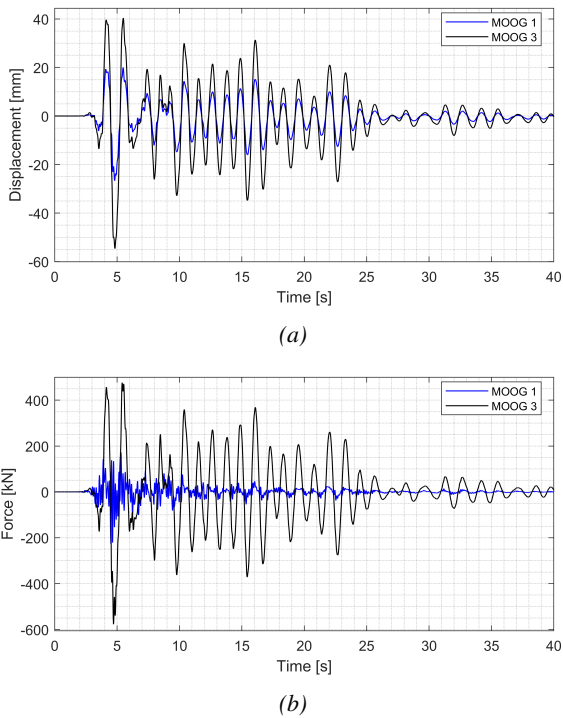
Figure 4.25: DRLF-HSS: SD - Time histories of the (a) displacements and (b) forces of the two actuators.

Floor	Maximum	Minimum	Residual
1st	0.57	-0.76	0.01
Sub. point	1.09	-1.50	0.01
2nd	0.92	-1.06	0.01
3rd	1.68	-1.95	0.01
4th	0.77	-0.84	0.01
5th	0.68	-0.73	0.01
6th	0.68	-0.73	0.01

Table 4.6: DRLF-HSS: SD - Peak interstorey drift ratio [%].

Near Collapse limit state

At the Near Collapse limit state, the specimen exhibited a strong non-linear behaviour characterized by the plasticization of the RBSs, as depicted in Figures 4.26 and 4.27.

		MOOG 1	MOOG 3
Displacement	Push	19.98	40.39
[mm]	Pull	-26.68	-54.64
Force	Push	172.68	476.38
[kN]	Pull	-226.18	-577.3

Table 4.7: DRLF-HSS: SD - Maximum displacements and forces attained during the test by the actuators.

In the Figures, the bending moment time-history and the moment-rotation diagrams of RBSs are reported, and the exceedance of the plastic resisting moment can be highlighted. The RBSs showed a large dissipative hysteretic behaviour, with a maximum rotation greater than 10 mrad. Moreover, the residual plastic deformation of the sections can be underlined in both figures. Nevertheless, besides the RBSs plasticization, the structure remained in the elastic field, as proven in Figure 4.28 where the time histories of the bending moment on the HSS fixed section are reported. As depicted, the maximum bending moment attained during the tests is significantly smaller than the plastic bending moment.

Figure 4.26: DRLF-HSS: NC - Strong axis bending moment of RBSs.
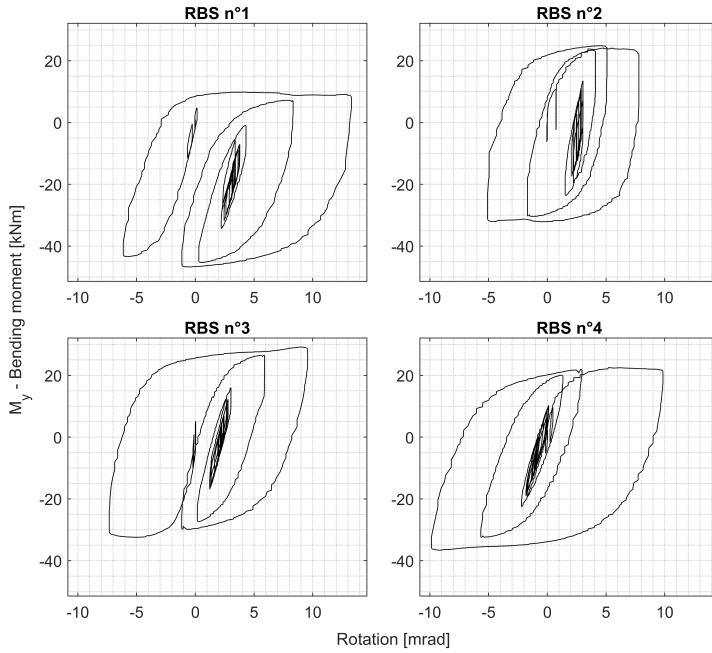
Figure 4.27: DRLF-HSS: NC - Moment-rotation diagrams of RBSs.
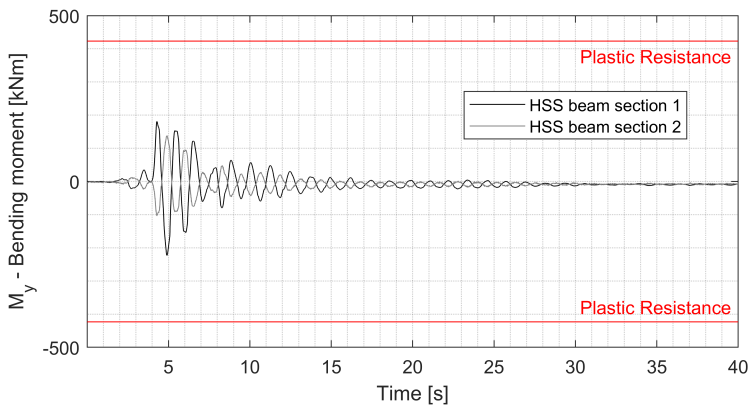
Figure 4.28: DRLF-HSS: NC - Bending moments at HSS fixed joints.

The plastic behaviour is also confirmed by looking at the residual PIDR reported in Table 4.8, which demonstrated the residual plastic deformation of the structure.
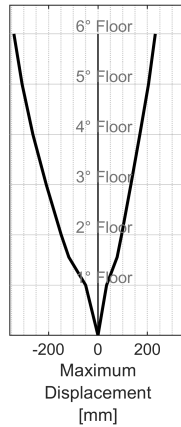
Figure 4.29: DRLF-HSS: NC - Maximum displacement of the six floors.

Floor	Maximum	Minimum	Residual
1st	0.99	-1.42	0.03
Sub. point	2.45	-3.50	0.03
2nd	1.48	-2.32	0.03
3rd	2.73	-4.14	0.03
4th	1.20	-1.68	0.03
5th	1.06	-1.37	0.03
6th	1.06	-1.37	0.03

Table 4.8: DRLF-HSS: NC - Peak interstorey drift ratio [%].

In Figure 4.30, the top floor displacement versus the base shear is reported for each test. As it can be noticed, the structure remained in the elastic field concerning the DL limit state, whilst slight plasticization can be appreciated from Figure 4.30b for SD limit state. Finally, Figure 4.30c remarks that the structure fully entered in the plastic region for NC limit state.

4.3.3   Comparison with the OpenSees reference model

In the tests performed on DRLF-HSS, the plastic hinges of the reduced beam sections were modelled by implementing the Bouc-Wen parameters calibrated based on the results of the previous tests on DRLF-MS. Due to this, a good agreement between the hybrid tests results and the OpenSees reference model was found, as demonstrated by the errors reported in Table 4.9 in terms of normalized root mean square for each limit state. It can be highlighted that all the errors are lower than 15%.

As for DRLF-MS, the RBSs suffered an out-of-plane deformation which caused a slightly different cyclic behaviour compared with the theoretical monotonic Figures 4.31 and 4.32.

(a)

(b)

(c)
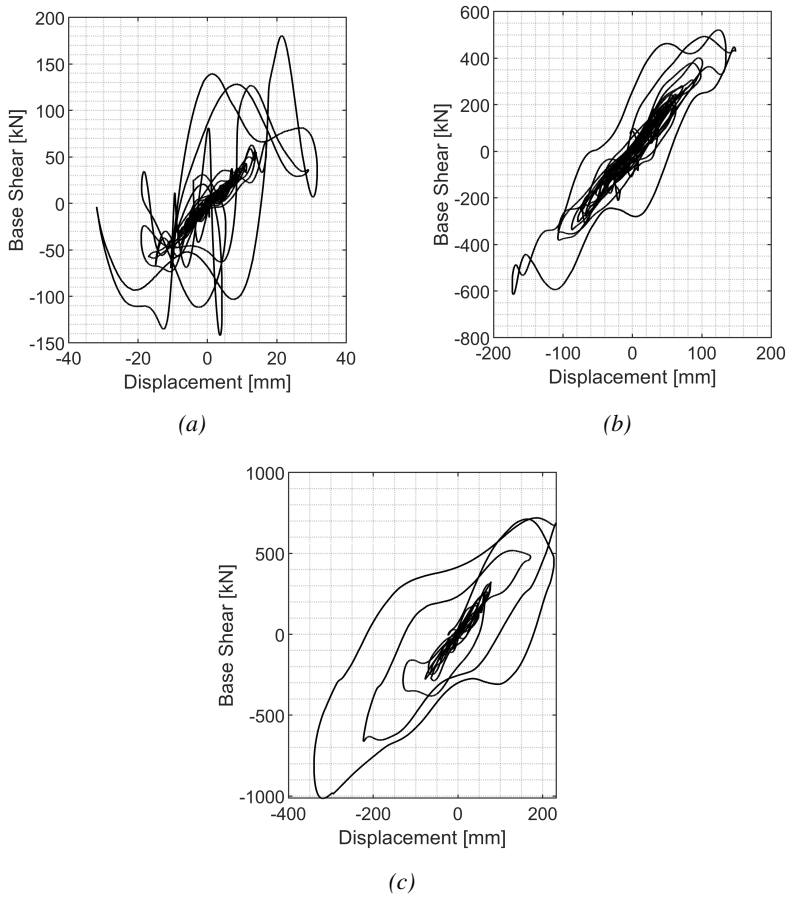
Figure 4.30: DRLF-HSS: Top Floor displacement vs Base Shear graphs at: (a) DL, (b) SD and (c) NC limit states.

	DL	SD	NC
Top floor disp	5.5	6.4	4.8
Base shear	7.7	5.5	5.4
MOOG1 disp	9.8	8.9	6.3
MOOG1 force	4.0	5.4	3.8
MOOG3 disp	11	10.3	5.8
MOOG3 force	7.7	5.5	5.1

Table 4.9: NRMSE between OpenSees reference model and the hybrid tests global quantities [%].
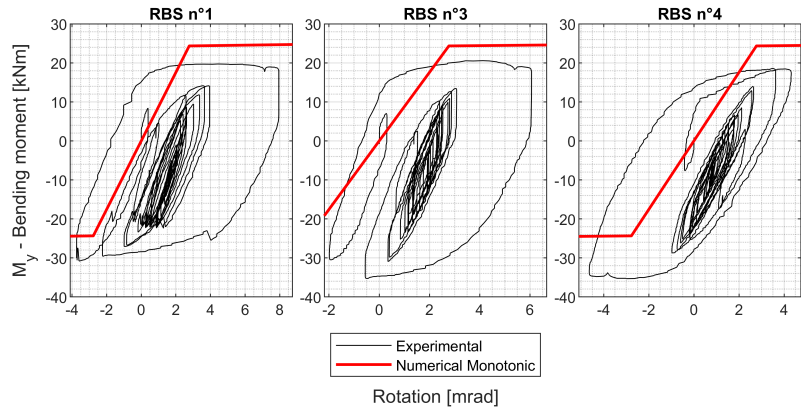
Figure 4.31: DRLF-HSS: SD - Moment-rotation diagram comparison between hybrid test and theoretical monotonic behaviour.
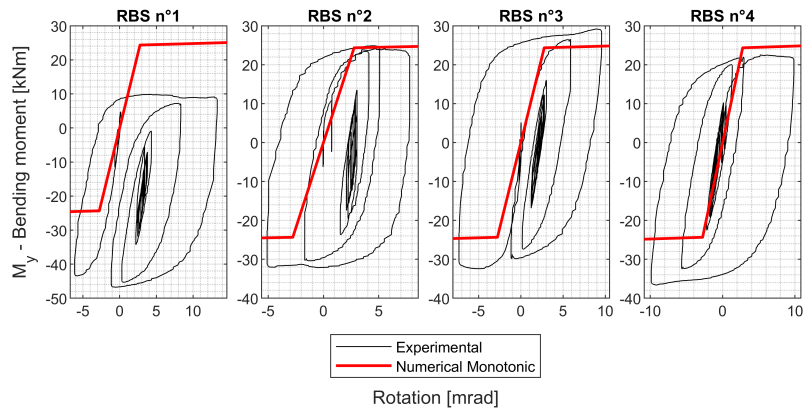
Figure 4.32: DRLF-HSS: NC - Moment-rotation diagram comparison between hybrid test and theoretical monotonic behaviour.

4.4 DRBrC Frame

4.4.1 Hybrid test configuration

As previously mentioned, the experimental set-up conceived to perform hybrid simulation on the DRBrC frame entailed the use of one actuator located at the first-floor level since the behaviour of the DRBrC depends on the axial forces in the braces, see Figure 4.33. Regarding the instrumentation, displacements and strains of the DRBrCs were measured by means, respectively, of displacement transducers on the lateral sides of each DRBrC, and strain gauges. From the latter, the axial force acting on the devices was derived, enabling to plot force-displacement diagrams and verifying the local behaviour. Moreover, a couple of strain gauges were also installed on the horizontal beam to compute the axial force. Since the column bases were an unreplaceable part of the structure and could not be regarded as perfect hinges, strain gauges were applied at the columns bases to predict any possible bending actions.
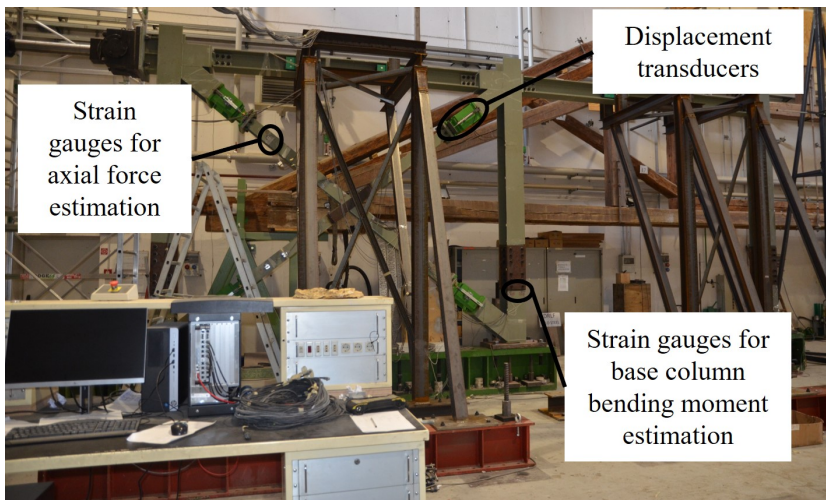
Figure 4.33: DRBrC: Experimental test set-up.

4.4.2 Description of the main results

This paragraph briefly describes the results on the frame equipped with both mild steel and HSS plates of DRBrC. Thanks to the tests carried out, it was possible to characterise the seismic behaviour of the structures. The tests were conducted at different seismic intensity levels, as described in Section 3.4, enabling the characterization of both the struc-

ture's elastic and the inelastic field. Moreover, the possibility of repairing the frame by replacing the dissipative components was demonstrated. The main outcomes of the overall test campaign are listed here:

- preliminary tests detected the presence of an initial branch with zero stiffness due to a non-negligible clearance, about 1 mm, between the pin and the eyebar plate hole. This clearance was included in the numerical part of the frame for consistency between PS and NS;

- regarding the structural behaviour at DL limit state, the structure elastically reacted to the stress imposed. In particular, the irreplaceable part remained in the elastic field while DRBrC exhibited small hysteretic dissipation due to the local bearing of the pin, see Figure 4.34;

- at both SD and NC limit state, the DRBrC components highlighted a favourable hysteretic behaviour with large loops owing to the pin inelastic behaviour. The non-dissipative parts of the frame, i.e. braces, columns and beams, did not experience inelastic behaviour, as shown in Figure 4.35 for the column base, which proves the good performance of the DRBrC components in protecting the irreplaceable parts of the frame.

- Finally, small residual displacements were observed at each limit state that enhanced the self-centring capabilities and repairability. Indeed, the connections could be replaced after the SD hybrid test without particular effort.

By comparing the test results on DRBrC with mild steel and HSS plates, no significant improvements or differences were found in the seismic performance, as shown in Figure 4.36. Indeed, the maximum displacements were not large enough to show the beneficial effects of a higher steel grade.
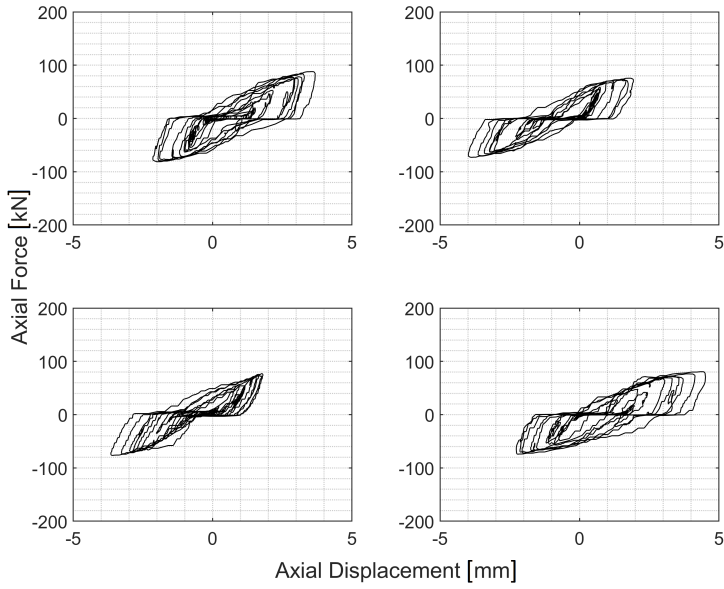
Figure 4.34: DRBrC: DL - Experimental axial force-displacement diagrams.
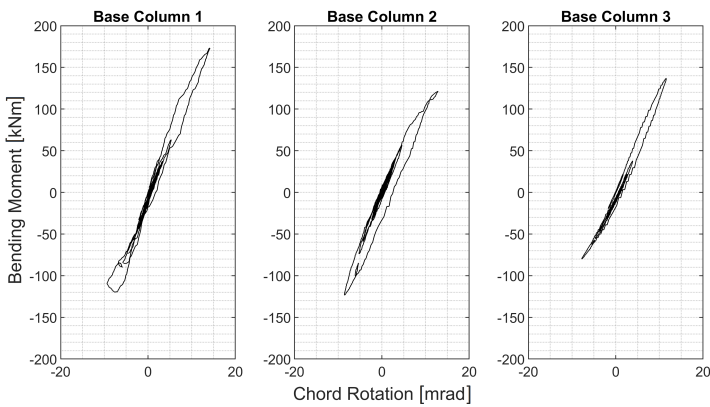
Figure 4.35: DRBrC: NC - Base columns bending moment.
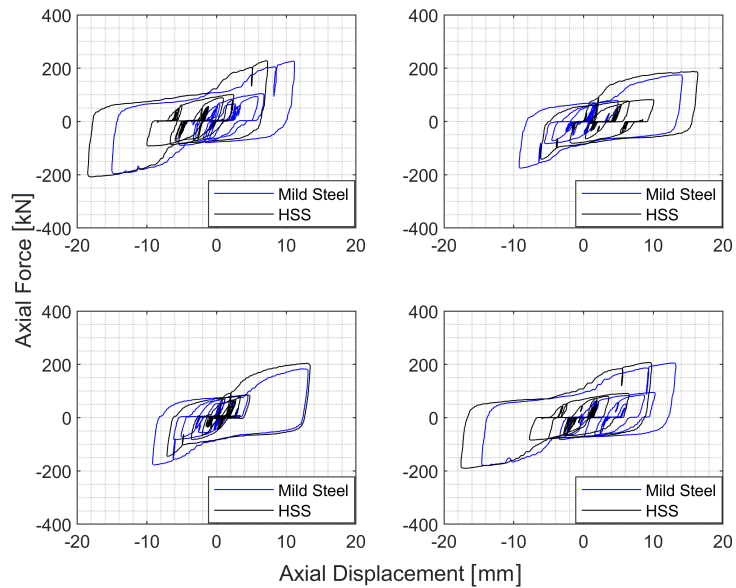
Figure 4.36: DRBrC: NC - MS vs HSS force-displacement diagrams.

4.5 DRBeS Frame

4.5.1 Hybrid test configuration

The experimental set-up conceived for DRBeS frame is depicted in Figure 4.37. As shown, the physical part consists of the first floor and a half of the structure. The point of inflexion, i.e. where the column bending moment is zero, at least for the gravity load, was localised in the columns to control only the horizontal degrees of freedom. As with the DRLF tests, two actuators were thus used. Regarding the instrumentation, Figure 4.38 illustrates the position of strain gauges in an elastic region near the device, and displacement transducers, for computing the component's rotation. Moreover, inclinometers were installed on the columns to measure the absolute rotations in two sections and estimate the bending moment at the base. This permitted to verify whether there had been any plasticisation during the tests. Finally, strain gauges were applied to the reinforcement bars to detect any possible yielding since they were part of the unreplaceable parts.

4.5.2 Description of the main results

The main results of the experimental campaign are reported here:

Figure 4.37: DRBeS: Experimental test set-up.
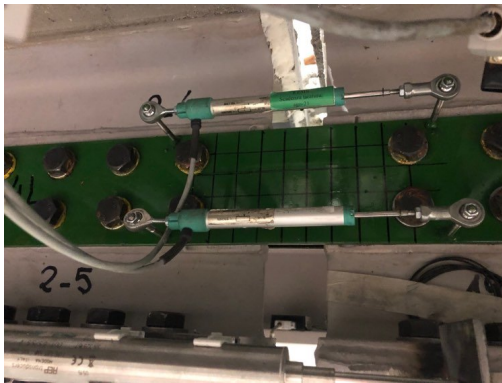
(a)
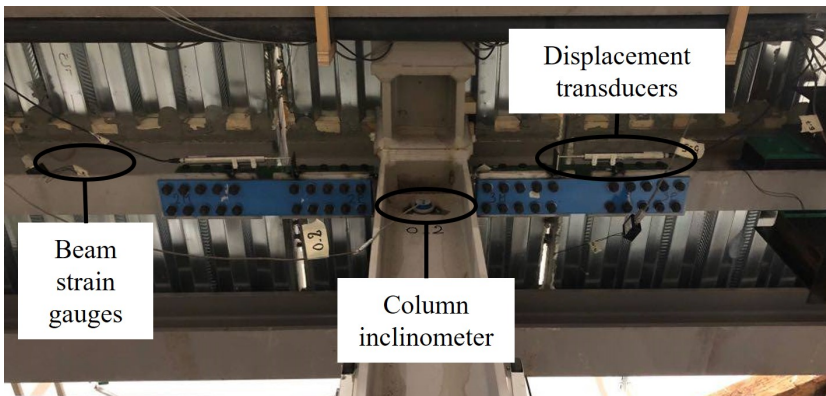
(b)

Figure 4.38: DRBeS: Some instrumentation photos.

- the structural behaviour at the DL limit state was fully elastic, as testified by Figure 4.39 where the moment-rotation diagram of devices is depicted.

- Figure 4.40 depicts the moment-rotation diagram of devices. As shown, DRBeS exhibited favourable inelastic behaviour without appreciable stiffness and strength loss. Moreover, large cycles entail a huge energy dissipation, which is a favourable outcome since the components were designed for this limit state. In addition, no damage in the non-replaceable parts of the frame.

- At the NC limit state, the base columns were slightly yielded, see Figure 4.41, as well as some cracking, occurred in the concrete slab. However, since the structure was designed for SD limit state, the overall behaviour was still satisfactory, with small residual inter-storey drifts and a favourable re-centring capability. Moreover, the DRBeS were highly damaged with evident plate buckling due to hogging bending moments.
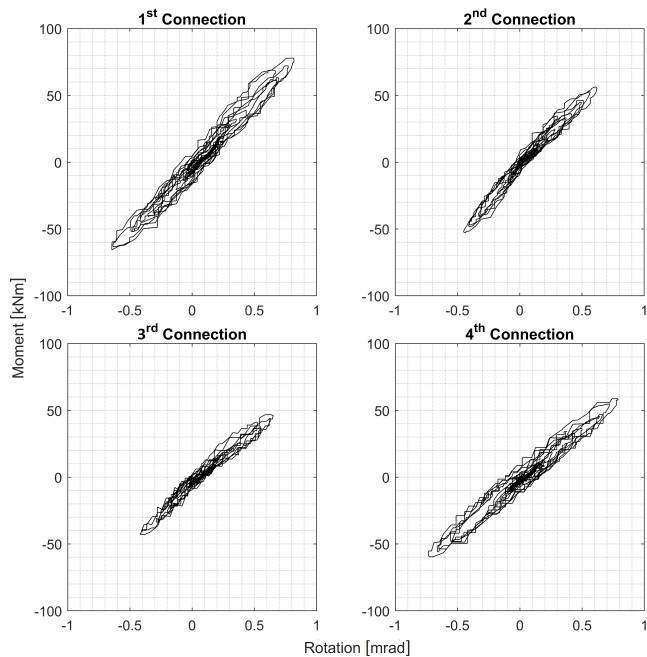
Figure 4.39: DRBeS: DL - Moment-rotation diagrams.
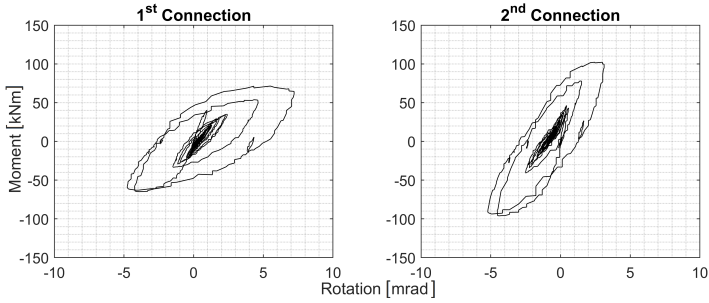
Figure 4.40: DRBeS: SD - Moment-rotation diagrams.
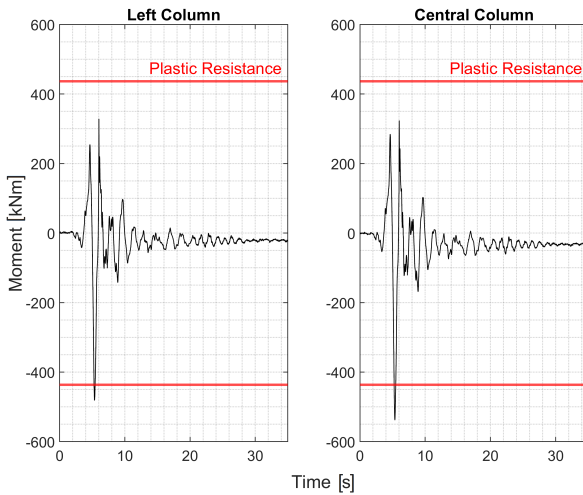
Figure 4.41: DRBeS: NC - Base columns bending moment.

4.6   Conclusions

The pseudodynamic hybrid tests performed on frames equipped with DISSIPABLE devices provided comprehensive and detailed information on their non-linear behaviour under natural earthquake accelerograms. It was possible to analyse the entire frames, including the five floors above, in the numerical substructure while keeping the physical substructure at full scale. In detail:

- the hybrid test results were compatible with the reference model for a frame with DRLF systems coupled with top bracing systems, even though the model was condensed on seven degrees of freedom. The RBSs remained in the elastic field at the DL limit state while they exhibited inelastic behaviour at the SD limit state. The RBSs experienced significant inelastic behaviour and out-of-plane rotation at the NC limit state. According to the design, except for the reduced beam sections, the remainder of the structure behaved elastically for all the limit states, i.e. DL, SD and NC. Furthermore, the replaceability of the link beams was checked between the SD and NC limit state tests by changing the beams and the substitution occurred without any particular problems.

- For the frame equipped with two parallel DRLF systems coupled with HSS beams, the behaviour of the structure was in agreement with what was observed for the mild-steel one in terms of dissipation of the devices at the different limit states. Differences were noted regarding the maximum forces reached by the actuators due to the greater structure stiffness given by fixed HSS beams. In addition, the out-of-plane displacement of the RBSs was less in this case.

- For tests on frames equipped with DRBrC component, the DL limit state test depicted a substantially elastic behaviour of the connections, with a small hysteretic dissipation due to local bearing between the pin and the internal side of the eyebar plate hole. The SD and NC limit state tests highlighted a remarkable hysteretic behaviour of the component due to the pin plastic behaviour both in bending and shear. The non-dissipative parts of the frame, i.e. braces, columns and beams, did not experience damage at any limit state test, which testifies an optimal performance of the DRBrC components in protecting the irreplaceable parts of the frame even for ground motion intensities (NC) larger than the design one (SD). This is a significant outcome in terms of repairability. More-

over, the connections could be replaced after the SD hybrid test
without particular effort. Finally, no significant improvements or
differences in the structural performance of HSS DRBrC compo-
nents concerning DRBrC mild steel components are found. The
differences in the axial force-displacement behaviour of mild and
HSS DRBrCs shown are mainly attributed to the different gap val-
ues, which is an aleatory parameter.

• For DRBeS at the DL limit state, both the non-dissipative elements
of the structures and the DISSIPABLE components behaved elas-
tically, whilst, at the SD limit state, energy dissipation in the plates
was detected. Dismounting the damaged plates and replacing the
new ones showed no particular difficulties. Since the structure
was designed for the SD limit state, some damage in the non-
dissipative parts was observed. In particular, cracking in the con-
crete slab and some yielding in the column bases were detected.
However, the overall behaviour was satisfactory with small resid-
ual inter-storey drifts, and a favourable re-centring capability was
highlighted.

Chapter 5

Optimization of the Partitioned G-α Algorithm

In this Chapter, the stability and accuracy analyses for the optimization of the PG-α algorithm are thoroughly presented. In order to study the real procedure implemented to perform DISSIPABLE tests, a Simulink [95] model (S-model) was developed. In particular, every laboratory source of error was accounted for and quantified by deriving it from the results of tests described in Chapter 4. Moreover, the algorithmic force correction was implemented in the same way as defined in the laboratory tests. Finally, the test results were compared to their respective OpenSees outcomes to validate the implemented procedure.

5.1 Algorithmic analysis implementing laboratory characteristics of real experimental tests

5.1.1 Proposed algorithmic correction

In order to perform the experimental tests, the laboratory test set-up depicted in Figure 5.1 was conceived. Lateral beams were placed at the floor level to reproduce the rigid diaphragm modelled in the finite element software. Those beams allowed for imposing the same displacement at each column avoiding the application of a significant axial force to the beams and the connections. In addition, beams with high axial stiffness were placed at the level of the higher actuator to impose the same displacement at the top of each column, as can be noticed from Figure 5.1.
The connection between the axially rigid beams and the structural elements was performed by means of hinges to avoid to increase the stiff-

ness of the original frame. The hinges were composed of three plates, through which a pin was inserted, as depicted in Figure 5.2. To decrease the gap between the pin and plates, the former was welded to the external plates, see Figure 5.2a. However, as illustrated in Figure 5.2b, the gap between the internal plates and the pin could not be avoided because of the physical impossibility of welding that area. Moreover, the connection between the axially rigid frame and the specimen was also constituted by hinges which underwent elastic deformations when loaded, as proven by preliminary tests conducted to measure the deformation of every element of the set-up.

To consider the source of error introduced by the issues mentioned above, auxiliary transducers were installed on the right side of the specimens to measure the displacements of the right column, see Figure 5.1. The Gefran external transducers were placed on an external fixed frame to obtain an absolute displacement measure.
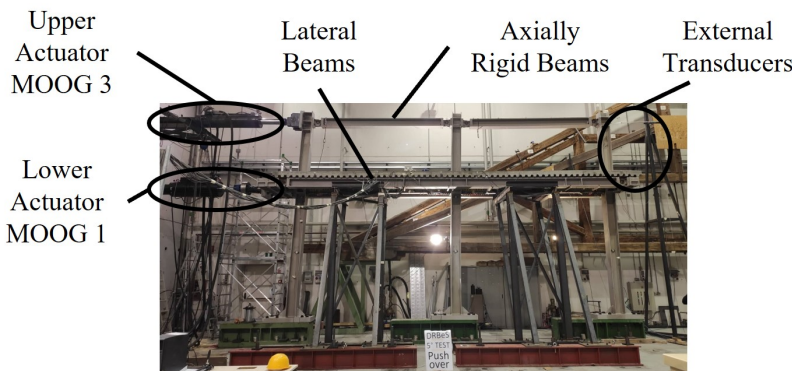
Figure 5.1: Laboratory test Set-Up.

Figure 5.2: Hinge detail: (a) pin welding and (b) gap between the internal plate and the pin.

In the numerical algorithm, the issues mentioned above were tackled by introducing an algorithmic correction on the forces read from the controller to account for the discrepancies between the displacement imposed by the actuators and the displacement on the opposite side of the frame. The implemented correction takes its starting point from what was proposed by Bursi and Shing [96] reported in Equation 5.1, where the second term of the sum is the algorithmic force correction. In the correction proposed, this term is proportional to the difference between the algorithmic displacement and the mean displacement of the three columns, see Equation 5.2.

$$\mathbf{R}_{n+1}^{P} = \mathbf{R}_{n+1}^{FBK} + \mathbf{K}_0 \left(\mathbf{Y}_{n+1}^{P} - \mathbf{Y}_{FBK}^{P} \right) \tag{5.1}$$

$$\mathbf{R}_{n+1}^{P} = \mathbf{R}_{n+1}^{FBK} + \mathbf{K}_0 \left(\mathbf{Y}_{n+1}^{P} - \frac{\left(\mathbf{Y}_{FBK}^{P} + \mathbf{Y}_{GEF}^{P} \right)}{2} \right) \tag{5.2}$$

In the previous formulae, $\mathbf{R}_{n+1}^{P}$ is the algorithmic force acting on the physical subdomain, $\mathbf{R}_{n+1}^{FBK}$ is the actuator force feedback, $\mathbf{K}_0$ is the numerically estimated stiffness matrix, $\mathbf{Y}_{n+1}^{P}$ is the displacement computed by the algorithm, $\mathbf{Y}_{FBK}^{P}$ and $\mathbf{Y}_{GEF}^{P}$ are respectively the displacement feedbacks from the actuator and the auxiliary Gefran transducers.
In order to study the reliability of the algorithmic correction adopted, stability and accuracy were investigated for the original PG-α method, implementing the algorithmic correction in Equation 5.2 and the parameter η previously defined in Equation 2.21.

5.1.2 Numerical model of the experimental set-up

To verify the stability and accuracy of the PG-α algorithm implemented to run the DISSIPABLE laboratory tests, a Simulink model (S-model) was developed, as depicted in Figure 5.3. In the S-model, the control system's effect and the errors introduced by the instrumentation readings were considered. In particular, the actuator was modelled by means of the z-transform transfer function, assimilating it to a single degree of freedom dynamic system. Laboratory errors were induced by considering, on the one hand, white noise added to each experimental measurement to simulate the effect of instrumentation. In addition, two further sources of error were accounted for in the external transducer readings, i.e. the delay and reduction with respect to the displacement imposed by the actuator. The force feedback correction illustrated in Equation 5.2 was implemented to consider the specimen's deformability and the impact of the gaps. The restoring force feedback was computed as indicated

119

in Equation 5.3.

$$\mathbf{R}_{n+1}^{FBK} = \mathbf{K} \cdot \frac{\mathbf{Y}_{FBK}^{P} + \mathbf{Y}_{GEF}^{P}}{2} \qquad (5.3)$$

From Equations 5.2 and 5.3, it can be deduced that when the numerically estimated stiffness used to compute the algorithmic correction K_0 is equal to the actual stiffness K, the algorithmic force is equal to the one of the original PG-α algorithm Equation 5.4.

$$\mathbf{R}_{n+1}^{P} = \mathbf{K} \cdot \mathbf{Y}_{n+1}^{P} \qquad (5.4)$$

5.1.3 Derivation of the source of error based on experimental tests

The data collected from tests on the five specimens at three limit states were analysed to thoroughly investigate the influence of adopting the proposed algorithmic correction. For three out of five tests, two actuators and two external transducers were employed, resulting in 24 signals to be analysed for each measure, i.e., actuators force feedback, displacement command, actuator displacement transducers and external transducers. To accurately replicate the laboratory tests, the instrumentation noise was modelled by means of white noise, whose variance was determined by applying a bandpass filter to isolate the noise with respect to the signal for each type of measure, as reported for one signal in Figure 5.4. In Figure 5.5, the variance values of all the signals of the same type are reported, while in Table 5.1, the mean noise variances are listed. These quantities are consistent with the precision of the instrumentation.

	σ^2	$3\,\sigma$	Datasheet accuracy
Displacement Feedback (Temposonic Transducer)	$7.97 \cdot 10^{-10}$ $[m^2]$	$8.4 \cdot 10^{-5}$ $[m]$	$2 \cdot 10^{-6}$ $[m]$
External Transducer (Gefran Transducers)	$1.27 \cdot 10^{-9}$ $[m^2]$	$1.07 \cdot 10^{-4}$ $[m]$	$5 \cdot 10^{-4}$ $[m]$
Force Feedback	$1.66 \cdot 10^{6}$ $[N^2]$	$3.87 \cdot 10^{3}$ $[N]$	$3 \cdot 10^{2}$ $[N]$

Table 5.1: Mean variance summary

Additionally to the white noise, the delay between the displacement transducer measures and the algorithmic command was introduced in

Figure 5.3: Simulink Model.
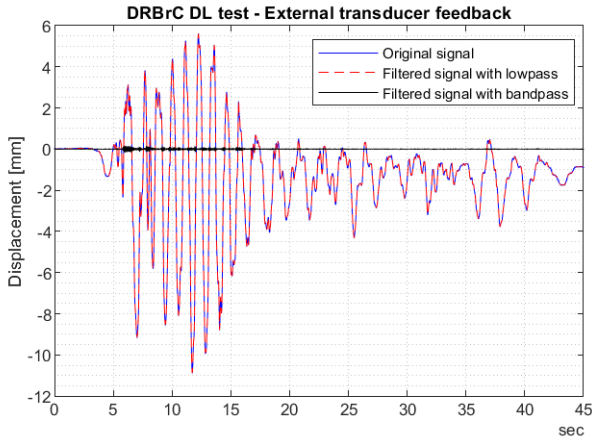
Figure 5.4: Signal filtering.
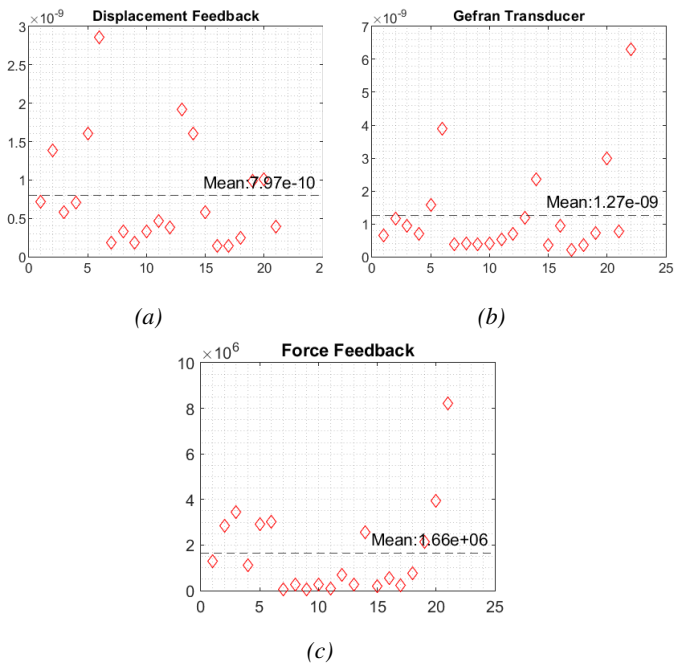
Figure 5.5: Noise variance of instrumentation measurements.

the S-model. Moreover, the reduction between the actuator command
and the Gefran measurement was introduced. Both phenomena can be
detected by Figure 5.6. Accounting for these sources of error allowed
the laboratory framework to be adequately represented and to model the
results. The delay was computed for all the signals, and a mean value of
2 algorithmic steps was identified. The reduction factor was computed
considering each signal's first five positive and five negative peaks, ob-
taining a mean value of 0.82.
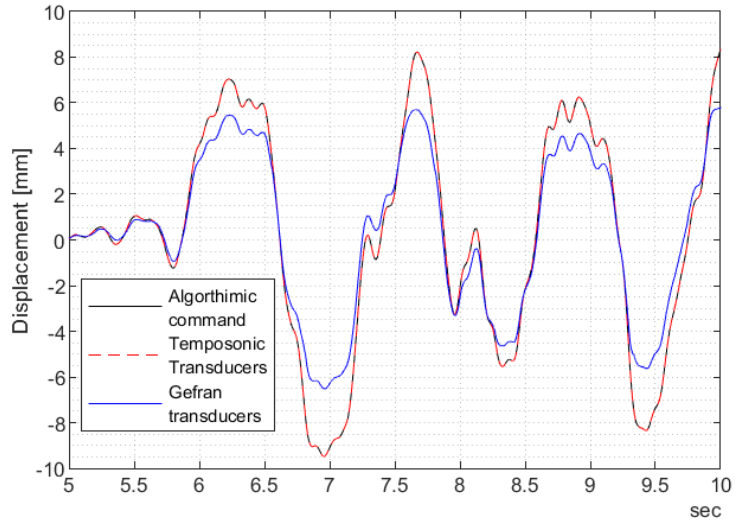
Figure 5.6: DRBrC DL test.

5.2   Algorithm analysis results

Given the previously described model, the stability and the accuracy of
the PG-α algorithm, along with the algorithmic correction and measure-
ment errors, have been investigated for a single degree of freedom case
study. The mass and stiffness values were computed by dynamically con-
densing, see Equation 5.5, the physical and the numerical mass matrix, as
well as the total mass and stiffness on the first period of the DRLF-HSS
test.

$$\mathbf{T_{cond}} = \Phi_1^T \cdot \mathbf{T} \cdot \Phi_1 \qquad (5.5)$$

where T is a generic matrix an Φ_1 the first mode shape vector.
Moreover, the factor b_1 was computed as defined in Equation 2.23c and

the numerical and physical stiffness were derived starting from the total one by inverting Equation 2.23d. In particular, according to the preliminary results on the SDoF reported in Section 2.2.2, a unique value of b_1 was considered since it is irrelevant to the stability and accuracy of the algorithm.

Parameters	Value
m_{tot}	$8.42 \cdot 10^4 kg$
m^N	$6.62 \cdot 10^4 kg$
m^P	$1.80 \cdot 10^4 kg$
k_{tot}	$2.13 \cdot 10^6 N/m$
k^N	$4.55 \cdot 10^5 N/m$
k^P	$1.68 \cdot 10^6 N/m$
b_1	0.27

Table 5.2: S-Model: Model parameters

As done for the previous case studies, four values of infinity spectral radius ρ_∞ were investigated for three values of η, i.e. 0.5, 0.75 and 1.00. For each combination of ρ_∞ and η, the amplification matrix **A** was computed by imposing a unitary value alternatively for all the problem variables, e.g., numerical and physical displacement, numerical and physical velocity, etc. It can be noticed from the results depicted in Figure 5.7 that the algorithm is always stable regardless of the value of η and ρ_∞ since the absolute value of the eigenvalues of the amplification matrix, λ, are always lower than the stability threshold. This result agrees with what is reported in Section 2.2.2. Hence, with the algorithmic correction, the order of accuracy is in general lowered to 1, but the algorithm is still always stable.

Regarding the accuracy analysis, whose results are reported in Figure 5.8 in terms of GTE on the displacement, it can be highlighted that by introducing the laboratory errors, the order of accuracy is one, even in the case of η equal to one, differently from what is reported in Section 2.2.2. Moreover, for values of the ratio η lower than the unit, the global truncation error has an asymptotic trend for small values of Δt, indicating that reducind the time step does not enhance the algorithm's accuracy.
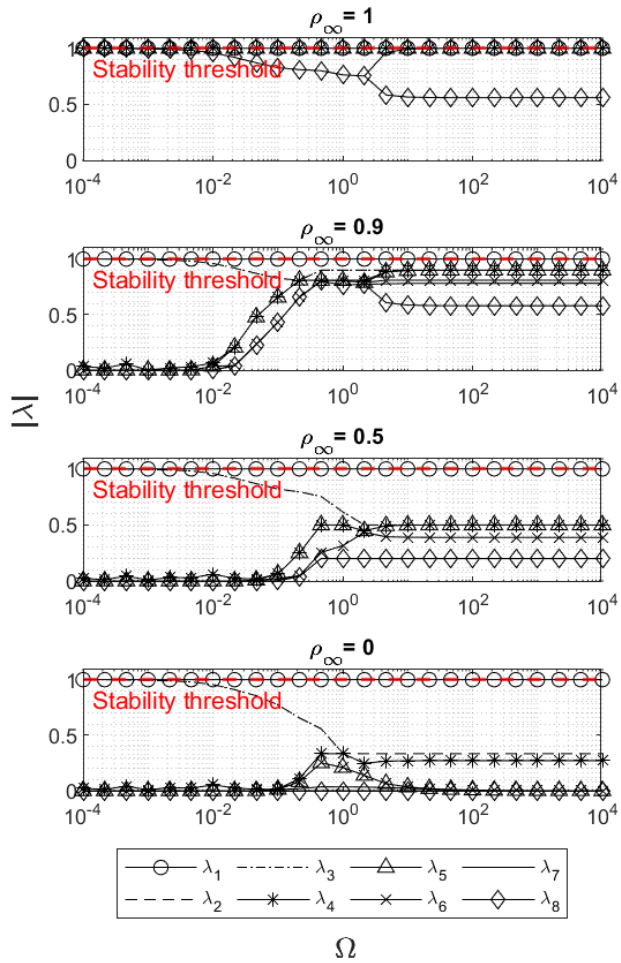
(a)
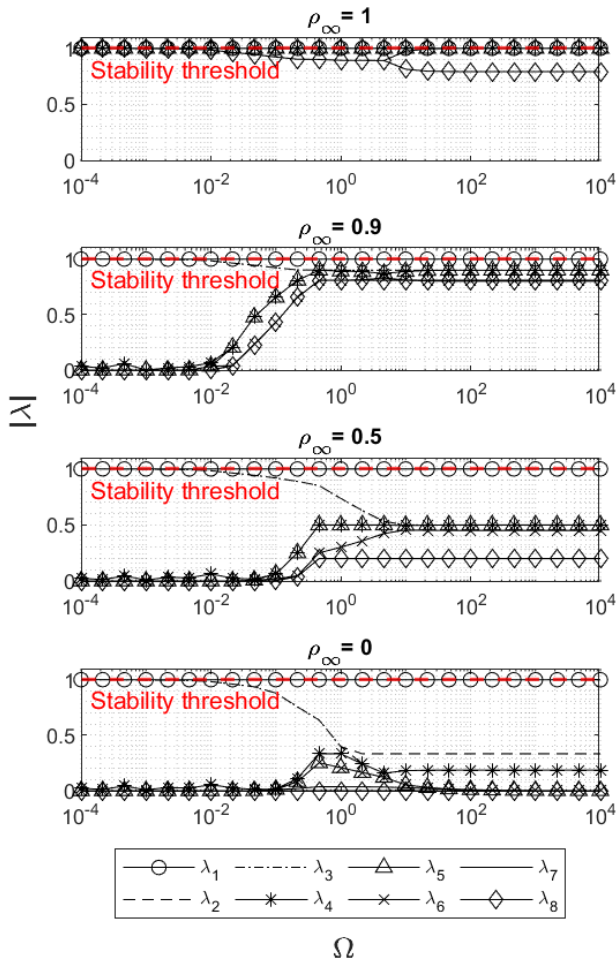
(b)
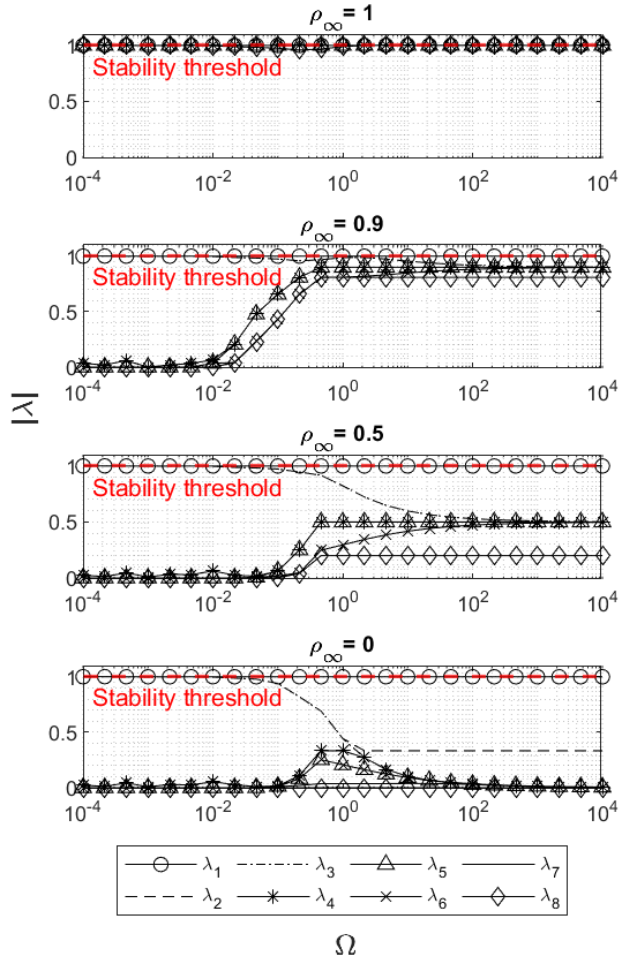
(c)

Figure 5.7: S-Model: Stability analysis: (a) η = 0.50, (b) η = 0.75 and (c) η = 1.00.

(a)

(b)

(c)
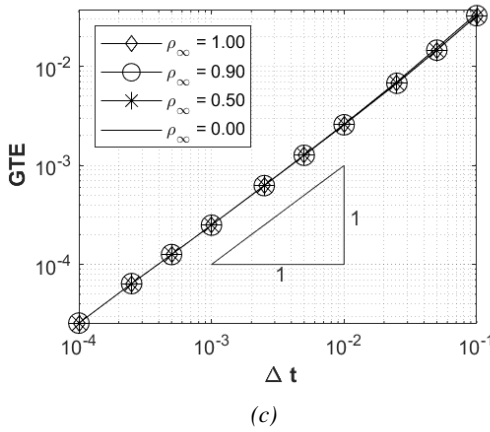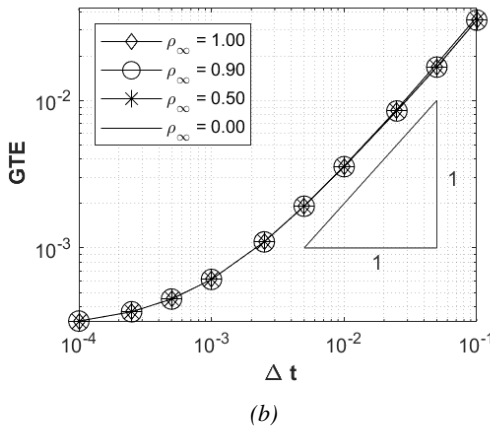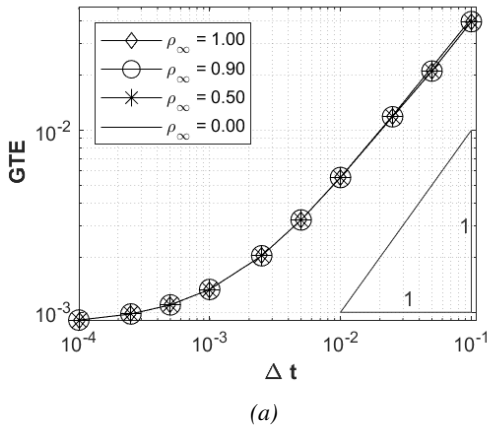
Figure 5.8: S-Model: Global Truncation Error on the displacement: (a) $\eta =$ 0.50, (b) $\eta = 0.75$ and (c) $\eta = 1.00$.

5.3   Experimental results

In this Section, the main results of the laboratory test are reported to
prove the effectiveness of the algorithmic correction proposed. Figures 5.9 and 5.10 depict the displacements imposed by the controller
and the one determined on the reference model, built in the finite element software OpenSees, for DRLF-HSS tests at different limit states.
It can be noticed that the discrepancies are significantly small, as also
confirmed by Table 5.3, where the distance between the two values is
computed in terms of NRMSE expressed in terms of percentage, Equation 3.11. Similar consideration can be done by observing the comparison in terms of base shear, reported in Figure 5.11.

$$RMSE = \frac{\|x_i - x_j\|_2}{\sqrt{N}} \tag{5.6}$$

In Table 5.4, the RMSE, defined in Equation 5.6, between the correction
and the algorithmic force is reported and normalised with respect to the
maximum algorithmic force. It can be noticed that the amount of corrected force decreases as the intensity of the earthquake increases, with
a maximum value of 26.9% and a mean value of 13.4%. This reflects the
fact that the correction forces serve mainly to account for the initial gaps,
whose effects are compensated already at low intensities. Therefore, the
correction forces do not significantly increase when the intensity of the
earthquake further increases.

		Damage Limitation [%]	Significant Damage [%]	Near Collapse [%]
Displacement	Lower Actuator	5.6	6.4	5.7
	Upper Actuator	5.7	5.7	4.9
Base Shear		5.8	6.4	7.5

*Table 5.3: NRMSE between the Hybrid Simulation and OpenSees reference
model of DRLF-HSS tests.*
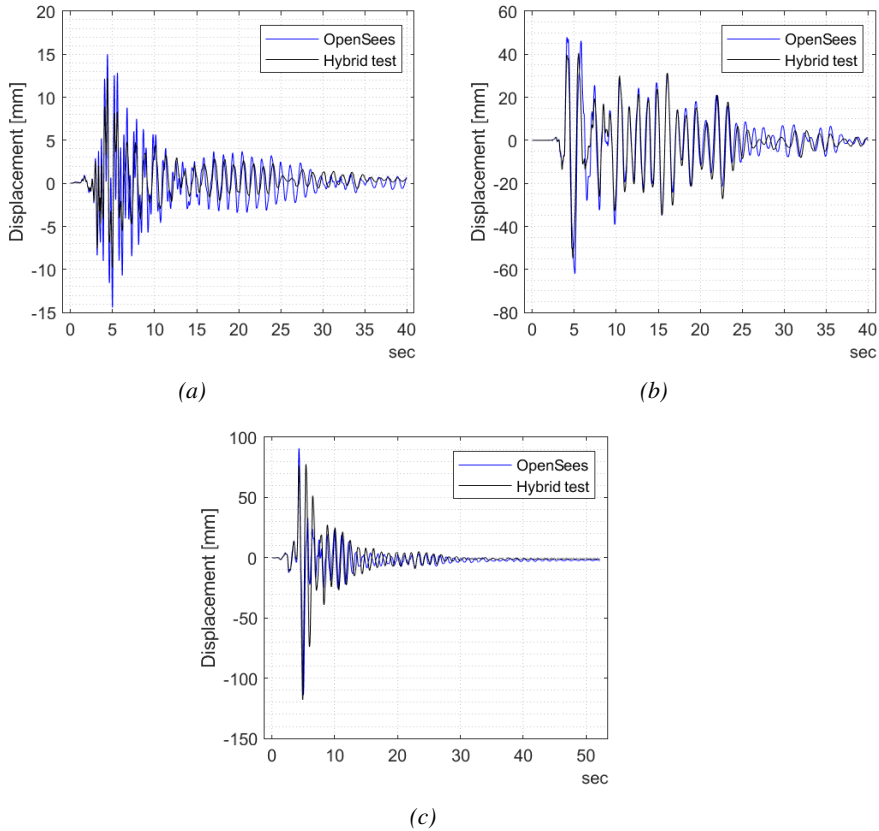
Figure 5.9: Displacement comparison at upper actuator level between OpenSees reference model and hybrid simulation at: (a) DL, (b) SD and (c) NC limit states of DRLF-HSS tests.

(a)

(b)

(c)
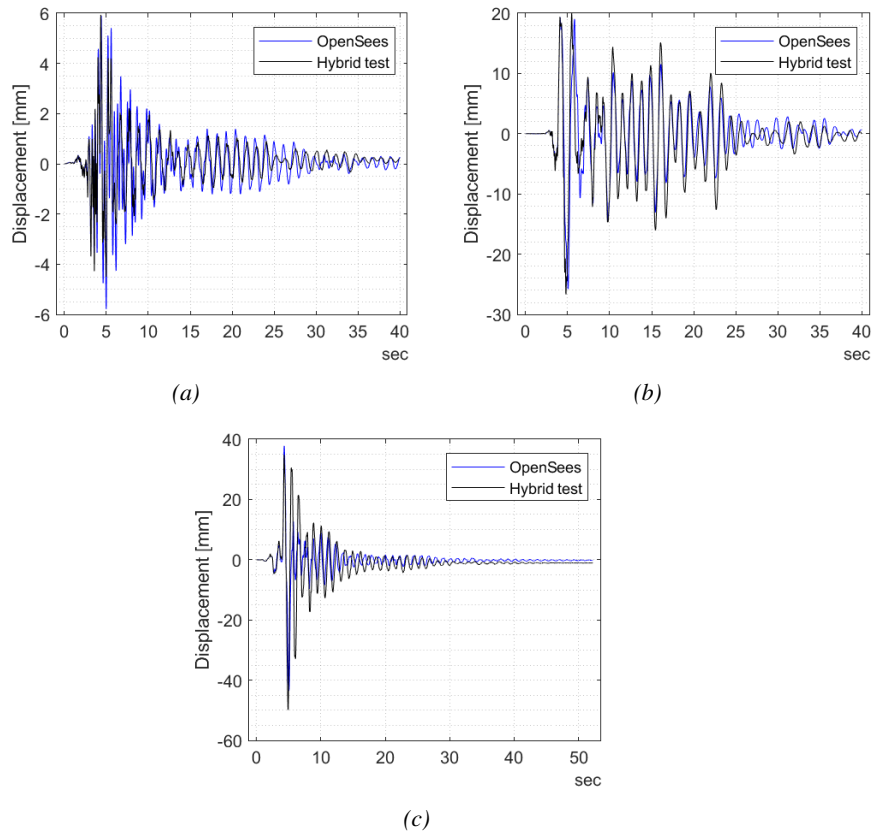
*Figure 5.10: Displacement comparison at lower actuator level between
OpenSees reference model and hybrid simulation at: (a) DL, (b) SD and (c)
NC limit states of DRLF-HSS tests.*

(a)

(b)

(c)
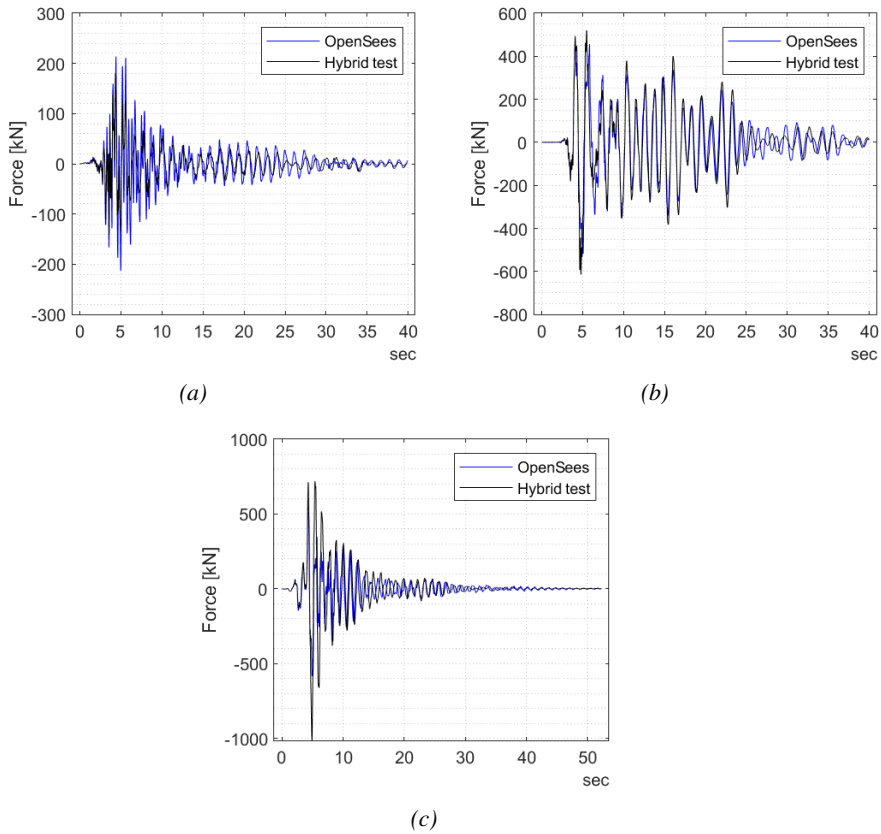
Figure 5.11: Force comparison between OpenSees reference model and hybrid simulation at: (a) DL, (b) SD and (c) NC limit states of DRLF-HSS tests.

		Damage Limitation [%]	**Significant Damage** [%]	**Near Collapse** [%]
DRBeS	Lower Actuator	14.6	14.6	5.9
	Upper Actuator	26.9	26.9	2.1
DRLF-MS	Lower Actuator	11.6	11.8	9.5
	Upper Actuator	15.1	17.0	14.3
DRLF-HSS	Lower Actuator	11.8	19.5	10.9
	Upper Actuator	7.4	14.0	13.3
DRBrC-MS	Lower Actuator	19.3	9.3	9.5
DRBrC-HSS	Lower Actuator	18.2	9.1	9.7

Table 5.4: RMSE of the correction over the maximum applied force of all the performed tests.

5.4 Conclusions

This Chapter describes the validation of a novel algorithmic correction suited for the PG-α algorithm in hybrid simulation. Via an extensive investigation, stability and accuracy were studied for the PG-α algorithm along with the proposed correction, considering realistic sources of error, e.g. delay and noise in the signal, calibrated on real experimental tests. For this purpose, a Simulink model was developed and analysed.

Firstly, the laboratory data were analysed to calibrate the parameters of the Simulink model. Subsequently, stability and accuracy analyses were performed, proving that the algorithm is stable for values of η lower than one and first-order accurate independently from the value of η. In particular, when η is lower than the unit, the global truncation error has an asymptotic trend for small values of Δt. In order to confirm the effectiveness of the proposed correction in real experimental tests, the results of an experimental campaign carried out at the University of Trento, in which the algorithmic correction was employed, were illustrated. These results showed that the hybrid simulation displacements and forces were in excellent agreement with those of the numerical reference model previously developed. Moreover, the percentage of correction was always lower than the 30% of the force feedback and decreased as the intensity of the earthquake increased, i.e. for limit states with increasing severity.

Chapter 6

Probabilistic seismic demand model

In this Chapter, incremental dynamic analyses were exploited to investigate the influence of equipping steel frames with DRLF system. In particular, the DISSIPABLE frame behaviour was compared with a state-of-the-art moment-resisting frame designed according to the capacity design philosophy. The frame has the same geometry as the DISSIPABLE structure so that differences in the behaviour can be highlighted under the same design conditions. In addition, experimentally calibrated fragility curves were derived through IDAs.

6.1 Numerical modelling of the case studies

The frames were designed and modelled respectively with the finite element software SAP2000 and OpenSees. With the purpose of having a high-fidelity model for the DRLF frame, the benchmark model was calibrated on the results of laboratory full-scale tests previously described. Moreover, the non-linear behaviour of the device was modelled by means of analytical formulations to determine meaningful fragility curves for structural designers.

6.1.1 State of the art model

The moment resisting frame in the study was designed according to the provisions of Eurocode 8. The design process involved performing linear dynamic analysis using the SAP2000 finite element software. The frame considered was a six-storey frame with two spans, as illustrated in Figure 6.1. It is important to note that the frame's geometry was in-

tentionally chosen to match that of the DISSIPABLE structure, resulting in different dynamic characteristics, as shown in Table 6.1. To capture the non-linear behaviour of the structure, fibre elements were employed to model both the columns and composite beams. The choice of fibre elements was made based on preliminary analyses conducted according to Pecce and Rossi [97], which indicated that significant buckling effects did not develop in the steel beams. Instead of concentrated plasticity models, the spread of plasticity was described using fibre elements. Rayleigh damping was applied to the first and third modes of the frame, with a damping ratio of 5% as recommended by Chopra [98] for bolted steel structures. However, for the DRLF structure, the damping ratio was set to 2% since the presence of dissipative components in the structure is expected to result in lower viscous damping compared to a structure designed using the capacity design approach.
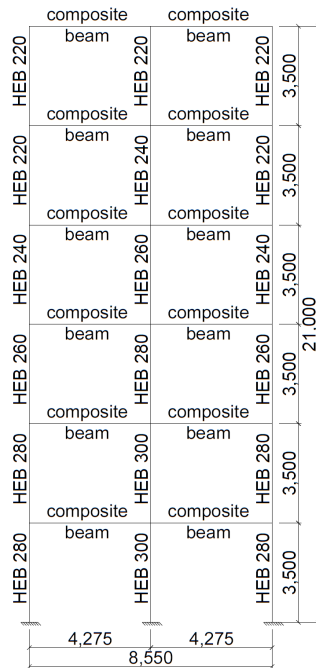
Figure 6.1: SoA: Frame model.

To establish the threshold for limit states in relation to beam hinge rotations, the calculation of the yielding rotation of the beams was conducted. Assuming a shear-type deformation of the structure, the rotational capacity was determined as reported in Equation 6.1. In this equation, θ_y represents the yielding rotation, $M_{pl,beam}$ is the plastic bending resistance, L_{beam} denotes the beam length, E represents the elastic

Mode	Periods [s]
1	1.08
2	0.36
3	0.21

Table 6.1: SoA: Vibration periods.

modulus and I_{beam} stands for the moment of inertia of the beam. The resulting rotational capacities for the beams were computed using these parameters and are detailed in Table 6.2.

$$\theta_y = \frac{M_{pl,beam}}{k_{\varphi,beam}} = M_{pl} \frac{L_{beam}}{6 \, E \, I_{beam}} \tag{6.1}$$

	Positive	Negative
$M_{pl,beam}$ $[kNm]$	233.00	188.5
I_{beam} $[mm^4]$	$1.17 \cdot 10^5$	$7.08 \cdot 10^4$
θ_y $[rad]$	$6.75 \cdot 10^{-3}$	$9.03 \cdot 10^{-3}$

Table 6.2: SoA: Rotational capacity.

6.1.2 DRLF model

The IDAs for the DRLF system were performed on a six-storey frame with two spans, as for the frame experimentally tested, and depicted in Figure 6.2. For this frame, the non-linearity was concentrated at the RBSs and, differently from pseudo-dynamic tests, for the hysteretic behaviour a piece-wise model, namely "modified Ibarra-Krawinkler deterioration model with bilinear hysteretic response" [99–102], was implemented to reproduce the non-linear behaviour. The parameters which define the numerical model can be analytically determined starting from the mechanical characteristics of the RBSs following INNOSEIS provision. In particular, Table 6.3 indications were used to compute the monotonic curve.

137
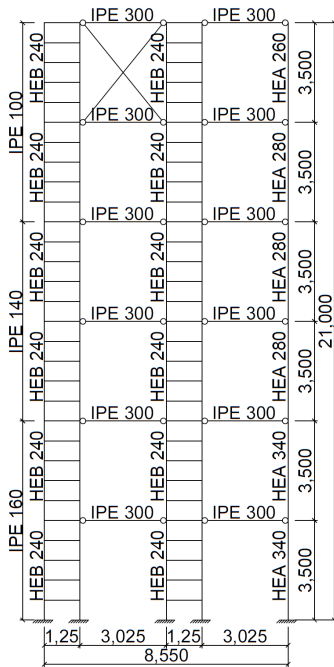
Figure 6.2: DRLF: Frame model.

	$M/M_{pl,RBS}$	$\theta/\theta_{pl,RBS}$
-E	-0.6	-45
-D	-0.6	-40
-C	$-\alpha_{pl}$	-40
-B	-1	-1
A	0	0
B	1	1
C	α_{pl}	40
D	0.6	40
E	0.6	45

Table 6.3: RBS: Non-linear hinge parameters.
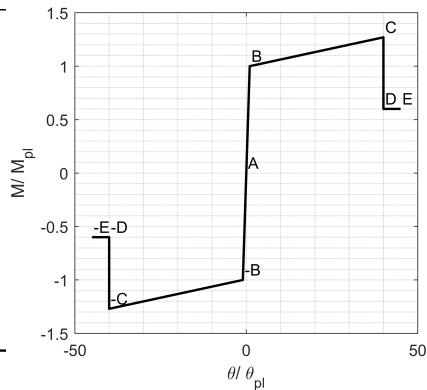
Figure 6.3: RBS: Monotonic shape.

In detail, point C ordinate was obtained considering for the strain hardening α_{pl}, the formula proposed by AISC341-10 [103], Equation 6.2.

$$\alpha_{pl} = \frac{f_y + f_u}{2f_y} \tag{6.2}$$

To calculate the plastic rotation of the RBS, the formulation proposed
by Dougka et al. was adopted whilst the plastic moment was calculated
according to Eurocode 8-3, Equation 6.3.

$$\theta_{pl,RBS} = \frac{W_{pl,RBS} \ f_y \ L_{RBS}}{6 \ E \ J \ I_{RBS}}$$

$$M_{pl,RBS} = Z_{pl,RBS} \ f_{yb}$$

(6.3)

Those parameters were found to be in accordance with the results
of the experimental campaign, see Figures 6.4 to 6.6, where the re-
sults of the hybrid simulation are superimposed with the outcome of the
OpenSees reference model where the RBSs were modelled once with
Bouc-Wen and once with IMK models.
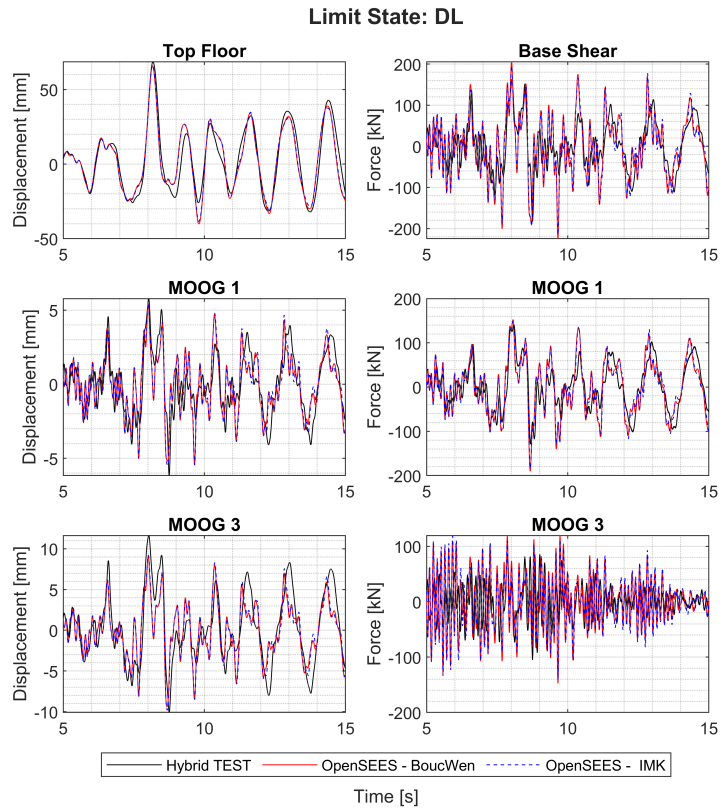
*Figure 6.4: DL - Comparison between hybrid test and OpenSees reference mod-
els.*
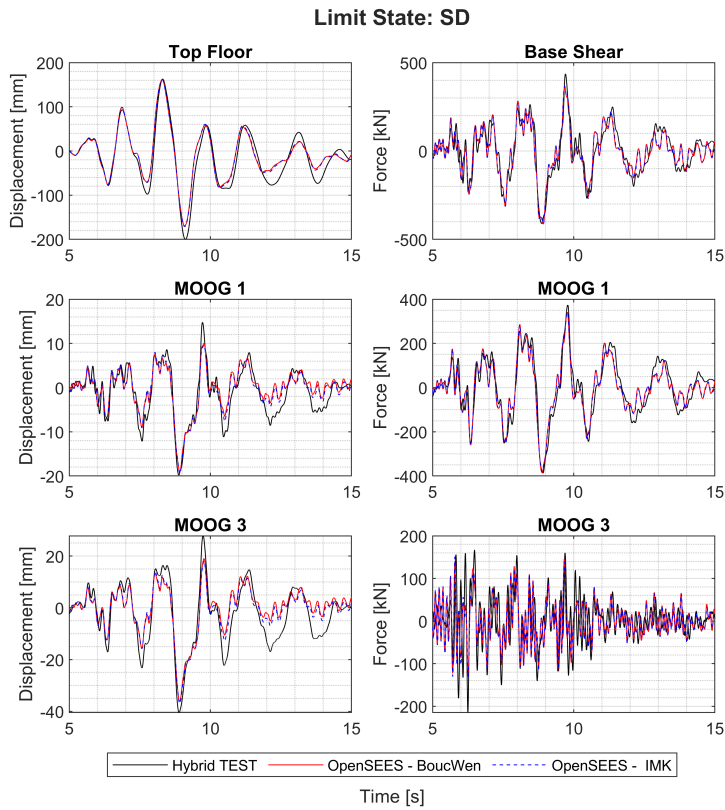
Figure 6.5: SD - Comparison between hybrid test and OpenSees reference models.
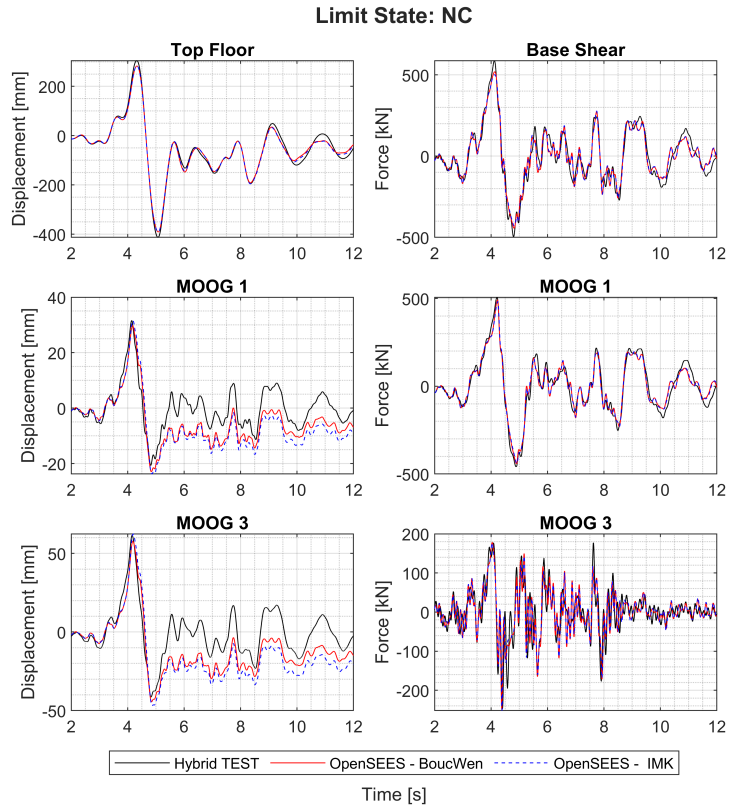
Figure 6.6: NC - Comparison between hybrid test and OpenSees reference models.

In the OpenSees model used to perform IDAs, beams and braces were modelled with elastic elements, since buckling, as well as plasticity, did not occur, whilst fibre elements were employed for the columns, to account for plasticity and to detect the column-base yielding. The modal characteristics of the structure are listed in Table 6.4 whilst the IMK model values are reported in Table 6.5 whose quantities refers to Figure 6.7.

Mode	Periods [s]
1	1.38
2	0.35
3	0.19

Table 6.4: DRLF: Vibration periods.

	IPE 160	IPE 140	IPE 100
$k_0 \ [Nm/rad]$	$8.79 \cdot 10^6$	$5.42 \cdot 10^6$	$1.57 \cdot 10^6$
$a_{s,pos} \ [-]$	0.0069	0.0069	0.0069
$a_{s,neg} \ [-]$	-0.0069	-0.0069	-0.0069
$M_{y,pos} \ [Nm]$	24343.64	17242.44	7730.91
$M_{y,neg} \ [Nm]$	-24343.64	-17242.44	-7730.91
$\theta_{p,pos} \ [rad]$	0.1080	0.1240	0.1919
$\theta_{p,neg} \ [rad]$	-0.1080	-0.1240	-0.1919
$\theta_{pc,pos} \ [rad]$	0.02	0.02	0.02
$\theta_{pc,neg} \ [rad]$	-0.02	-0.02	-0.02
$M_{r,pos} \ [Nm]$	0.6	0.6	0.6
$M_{r,neg} \ [Nm]$	-0.6	-0.6	-0.6
$\theta_{u,pos} \ [rad]$	0.1247	0.1431	0.2215
$\theta_{u,neg} \ [rad]$	-0.1247	-0.1431	-0.2215

Table 6.5: RBS: IMK parameters
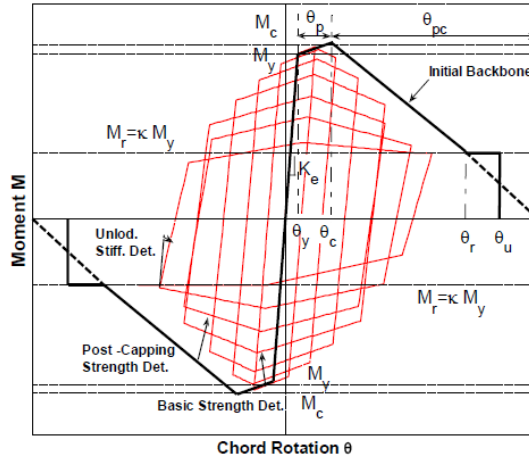
Figure 6.7: IMK material [101].

6.2 Fragility methods and ground motion selection

6.2.1 Formulation of fragility models

The numerical simulations were conducted using the incremental dynamic analysis [104] technique on FE models built in OpenSees. A suite of representative ground motion records was used and then scaled to various intensity levels. To reduce the computational burden, the maximum intensity level was determined based on reaching either a maximum inter-storey drift ratio of 5% or a predefined maximum value of intensity. The former corresponds to the collapse limit state according to FEMA356 guidelines for moment resisting frames [94]. At the same time, the latter was determined through preliminary analyses to ensure an adequate number of ground motions leading to structural collapse. To prevent numerical divergence at low-intensity levels, the time step interval (Δt) for each ground motion record was reduced up to a minimum value of 0.0005s.

An IDA curve was derived for each ground motion, relating an intensity measure (IM) to an engineering demand parameter (EDP). The selected intensity measure, as discussed by Vamvatsikos and Cornell [104], was the spectral acceleration at the first mode of vibration period (Sa_{T1}) in the direction of the frame.

Following IDAs, fragility functions were estimated for different levels of EDP, corresponding to specific limit states. These fragility functions are essential for conducting seismic risk assessments. The proce-

dure employed to construct the fragility functions followed the approach described by Baker [105], which assumes that an IM causing the exceedance of a limit state, identified as C, follows a lognormal cumulative distribution function, see Equation 6.4.

$$P\left(C|IM = x\right) = \Phi\left(\frac{\ln\left(x/\theta\right)}{\beta}\right) \tag{6.4}$$

where $\Phi()$ is the standard normal cumulative distribution function (CDF), θ is the median of the fragility function, and β is the standard deviation of $\ln(IM)$. After performing IDA for a set of n accelerograms, a set of IMs associated with the onset of collapse is obtained. In the case that all the records lead to structural collapse within the maximum IM value, estimations of θ and β are obtained from this set of IM, assuming it to be lognormally distributed, see Equations 6.5 and 6.6.

$$\ln\hat{\theta} = \frac{1}{n}\sum_{i=1}^{n}\ln IM_i \tag{6.5}$$

$$\hat{\beta} = \sqrt{\frac{1}{n-1}\sum_{i=1}^{n}\left(\ln\frac{IM_i}{\hat{\theta}}\right)^2} \tag{6.6}$$

Nevertheless, when the analyses were conducted up to a predefined value of IM, only m (where $m \leq n$) ground motions resulted in the exceedance of the limit state. There is insufficient data for the remaining n-m records to estimate fragility functions using the previously mentioned equations directly. In such cases, the maximum likelihood method is employed to extrapolate the parameters of the fragility functions. The likelihood function for the entire dataset is obtained by assuming that all n values of IM for each ground motion are independent of each other. Therefore, considering both the likelihood function of the m ground motions that lead to collapse and the likelihood function of the n - m ground motions that do not result in collapse at the maximum IM value, the likelihood function for the entire dataset can be defined as follows:

$$Likelihood = \left(\prod_{i=1}^{m}\Phi\left(\frac{\ln IM_i/\theta}{\beta}\right)\right)\left(1 - \Phi\left(\frac{\ln IM_{max}/\theta}{\beta}\right)\right)^{n-m} \tag{6.7}$$

the function variables are the fragility function parameters θ and β. Such a function gives an estimation of how likely an arbitrary couple of values (θ, β) well represent the set IMi given as input. In general, the estimations of θ and β can be obtained by maximizing the likelihood function.

Maximizing the logarithm of the likelihood function results to be a mathematically equivalent procedure, given the monotonicity of the logarithm function, yet numerically easier. Therefore, the estimation of the parameters is obtained by finding the couple of parameters that maximize the logarithm of the likelihood function:

$$
\begin{aligned}
\left\{ \hat{\theta}, \hat{\beta} \right\} = arg \ \max_{\theta, \beta} \sum_{j=1}^{m} & \left\{ \ln \Phi \left(\frac{\ln {}^{IM_i/\theta}}{\beta} \right) \right\} \\
& + (n - m) \ln \left(1 - \Phi \left(\frac{\ln {}^{IM_{max}/\theta}}{\beta} \right) \right)
\end{aligned}
\tag{6.8}
$$

Finally, an estimation of the cumulative distribution function of the IM for which a certain threshold of collapse is exceeded, i.e. the fragility curve, can be represented by a lognormal distribution whose parameters are $\hat{\theta}$ and $\hat{\beta}$.

6.2.2   Selection of ground motions

A set of 20 accelerograms was employed for the IDAs, selected from the NGA-West2 PEER database [106] and the European database ESM of ORFEUS [107]. The selection included near- and far-field accelerograms, with a Joyner-Boore distance (R_{jb}) of less than 30 km. Additionally, pulse-like records were chosen to ensure a comprehensive representation of various ground motion characteristics. A Consequence class of CC2 and a site category A, as defined in Eurocode 8 part 1-1, were selected for the analysis. These choices were made to ensure consistency with the response spectrum used in the design of the structures. The acceleration spectrum, considering a damping ratio of 2%, is depicted in Figure 6.8.

N°	Database Record Number	Component	Event	Year	Mw
1	A.487	East	Duzce	1999	7.3
2	A.498		Turkey		
3	E.SRC0	East	Friuli 3rd shock Italy	1976	6
4	EU.ULA	East	North-western Balkan	1979	6.9
5		North	Peninsula		
6	IT.MRM	East	Cosenza Italy	2012	5.2
7	IV.EVRN	East	Sicily Italy	2018	4.9
8	IV.T1212	North	Central Italy	2016	6.5
9	KO.GMLD	North	Dodecanese Islands Greece	2020	7
10	TK.4101	East	Izmit Turkey	1999	7.6
11	RSN 763	North	Loma Prieta California	1989	6.93
12	RSN 809	North			
13	RSN 810	East			
14	RSN 989	North	Northridge 1st shock California	1994	6.69
15	RSN 1011	East			
16	RSN 1091	East			
17	RSN 1161	East	Kocaeli Turkey	1999	7.51
18	RSN 1165	North			
19	RSN 4483	East	L'Aquila Italy	2009	6.3
20	RSN 5618	North	Iwate Japan	2008	6.9

Table 6.6: Selected time histories.
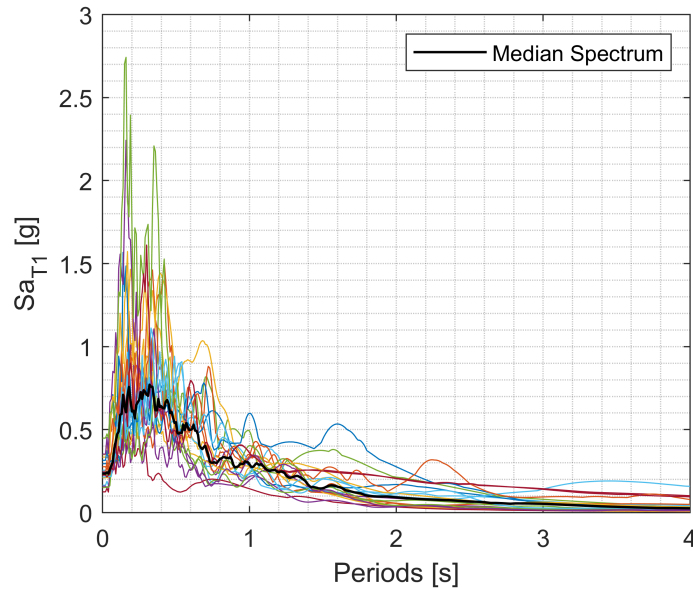
Figure 6.8: Response spectra of the selected records ($\xi = 2\%$).

6.3 Seismic performance

6.3.1 Definition of the limit states

In order to assess the behaviour of the structures, two significant EDP
were identified: in terms of global quantities, the Peak Interstorey Drift
Ratio (PIDR) was considered whilst, concerning local quantities, the de-
formation of the dissipative elements, i.e.:

- the rotation of the RBSs for DRLF frame;

- the rotation of the plastic hinges, for MRF.

was taken into account.

To define the exceedance of limit states, the following threshold were
considered for PIDR in accordance with FEMA356 provisions for mo-
ment resisting frames:

- 0.7%, that is conventionally defined as the DL limit state threshold.

- 2.5%, that is conventionally defined as the SD limit state threshold.

- 5.0%, that is conventionally defined as the NC limit state thresh-
  old.

The provisions of Eurocode 8-3 were considered for the local parameters. Specifically, for the RBSs sections, the threshold values in Table 6.7 were considered. For the plastic hinges of the SoA frame, the criteria indicated in Table 6.8 were used as references for different limit states.

DL	SD	NC
0.010	0.025	0.040

Table 6.7: Required rotation capacity of RBSs [72].

Class of cross section	DL	SD	NC
1	$1.0\,\theta_y$	$6.0\,\theta_y$	$8.0\,\theta_y$
2	$0.25\,\theta_y$	$2.0\,\theta_y$	$3.0\,\theta_y$

Table 6.8: Plastic rotation capacity at the end of beams [72].

In addition, the median value of EDP for which the first column base section reaches the yielding of the outer fibres was also considered. The value is inherently different for each structure.

The performance levels are defined as exceeding the threshold mentioned above, which represents the so-called EDP-based rule [104] i.e. the EDP is the damage indicator whose value determines in which limit state the structural model is. Hence, these values were also considered to evaluate the fragility curves.

6.3.2 Probabilistic seismic demand analysis through IDAs

The results of IDAs are reported with respect to the first period spectral acceleration, as depicted in Figures 6.9 and 6.10: in the former, the peak interstorey drift ratio was taken as EDP whilst in the latter the maximum rotation of the dissipative zones was considered.

From Figures 6.9 and 6.10, it may be noted that the maximum IM value chosen for the SoA structure is 3g; otherwise, for the DRLF frame is equal to 2g. Different maximum IM values were chosen due to the higher stiffness of the moment-resisting frame, which needs stronger inputs to provide the same displacement value. Indeed, using a maximum IM value of 2g also for the SoA frame, the number of accelerograms leading to the collapse of the structure would not have been sufficient to derive a reliable fragility curve.

From Figure 6.9a can be highlighted that, since the EDP-based rule is used, given a unique value of EDP threshold, multiple limit-state points on an IDA curve can be identified. This was handled conservatively, considering the lowest value of IM. In Figure 6.9b the IDAs curves of DRLF frame were reported. It can be highlighted that, for $Sa_{T1} \leq 0.2g$, the structure is in the elastic range and the data have low variability. Instead, the higher dispersion of the results for $Sa_{T1} > 0.2g$ is due to the characteristics of the system. Indeed, compared with the SoA frame, the DRLF system presents the highest number of devices and owing to the progressive plasticisation of such devices, the dynamic characteristics of the frame change during a seismic event. Moreover, since each accelerogram may excite different vibration modes, the order in which the devices plasticise may vary as well, leading from time to time to a different structural response. As shown in Figure 6.9a, certain IDA curves display a distinctive pattern of high response at a specific level of intensity, with a lower response at higher seismic intensities. This is because when the accelerogram is scaled up, the vulnerable response cycles at the beginning of the response time history can cause damage and modify the structure's characteristics for the subsequent, stronger cycles [108].

(a)

(b)
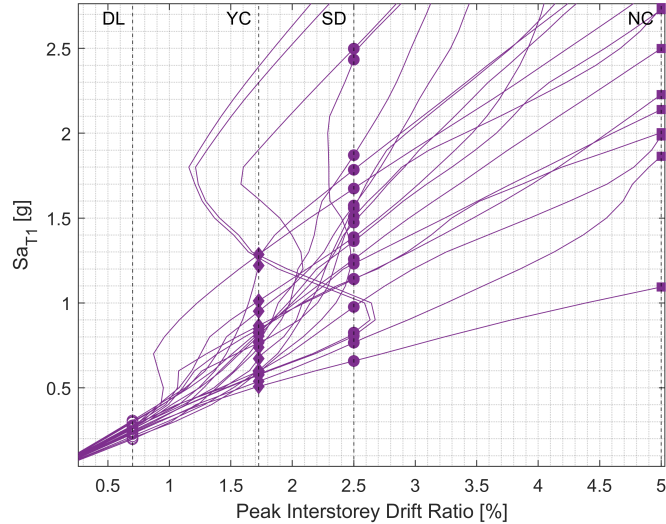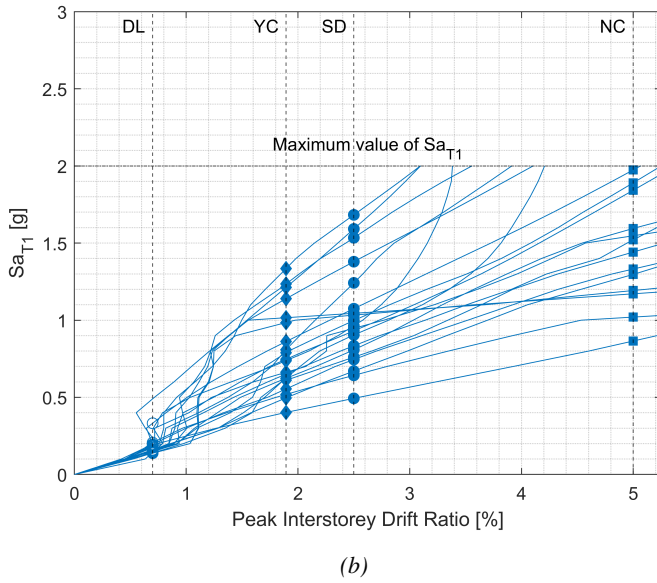
Figure 6.9: IDA curves with global EDP of: a) SoA and b) DRLF Frame.

(a)

(b)
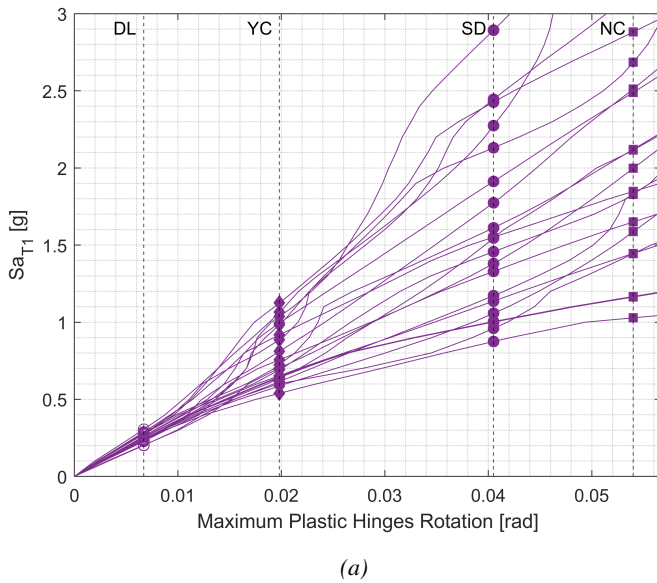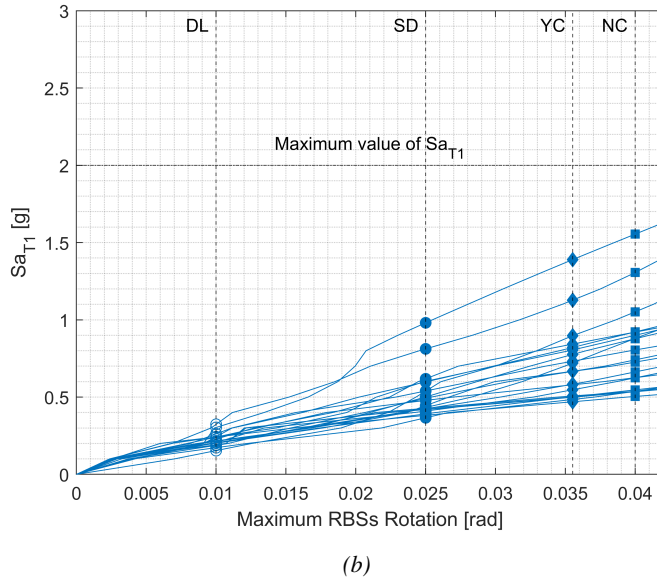
Figure 6.10: IDA curves with local EDP of: a) SoA and b) DRLF Frame.

The results of the IDAs were further processed to generate capacity curves, which involve plotting the maximum top floor displacement against the maximum base shear for each intensity measure (see Figure 6.11). These curves were then compared with the results obtained from static non-linear analysis to assess the similarities and differences between static and dynamic properties. In particular, pushover analyses were conducted using a lateral load distribution defined by:

$$\overline{\mathbf{F}_i} = \mathbf{m}_i \cdot \overline{\mathbf{\Phi}_i} \tag{6.9}$$

Here, m_i represents the mass of the i-th node, and $\overline{\Phi}_i$ denotes the normalized mode of vibration corresponding to the highest value of the effective modal mass, as defined in Eurocode 8 part 1-1.
Figure 6.11a illustrates the capacity curves of the SoA frame in comparison with the non-linear static curve. It can be observed that the initial elastic stiffness estimated through the pushover analysis aligns with the dynamic stiffness, while the IDAs exhibit a different non-linear behaviour that allows for higher base shear values. Additionally, Figure 6.11b highlights that the dynamic capacity curves for the DRLF frame differ from the pushover curve, as the non-linear dynamic analyses consider the contribution of high modes, which is neglected in pushover analysis.

(a)

(b)
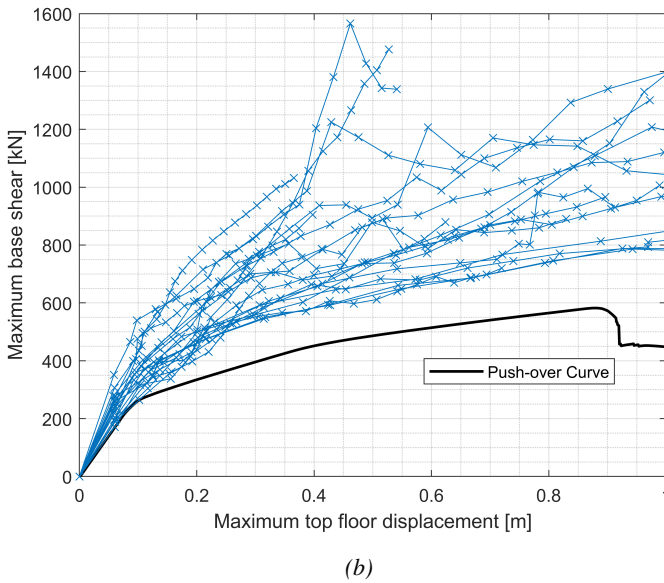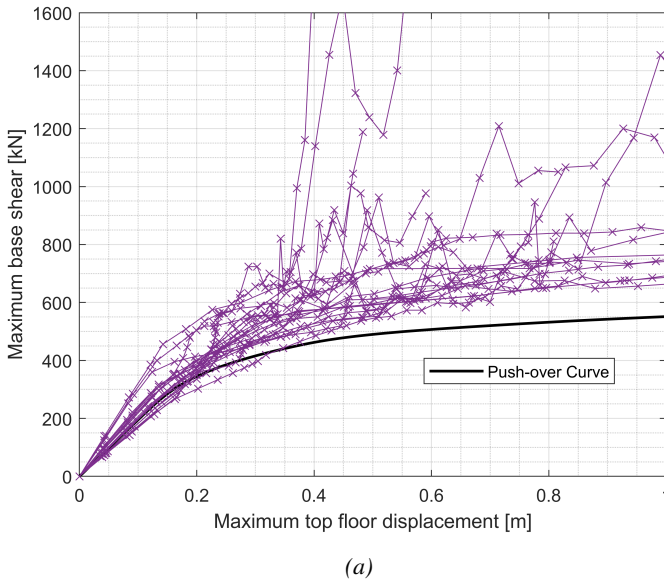
Figure 6.11: Capacity curves of: a) SoA and b) DRLF Frame.

6.3.3 Fragility functions

In this paragraph, the fragility curves for the previously illustrated frames are shown. Firstly, from all figures, it can be deduced that the probabil-

ity determined analytically, according to the procedure illustrated above, well reproduces the data distribution for both limit states. In addition, the maximum IM value used in the analyses is shown for all the structures, i.e. 2g for the DRLF structures and 3g for the SoA building.

Considering the SoA frame, it can be pointed out that the choice of a local or global EDP does not affect the probability of collapse of the structure. Indeed, as can be seen from figures Figures 6.12b and 6.13b, the collapse probability associated with the various limit states calculated considering the peak interstorey drift ratio is comparable to that computed with the maximum rotation of the plastic hinges. This demonstrates the accuracy of interstorey drift limits in identifying limit states.

Differently, for the DRLF structure, there are similar results between the two EDPs only for the damage limit state and the limit state identified by the yielding of the column base. This could be due to the high stiffness that the DRLF system retains after the first yielding of the devices. As a favourable output of considering a local EDP, the collapse probability associated with column yielding is higher than that associated with the significant damage limit state, which demonstrates the capability of the structure to avoid elements' plasticisation before the design limit state. This result aligns with the experimental campaign and the preliminary numerical analyses where no column yielding was individuated before the SD limit state.

(a)

(b)
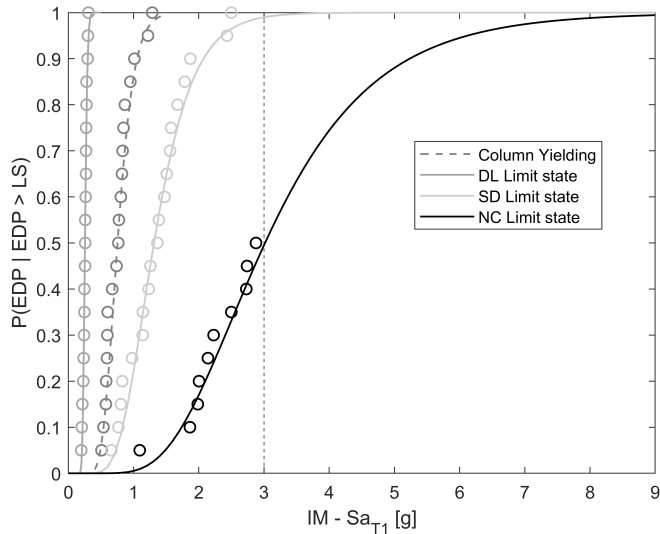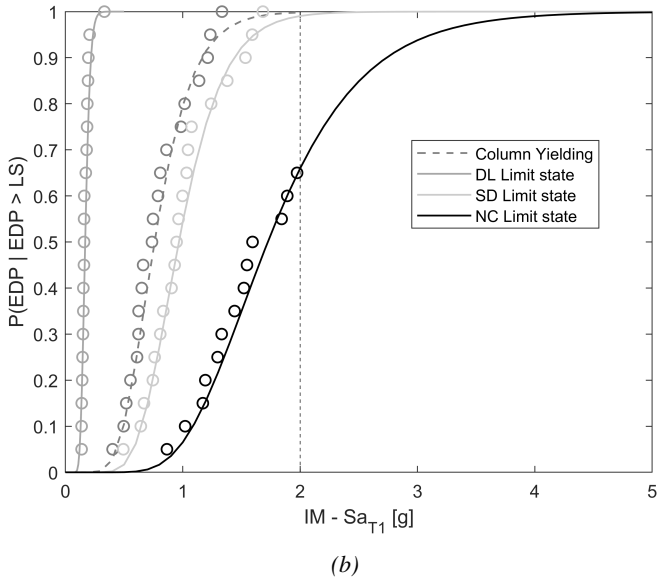
Figure 6.12: Fragility Curves for global EDP (PIDR) of: a) SoA and b) DRLF Frame.

(a)

(b)
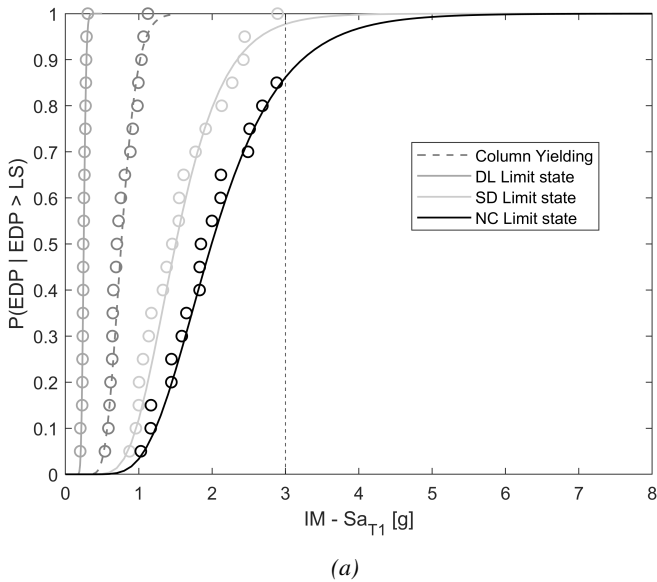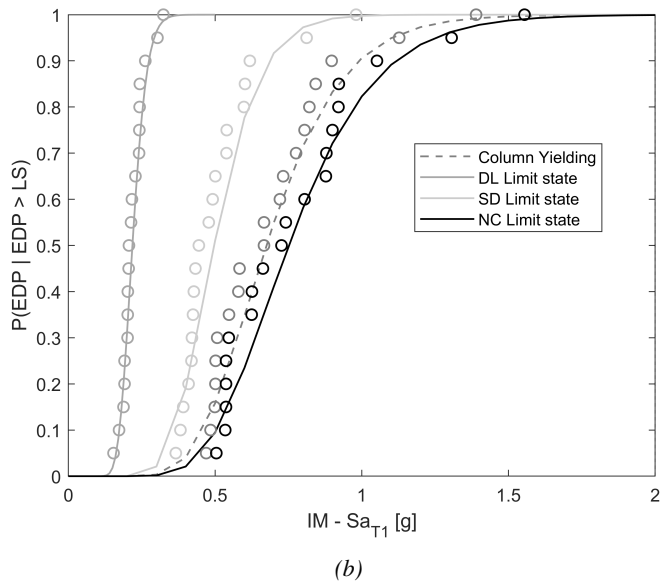
*Figure 6.13: Fragility Curves for local EDP (Maximum Rotation) of: a) SoA
and b) DRLF Frame.*

6.4 Discussion of the results

Hereafter the comparison between the results obtained from the analyses
of the structures is described. By comparing the dynamic characteristics,
despite the two structures having the same geometry, the first period of
the SoA structure is 22% lower than that of the DRLF frame, as can be
seen from Tables 6.1 and 6.4. Furthermore, the structures were designed
under the same gravity and seismic loads, therefore a lower first period
implies the SoA frame being stiffer than the others. In Figure 6.14 the
comparisons in terms of fragility curves at the four limit states previously
identified are reported. Concerning Figure 6.14b which describes the
probability of exceedance of the Peak Interstorey Drift Ratio for which
the first yielding of the column base occurs, the State-of-the-Art frame
and the DRLF frame show a comparable probability of collapse. In con-
trast, for the other limit states it can be seen from the Figures 6.14a, 6.14c
and 6.14d that the SoA frame always has a lower probability of collapse
than the frame equipped with the DRLF system. Nevertheless, this is not
an unfavourable outcome since the presence of the devices guarantees
their replaceability and, therefore, the reparability of the structure after
seismic events, including at the collapse limit state.
Moreover, it should be highlighted that in the DRLF Frame the concen-

tration of plasticity in the devices allowed for an optimised design with smaller sections for beam and column. Conversely, the SoA structure was designed with conservative assumptions, in order to have a flexible design that can withstand different actions and could be later optimised. In future developments, the SoA structure will be redesigned with optimised sections, to obtain a more meaningful comparison. Nevertheless, it should be highlighted that in a more holistic framework, accounting for the costs or the environmental impact of the structure, the SoA frame could be the worst solution though providing a lower probability of collapse.

(a)

(b)

(c)

(d)
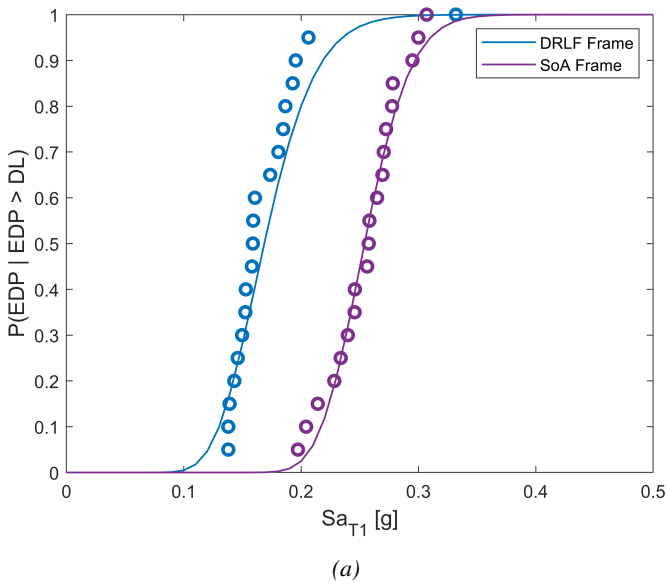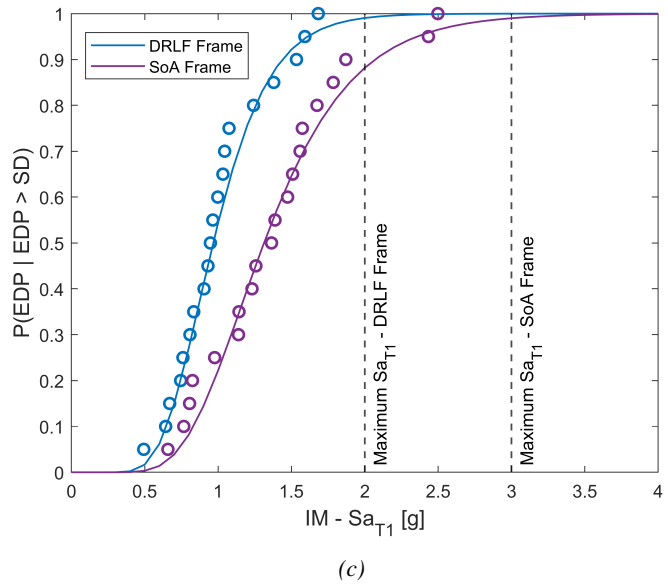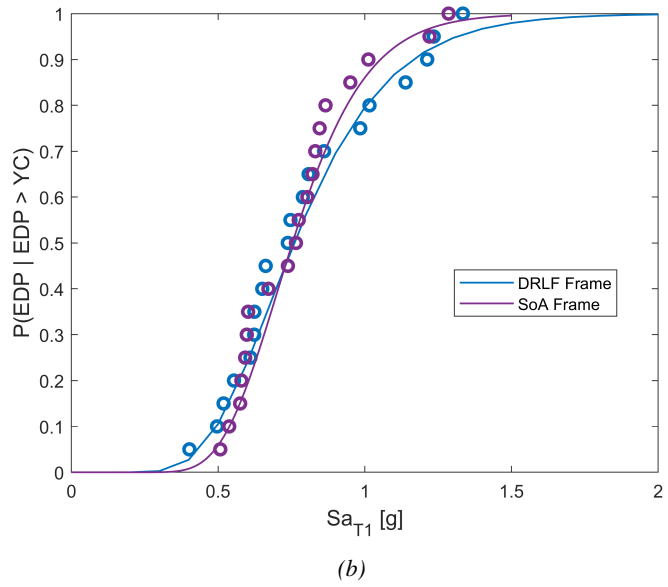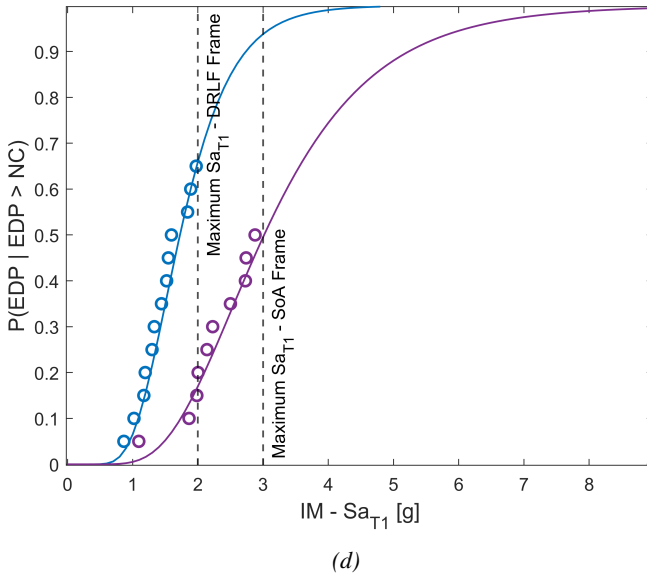
Figure 6.14: Fragility curves comparison at significant Peak Interstorey Drift Ratio: a) DL, b) Yielding Column, c) SD and d) NC limit state.

In Figures 6.15 and 6.16, the overlapping of the IDA and capacity curves for the structures are reported, respectively. In both cases, the percentiles 50, 16 and 84 were employed for the comparison as suggested by Vamvatsikos and Cornell since they represent the median value and the median times e to the $\pm$ the dispersion, $mean \cdot e^{\pm\sigma}$.

The comparison of both Figures 6.15 and 6.16 reveals some noteworthy differences in the behaviour of the DRLF system with respect to the SoA model. In Figure 6.15, it is evident that the DRLF frames initially exhibited a lower stiffness compared to the SoA frames. This can be attributed to the introduction of dissipative devices within the frame, which enhances structural deformability. However, as the intensity level increases and the frames experience yielding, the DRLF system preserves higher stiffness due to the elevated number of devices present. In contrast, the SoA model, which lacks in dissipative devices, experiences a more significant reduction in stiffness following yielding.

Additionally, the DRLF system showed a high deformation capacity, comparable to that of the SoA model, as depicted in Figure 6.16, emphasizing its effectiveness in adjusting significant structural deformations while preserving structural integrity.
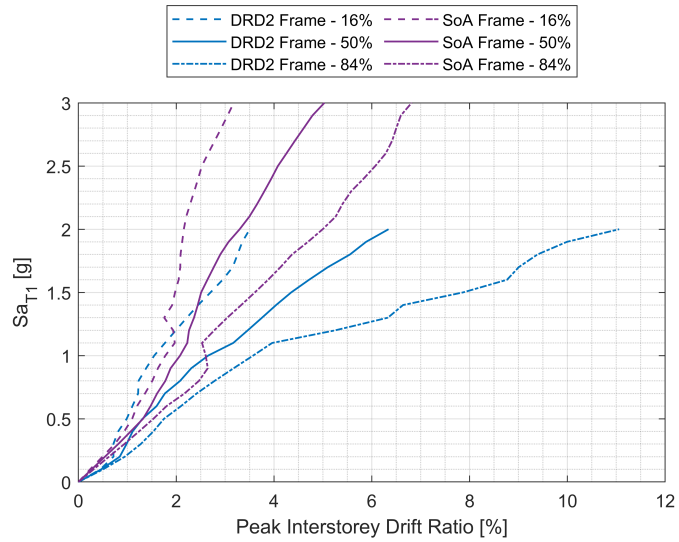
Figure 6.15: IDA curves comparison between SoA Frame ad DRLF Frames.
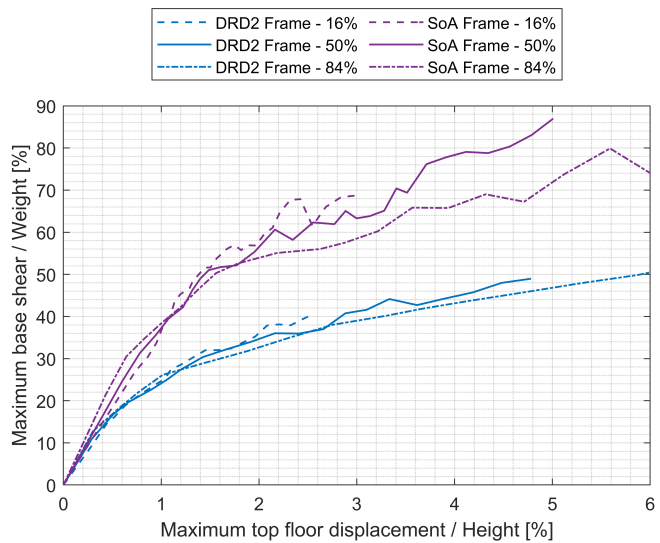
Figure 6.16: Capacity curves comparison between SoA Frame ad DRLF Frames.

Chapter 7

Conclusions and future perspectives

7.1   Conclusions

This thesis goes through the experimental campaign carried out at the University of Trento within the framework of the European DISSIPABLE project funded by RFCS. In particular, the first chapter is devoted to the preliminary studies performed on the G-α algorithm implemented to perform hybrid simulation. As a result, it was proved that the algorithm is stable and first-order accurate, considering possible differences between the initial numerically estimated and the physical subdomain's actual stiffness. However, since the G-α algorithm allows for solving first-order equations, this order of accuracy is sufficient. In addition, stability studies proved that the algorithm is stable until the numerically estimated stiffness is greater than the actual one. This outcome aligns with the usual scenario observed in hybrid simulations, where the stiffness of the physical subdomain is calculated using finite element software, resulting in a higher stiffness than the actual physical stiffness. This difference can be attributed to factors such as gaps and post-elastic deformability.

In order to perform experimental tests, numerical analyses conducted on the prototype buildings were needed. In particular, the experimental configurations were identified through a substructuring process. That was required due to the limitation of only having two actuators, so the frame was identified to reduce the number of controlled degrees of freedom. To do that, modal, pushover, and time history analyses were performed, demonstrating that the 2D frame effectively captured the overall behaviour of the 3D building. To study the substructured configuration, a hinge and a vertical constraint were inserted at the actuator position.

The analysis results indicated that the identified substructures accurately represented the behaviour of the two-dimensional frames.

The pseudodynamic hybrid tests provided detailed insights into their non-linear behaviour when subjected to natural earthquake accelerograms. The tests allowed for the analysis of entire frames, including the upper five floors, within the numerical substructure while maintaining the physical substructure at full scale. The tests proved that DISSIPABLE components remained elastic at the DL limit state, exhibited inelastic behaviour at the SD limit state, and experienced significant inelastic behaviour at the NC limit state. The remaining structure behaved elastically for all limit states, proving the device's effectiveness in protecting the structures' irreplaceable parts. Moreover, the replacement of the device between the SD and NC tests occurred without issues, confirming the easy reparability of the frames. Finally, very small residual displacements were observed, which enhanced the self-centring capabilities and quicker repairability.

Based on the results of the experimental campaign, it was possible to perform an a posteriori validation of the algorithm adopted. The Simulink model developed for this purpose took into account realistic sources of error, e.g. delay and noise in the signal, calibrated on real experimental tests along with the proposed correction. The laboratory data were analysed to calibrate the parameters implemented on the Simulink model. Stability and accuracy analyses were performed, proving the algorithm is stable when the numerically estimated stiffness is greater than the actual one. Moreover, it is first-order accurate, independent of the numerically estimated and actual stiffness differences. The effectiveness of the proposed correction was proved by comparing the results of the experimental campaign to those of the reference models, obtaining excellent agreement between the hybrid simulation displacements and forces.

Finally, the results of the experimental campaign were used to calibrate numerical models for which fragility curves were derived and compared with those of a state-of-the-art model. The comparison showed that the SoA frame has a lower probability of collapse for most limit states, except for that associated with the first yielding of the column base, where both frames show comparable probabilities. Nevertheless, the DRLF frame allows for optimized design with smaller sections, while conservative assumptions were made for the SoA structure. The comparison of IDA capacity curves highlighted the DRLF system exhibiting high deformation capacity similar to the SoA model, emphasising its effectiveness in adjusting significant structural deformations while maintaining structural integrity.

7.2 Future Perspectives

The hybrid simulations conducted have demonstrated the favourable performance of the DISSIPABLE replaceable components. The results of the experimental campaign provide substantial evidence that supports the viability and effectiveness of utilizing the devices in structural designs, enhancing the seismic resilience of structures. As a result, integrating these components into current design practices may allow for improving structural safety, reducing repair costs, and extending the service life of buildings and infrastructure.

A concluding workshop was arranged to promote the DISSIPABLE project. Additionally, meetings with relevant stakeholders such as design companies, engineers, and steel producers should be scheduled to aid in the use of the devices in actual structures. Additionally, meetings with relevant stakeholders such as design companies, engineers, and steel producers should be scheduled to promote the use of the investigated components in the design practice. The latter objective will be accomplished by engaging in extensive dialogue with legislative committees and promoting the potential integration of device design guidelines into the forthcoming version of design codes.

In order to thoroughly explore and understand the behaviour of the device within a realistic framework, it is crucial to conduct comprehensive analyses focusing on the components under fire conditions. Such analyses should provide valuable insights into how the device works, withstands, and interacts with fire, enabling researchers to evaluate its safety measures, identify potential vulnerabilities, and develop strategies for enhanced fire resistance and mitigation.

The DISSIPABLE components could also be used as retrofit measures for existing structures. Investigating the feasibility and effectiveness of incorporating dissipative components into the retrofitting process holds great potential for enhancing existing buildings' structural resilience and performance. Implementing dissipative devices as retrofit measures involves analyzing their compatibility with existing structural systems and evaluating their impact on the overall performance. This application could extend the lifespan of buildings, minimize potential risks, and provide sustainable solutions for improving the resilience of our built environment in the face of evolving challenges.

List of Figures

List of Tables

Bibliography

[1] (European Committee for Standardization) CEN. Eurocode 8: Design of structures for earthquake resistance - part 1: General rules, seismic actions and rules for buildings, 2005.

[2] American Society of Civil Engineers. Minimum design loads and associated criteria for buildings and other structures. American Society of Civil Engineers, 2017.

[3] American Institute of Steel Construction. *Seismic Provisions for Structural Steel Buildings*. Number No. 1 in Publication no S341. American Institute of Steel Construction, 1997. URL `https://books.google.it/books?id=1T5SAAAAMAAJ`.

[4] André Plumier. New idea for safe structures in seismic zones. 1990. doi: 10.5169/SEALS-46518. Medium: text/html,application/pdf,text/html Publisher: IABSE.

[5] N.R. Iwankiw and C.J. Carter. The dogbone: a new idea to chew on. *Modern Steel Construction*, 36 (4):18–23, 1996.

[6] Antonella B Francavilla, Massimo Latour, Vincenzo Piluso, and Gianvittorio Rizzano. Design of full-strength full-ductility extended end-plate beam-to-column joints. *Journal of Constructional Steel Research*, 148:77–96, 2018.

[7] Roberto Tartaglia, Mario D'Aniello, and Mariana Zimbru. Experimental and numerical study on the t-stub behaviour with preloaded bolts under large deformations. In *Structures*, volume 27, pages 2137–2155. Elsevier, 2020.

[8] M Latour and G Rizzano. A theoretical model for predicting the rotational capacity of steel base joints. *Journal of Constructional Steel Research*, 91:89–99, 2013.

[9] Pablo Torres Rodas, Farzin Zareian, and Amit Kanvinde. Hysteretic model for exposed column–base connections. *Journal of Structural Engineering*, 142(12):04016137, 2016.

[10] AS Elnashai and AY Elghazouli. Seismic behaviour of semi-rigid steel frames. *Journal of Constructional Steel Research*, 29(1-3): 149–174, 1994.

[11] Sheng-Jin Chen, C. H. Yeh, and J. M. Chu. Ductile steel beam-to-column connections for seismic resistance. *Journal of Structural Engineering*, 122(11):1292–1299, November 1996. doi: 10.1061/ (ASCE)0733-9445(1996)122:11(1292).

[12] Raffaele Pucinotti, Nicola Tondini, Gabriele Zanon, and Oreste S. Bursi. Tests and model calibration of high-strength steel tubular beam-to-column and column-base composite joints for moment-resisting structures: HIGH-STRENGTH STEEL TUBULAR BEAM-TO-COLUMN AND COLUMN-BASE COMPOSITE JOINTS. *Earthquake Engineering & Structural Dynamics*, 44(9):1471–1493, July 2015. doi: 10.1002/eqe.2547.

[13] Rosario Montuori, Elide Nastri, Vincenzo Piluso, and Marina Troisi. Influence of connection typology on seismic response of mr-frames with and without 'set-backs'. *Earthquake Engineering & Structural Dynamics*, 46(1):5–25, 2017.

[14] N. Tondini, G. Zanon, R. Pucinotti, R. Di Filippo, and O.S. Bursi. Seismic performance and fragility functions of a 3D steel-concrete composite structure made of high-strength steel. *Engineering Structures*, 174:373–383, November 2018. doi: 10.1016/ j.engstruct.2018.07.026.

[15] Gregory A MacRae, G Charles Clifton, Hamish Mackinven, Nandor Mago, John Butterworth, and Stefano Pampanin. The sliding hinge joint moment connection. *Bulletin of the New Zealand Society for Earthquake Engineering*, 43(3):202–212, 2010.

[16] J Borzouie, JG Chase, GA MacRae, GW Rodgers, and GC Clifton. Spectral assessment of the effects of base flexibility on seismic demands of a structure. *Advances in Civil Engineering*, 2016:1–8, 2016.

[17] Mariantonieta Gutierrez Soto and Hojjat Adeli. Tuned mass dampers. *Archives of Computational Methods in Engineering*, 20: 419–431, 2013.

[18] Robert J McNamara. Tuned mass dampers for buildings. *Journal of the Structural Division*, 103(9):1785–1798, 1977.

[19] Said Elias and Vasant Matsagar. Wind response control of tall buildings with a tuned mass damper. *Journal of Building Engineering*, 15:51–60, 2018.

[20] Amir M Kaynia, Daniele Veneziano, and John M Biggs. Seismic effectiveness of tuned mass dampers. *Journal of the Structural Division*, 107(8):1465–1484, 1981.

[21] John R Sladek and Richard E Klingner. Effect of tuned-mass dampers on seismic response. *Journal of structural engineering*, 109(8):2004–2009, 1983.

[22] Jonathan Salvi and Egidio Rizzi. Optimum tuning of tuned mass dampers for frame structures under earthquake excitation. *Structural Control and Health Monitoring*, 22(4):707–725, 2015.

[23] Sajal Kanti Deb. Seismic base isolation–an overview. *Current Science*, pages 1426–1430, 2004.

[24] James M Kelly. Aseismic base isolation: review and bibliography. *Soil Dynamics and earthquake engineering*, 5(4):202–216, 1986.

[25] Vincenzo Piluso, Alessandro Pisapia, Elide Nastri, and Rosario Montuori. Ultimate resistance and rotation capacity of low yielding high hardening aluminium alloy beams under non-uniform bending. *Thin-Walled Structures*, 135:123–136, 2019.

[26] Fabio Freddi, Christoforos A Dimopoulos, and Theodore L Karavasilis. Experimental evaluation of a rocking damage-free steel column base with friction devices. *Journal of Structural Engineering*, 146(10):04020217, 2020.

[27] Antonella B. Francavilla, Massimo Latour, Vincenzo Piluso, and Gianvittorio Rizzano. Design criteria for beam-to-column connections equipped with friction devices. *Journal of Constructional Steel Research*, 172:106240, September 2020. doi: 10.1016/j.jcsr. 2020.106240.

[28] Massimo Latour, Vincenzo Piluso, and Gianvittorio Rizzano. Experimental analysis of innovative dissipative bolted double split tee beam-to-column connections. *Steel Construction*, 4(2):53–64, June 2011. doi: 10.1002/stco.201110009.

[29] Vincenzo Piluso, Gianvittorio Rizzano, Massimo Latour, Rosario Montuori, Elide Nastri, Antonella B. Francavilla, Sabatino Di Benedetto, Raffaele Landolfo, Luis Simões da Silva, Aldina Santiago, Ana Francisca Santos, Jean-Pierre Jaspart, and Jean-Francois Demonceau. *Seismic design of steel structures with FREE from DAMage steel connections*. ECCS – European Convention for Constructional Steelwork, 2022. ISBN 978-92-9147-182-9.

[30] Sabatino Di Benedetto, Antonella Bianca Francavilla, Massimo Latour, Vincenzo Piluso, and Gianvittorio Rizzano. Experimental response of a large-scale two-storey steel building equipped with low-yielding friction joints. *Soil Dynamics and Earthquake Engineering*, 152:107022, January 2022. doi: 10.1016/j.soildyn.2021.107022.

[31] Ricky WK Chan and Faris Albermani. Experimental study of steel slit damper for passive energy dissipation. *Engineering Structures*, 30(4):1058–1066, 2008.

[32] Sang-Hoon Oh, Young-Ju Kim, and Hong-Sik Ryu. Seismic performance of steel structures with slit dampers. *Engineering structures*, 31(9):1997–2008, 2009.

[33] Seyed Masoud Sajjadi Alehashem, Ali Keyhani, and Hassan Pourmohammad. Behavior and performance of structures equipped with adas & tadas dampers (a comparison with conventional structures). In *The 14th World Conference on Earthquake Engineering*, volume 12, page 17, 2008.

[34] Rodrigo Thiers-Moggia and Christian Málaga-Chuquitaype. Seismic protection of rocking structures with inerters. *Earthquake Engineering & Structural Dynamics*, 48(5):528–547, 2019.

[35] Robert Tremblay, L Poncet, P Bolduc, R Neville, and R DeVall. Testing and design of buckling restrained braces for canadian application. In *Proceedings of the 13th world conference on Earthquake Engineering*, pages 1–6, 2004.

[36] Qiang Xie. State of the art of buckling-restrained braces in asia. *Journal of constructional steel research*, 61(6):727–748, 2005.

[37] Alessandro Zona and Andrea Dall'Asta. Elastoplastic model for steel buckling-restrained braces. *Journal of Constructional Steel Research*, 68(1):118–125, 2012.

[38] Shawn Kiggins and Chia-Ming Uang. Reducing residual drift of buckling-restrained braced frames as a dual system. *Engineering Structures*, 28(11):1525–1532, 2006.

[39] Fabio Freddi, Enrico Tubaldi, Alessandro Zona, and Andrea Dall'Asta. Seismic performance of dual systems coupling moment-resisting and buckling-restrained braced frames. *Earthquake Engineering & Structural Dynamics*, 50(2):329–353, 2021.

[40] Sabau GA, Poljansek M, Taucer F, Pegon P, Molina Ruiz FJ, Tirelli D, Viaccoz B, Stratan A, Dubina D, and Ioan Chesoan A. Seismic engineering research infrastructures for european synergies. full-scale experimental validation of a dual eccentrically braced frame with removable links (duarem). Scientific analysis or review LB-NA-27030-EN-N, Luxembourg (Luxembourg), 2014.

[41] Cheng Fang, Canxing Qiu, Wei Wang, and M Shahria Alam. Self-centering structures against earthquakes: A critical review. *Journal of Earthquake Engineering*, pages 1–36, 2023.

[42] Shuling Hu, Wei Wang, M Shahria Alam, and Ke Ke. Life-cycle benefits estimation of self-centering building structures. *Engineering Structures*, 284:115982, 2023.

[43] Hesam Azizi, Jamal Ahmadi, and Mahdi Eghbali. Study on self-centering mechanism of different yield strength hybrid buckling restrained braces. *Journal of Constructional Steel Research*, 210: 108068, 2023.

[44] A. Plumier, C. Doneux, and Carlo Andrea Castiglioni. *Two innovations for earthquake-resistant design: the INERD project: final report*. Number 22044 in European Commission, Directorate General for Research and Innovation. Publications Office, 2006. ISBN 978-92-79-01694-3.

[45] Carlo Andrea Castiglioni, Georgia Dougka, D. Kalteziotis, Ph. Karydakis, L. Calado, A. Kanyilmaz, I. Vayas, J.M. Proença, Benno Hoffmeister, T. Rauert, Danai Dimakogianni, and M. Espinha. *Dissipative devices for seismic-resistant steel frames (Fuseis)*. European Commission, Directorate General for Research and Innovation. Publications Office, LU, 2013.

[46] I Vayas. Innovative dissipative (inerd) pin connections for seismic resistant braced frames. page 12.

[47] Georgia Dougka, Danai Dimakogianni, and Ioannis Vayas. Innovative energy dissipation systems (fuseis 1-1) — experimental analysis. *Journal of Constructional Steel Research*, 96:69–80, may 2014. doi: 10.1016/j.jcsr.2014.01.003.

[48] Danai Dimakogianni, Georgia Dougka, and Ioannis Vayas. Seismic behavior of frames with innovative energy dissipation systems (fuseis 1-1). *Earthquakes and Structures*, 6(5):561–580, May 2014. doi: 10.12989/EAS.2014.6.5.561.

[49] Alper Kanyilmaz, Milot Muhaxheri, and Carlo Andrea Castiglioni. Influence of repairable bolted dissipative beam splices (structural fuses) on reducing the seismic vulnerability of steel-concrete composite frames. *Soil Dynamics and Earthquake Engineering*, 119:281–298, April 2019. doi: 10.1016/j.soildyn.2019.01.007.

[50] Alper Kanyilmaz and Carlo Andrea Castiglioni. Dissipable proposal - fully dissipative and easily repairable devices for resilient buildings with composite steel-concrete structures. Technical report, Politecnico di Milano, Instituto Superior Tecnico Lisboa, University of Trento, RWTH Aachen University, National Technical University of Athens NTUA, RINA Consulting - Centro Sviluppo Materiali SpA, University of Pisa, SOFMAN, 2017.

[51] JM Proencca, Luis Calado, Alper Kanyilmaz, et al. Dissipative replaceable bracing connections (drbrc) for earthquake protection of steel and composite structures. *Steel and Composite Structures*, 46(2):237–252, 2023.

[52] Roberto Andreotti, Giulia Giuliani, Nicola Tondini, and Oreste S. Bursi. Hybrid simulation of a partial-strength steel–concrete composite moment-resisting frame endowed with hysteretic replaceable beam splices. *Earthquake Engineering & Structural Dynamics*, 52(1):51–70, January 2023. doi: 10.1002/eqe.3744.

[53] Roberto Andreotti, Giulia Giuliani, and Nicola Tondini. Experimental analysis of a full-scale steel frame with replaceable dissipative connections. *Journal of Constructional Steel Research*, 208:108036, 2023. doi: 10.1016/j.jcsr.2023.108036.

[54] Masayoshi Nakashima. Hybrid simulation: An early history. *Earthquake Engineering & Structural Dynamics*, 49(10):949–962, August 2020. doi: 10.1002/eqe.3274.

[55] Giuseppe Abbiati, Oreste S. Bursi, Philippe Caperan, Luigi
Di Sarno, Francisco Javier Molina, Fabrizio Paolacci, and Pierre
Pegon. Hybrid simulation of a multi-span rc viaduct with plain
bars and sliding bearings. *Earthquake Engineering & Structural
Dynamics*, 44(13):2221–2240, October 2015. doi: 10.1002/eqe.
2580.

[56] Maikol Del Carpio Ramos, Gilberto Mosqueda, and M. Javad
Hashemi. Large-Scale Hybrid Simulation of a Steel Moment
Frame Building Structure through Collapse. *Journal of Struc-
tural Engineering*, 142(1):04015086, January 2016. doi: 10.1061/
(ASCE)ST.1943-541X.0001328.

[57] Sabatino Di Benedetto, Antonella Bianca Francavilla, Massimo
Latour, Giovanni Ferrante Cavallaro, Vincenzo Piluso, and Gi-
anvittorio Rizzano. Pseudo-dynamic testing of a full-scale two-
storey steel building with RBS connections. *Engineering Struc-
tures*, 212:110494, June 2020. doi: 10.1016/j.engstruct.2020.
110494.

[58] Nicola Tondini, Giuseppe Abbiati, Luca Possidente, and Bozidar
Stojadinovic. Hybrid simulation applied to fire testing: a newly
conceived numerical framework. page 11, 2016.

[59] Ana Sauca, Thomas Gernay, Fabienne Robert, Nicola Tondini,
and Jean-Marc Franssen. Hybrid fire testing: Discussion on sta-
bility and implementation of a new method in a virtual environ-
ment. *Journal of Structural Fire Engineering*, 9(4):319–341, Oc-
tober 2018. doi: 10.1108/JSFE-01-2017-0017.

[60] Patrick Covi, Giuseppe Abbiati, Nicola Tondini, Oreste S Bursi,
and Božidar Stojadinović. A static solver for hybrid fire simula-
tion based on model reduction and dynamic relaxation. The Uni-
versity of Queensland, Brisbane, Australia, December 2020.

[61] Oreste S Bursi and David Wagg. *Modern Testing Techniques for
Structural Systems*. Dynamics and Control. 2008. ISBN 978-3-
211-09445-7.

[62] O.S. Bursi, L. He, A. Bonelli, and P. Pegon. Novel generalized-α
methods for interfield parallel integration of heterogeneous struc-
tural dynamic systems. *Journal of Computational and Applied
Mathematics*, 234(7):2250–2258, August 2010. doi: 10.1016/j.
cam.2009.08.082.

[63] Bin Wu, Guoshan Xu, Qianying Wang, and Martin S Williams. Operator-splitting method for real-time substructure testing. *Earthquake Engineering & Structural Dynamics*, 35(3):293–314, 2006.

[64] C. P. Lamarche, A. Bonelli, O. S. Bursi, and R. Tremblay. A rosenbrock-w method for real-time dynamic substructuring and pseudo-dynamic testing. *Earthquake Engineering & Structural Dynamics*, 38(9):1071–1092, July 2009. doi: 10.1002/eqe.884.

[65] Giuseppe Abbiati, Igor Lanese, Enrico Cazzador, Oreste S. Bursi, and Alberto Pavese. A computational framework for fast-time hybrid simulation based on partitioned time integration and state-space modeling. *Structural Control and Health Monitoring*, 26 (10), October 2019. doi: 10.1002/stc.2419.

[66] Kenneth E. Jansen, Christian H. Whiting, and Gregory M. Hulbert. A generalized-α method for integrating the filtered navier–stokes equations with a stabilized finite element method. *Computer Methods in Applied Mechanics and Engineering*, 190 (3-4):305–319, October 2000. doi: 10.1016/S0045-7825(00) 00203-6.

[67] Charbel Farhat and Francois-Xavier Roux. A method of finite element tearing and interconnecting and its parallel solution algorithm. *International Journal for Numerical Methods in Engineering*, 32(6):1205–1227, October 1991. doi: 10.1002/nme. 1620320604.

[68] A. Bonelli, O. S. Bursi, L. He, G. Magonette, and P. Pegon. Convergence analysis of a parallel interfield method for heterogeneous simulations with dynamic substructuring. *International Journal for Numerical Methods in Engineering*, 75(7):800–825, August 2008. doi: 10.1002/nme.2285.

[69] Inc. Wolfram Research. Mathematica, 2022. URL https://www.wolfram.com/mathematica.

[70] Roberto Andreotti. *Dissipative replaceable components and impact mass dampers towards more resilient earthquake-resistant steel structures*. PhD thesis, Doctoral School in Civil, Environmental and Mechanical Engineering - University of Trento, 2022.

[71] Ioannis Vayas, editor. *Innovative anti-seismic devices and systems: INNOSEIS Project RFCS-02-2015*. ECCS, Zürich, 1st edition edition, 2017. ISBN 978-92-9147-136-2.

[72] (European Committee for Standardization) CEN. Eurocode 8: Design of structures for earthquake resistance - part 3: Assessment and retrofitting of buildings, 2005.

[73] Frank McKenna, GL Fenves, and M Scott. Opensees: Open system for earthquake engineering simulation. university of california berkeley, 2006. URL `opensees.berkeley.edu`.

[74] Y.-K. Wen. Method for random vibration of hysteretic systems. *Journal of Engineering Mechanics Division*, 102(2):249–263, 1976. doi: https://doi.org/10.1061/JMCEA3.0002106.

[75] Alessio Bonelli and Oreste S. Bursi. Predictor-corrector procedures for pseudo-dynamic tests. *Engineering Computations*, 22 (7):783–834, October 2005. doi: 10.1108/02644400510619530.

[76] Jian Li, Billie F. Spencer, Amr S. Elnashai, and Brian M. Phillips. Substructure Hybrid Simulation with Multiple-Support Excitation. *Journal of Engineering Mechanics*, 138(7):867–876, July 2012. doi: 10.1061/(ASCE)EM.1943-7889.0000394.

[77] R. Bouc. Forced vibrations of mechanical systems with hysteresis. Prague, 1967.

[78] (European Committee for Standardization) CEN. Eurocode 3: Design of steel structures - part 1-8: Design of joints, 2005.

[79] C Chisari, Antonella Bianca Francavilla, Massimo Latour, Vincenzo Piluso, and C Amadio. Critical issues in parameter calibration of cyclic models for steel members. *Engineering Structures*, (132):123–138, 2017. doi: 10.1016/j.engstruct.2016.11.030.

[80] Michael Smith. *ABAQUS/Standard User's Manual, Version 6.9*. Dassault Systémes Simulia Corp, United States, 2009.

[81] A Kanyilmaz, A Kondratenko, CA Castiglioni, L Calado, J Proenca, H Mouzakis, L Panoutsopoulou, I Psycharis, P Thanopoulos, K Papavasileiou, M Sofras, N Tondini, R Andreotti, G Giuliani, A Bonelli, OS Bursi, C Vuclu, M Pinkawa,

B Hoffmeister, E Rocco, L Napolano, G Zilli, S Caprili, I Panzera, and F Mattei. Fully dissipative and easily repairable components for resilient buildings with composite steel-concrete structures. Technical report, Politecnico di Milano, Instituto Superior Técnico Lisboa, National Technical University of Athens, Masina Team SA – SOFMAN, Universita' degli studi di Trento, RWTH Aachen University, Rina Consulting-Centro Sviluppo Materiali SPA, Universita' di Pisa, 2022.

[82] Luís Calado, Jorge M. Proença, Miguel Espinha, and Carlo A. Castiglioni. Hysteretic behaviour of dissipative bolted fuses for earthquake resistant steel frames. *Journal of Constructional Steel Research*, 85:151–162, 2013. doi: https://doi.org/10.1016/j.jcsr.2013.02.016.

[83] Computers and Structures Inc. Sap2000 integrated software for structural analysis and design. URL `https://www.csiamerica.com/products/sap2000`.

[84] (European Committee for Standardization) CEN. Eurocode 8: Design of structures for earthquake resistance - part 1: general rules, seismic actions and rules for buildings. working draft., 2018.

[85] Marius Pinkawa, Helen Bartsch, Simon Schaffrath, Benno Hoffmeister, and Markus Feldmann. Seismic design of steel frames with fuseis beam link energy dissipation systems. pages 878–890, Rhodes Island, Greece, 2017. ISBN 978-618-82844-3-2. doi: 10.7712/120117.5463.18111.

[86] F. Flores, F. Charney, and D. Lopez-Garcia. The influence of gravity column continuity on the seismic performance of special steel moment frame structures. *Journal of Constructional Steel Research*, 118:217–230, March 2016. doi: 10.1016/j.jcsr.2015.11.010.

[87] Miroslav Pastor, Michal Binda, and Tomáš Harčarik. Modal assurance criterion. *Procedia Engineering*, 48:543–548, 2012. doi: 10.1016/j.proeng.2012.09.551.

[88] Marius Pinkawa, Cristian Vulcu, Benno Hoffmeister, and Markus Feldmann. Optimization of dissipative replaceable link frames by elastic high-strength steel coupling beams. pages 3127–3143, Athens, Greece, 2020. doi: 10.47964/1120.9256.20314.

[89] Cristian Vulcu, Marius Pinkawa, and Benno Hoffmeister. Comparison of the seismic performance of conventional moment resisting frames and innovative dissipative replaceable link frames. page 8, Timisoara, Romania, May 2022.

[90] CEN. *EN 1994-1 - Eurocode 4: Design of composite steel and concrete structures - part 1.1: general rules, and rules for buildings*. CEN - European Committee of Standardization, Bruxelles, 2004.

[91] The MathWorks Inc. Matlab version: 9.13.0 (r2022b), 2022. URL `https://www.mathworks.com`.

[92] Giuseppe Abbiati. *Dynamic substructuring of complex hybrid systems based on time-integration, model reduction and model identification techniques*. PhD thesis, University of Trento, 2014.

[93] (European Committee for Standardization) CEN. Eurocode 3: Design of steel structures - part 1-1: General rules and rules for buildings, 2005.

[94] FEDERAL EMERGENCY. *Prestandard and commentary for the seismic rehabilitation of buildings - FEMA 356*, volume 356. 2000.

[95] Simulink Documentation. Simulation and model-based design, 2020. URL `https://www.mathworks.com/products/simulink.html`.

[96] O. S. Bursi and P.-S. B. Shing. Evaluation of some implicit time-stepping algorithms for pseudodynamic tests. *Earthquake Engineering & Structural Dynamics*, 25(4):333–355, April 1996. doi: 10.1002/(SICI)1096-9845(199604)25:4<333:: AID-EQE548>3.0.CO;2-M.

[97] M. Pecce and F. Rossi. The experimental behavior and simple modeling of joints in composite mrfs. *Engineering Structures*, 105:249–263, December 2015. ISSN 01410296. doi: 10.1016/j. engstruct.2015.09.042.

[98] A.K. Chopra. *Dynamics of Structures: Theory and Applications to Earthquake Engineering*. Always learning. Pearson, 2017. ISBN 9780134555126.

[99] Luis F Ibarra, Ricardo A Medina, and Helmut Krawinkler. Hysteretic models that incorporate strength and stiffness deterioration. *Earthquake engineering & structural dynamics*, 34(12): 1489–1511, 2005.

[100] Dimitrios G. Lignos and Helmut Krawinkler. A database in support of modeling of component deterioration for collapse prediction of steel frame structures. In *Structural Engineering Research Frontiers*, pages 1–12, Long Beach, California, United States, October 2007. American Society of Civil Engineers. doi: 10.1061/40944(249)31.

[101] Dimitrios G Lignos and Helmut Krawinkler. Deterioration modeling of steel components in support of collapse prediction of steel moment frames under earthquake loading. *Journal of Structural Engineering*, 137(11):1291–1302, 2011. doi: https://doi.org/10.1061/(ASCE)ST.1943-541X.0000376.

[102] Dimitrios G Lignos, Helmut Krawinkler, and Andrew S Whittaker. Prediction and validation of sidesway collapse of two scale models of a 4-story steel moment frame. *Earthquake Engineering & Structural Dynamics*, 40(7):807–825, 2011. doi: https://doi.org/10.1002/eqe.1061.

[103] AMERICAN INSTITUTE OF STEEL CONSTRUCTION. *Seismic Provisions for Structural Steel Buildings - AISC 341-10.* 2010.

[104] Dimitrios Vamvatsikos and C. Allin Cornell. Incremental dynamic analysis. *Earthquake Engineering & Structural Dynamics*, 31(3): 491–514, March 2002. doi: 10.1002/eqe.141.

[105] Jack W. Baker. Efficient analytical fragility function fitting using dynamic structural analysis. *Earthquake Spectra*, 31(1):579–599, February 2015. doi: 10.1193/021113EQS025M.

[106] Peer ground motion database. `https://ngawest2.berkeley.edu/`, 2013.

[107] Russo E Luzi L, Puglia R and ORFEUS WG5. Engineering strong motion database. *Istituto Nazionale di Geofisica e Vulcanologia. Observatories and Research Facilities for European Seismology*, 2016. doi: 10.13127/ESM.

[108] C. Allin Cornell, Fatemeh Jalayer, Ronald O. Hamburger, and
Douglas A. Foutch. Probabilistic Basis for 2000 SAC Federal
Emergency Management Agency Steel Moment Frame Guide-
lines. *Journal of Structural Engineering*, 128(4):526–533, April
2002. doi: 10.1061/(ASCE)0733-9445(2002)128:4(526).

The Thesis discusses the experimental campaign conducted on steel frames equipped with easily repairable seismic dissipative devices. The work has been developed in the framework of the European project DISSIPABLE founded by RFCS. The tested frames were equipped with three innovative components: dissipative replaceable link frames (DRLF), dissipative replaceable beam splices (DRBeS), and dissipative replaceable braced connections (DRBrC). The tests were conducted at different levels of seismic intensity, and hybrid simulation and substructuring techniques were used to reduce costs while providing accurate results. The laboratory tests demonstrated that the dissipative replaceable components effectively protected the critical parts of the frames, dissipating energy and remaining elastic at the design limit state. The damaged components were easily replaced, and the results matched the predictions of numerical models. Additionally, a novel algorithmic correction was implemented in the simulation process and validated. High-fidelity models of the structures were developed and calibrated based on the experimental results, allowing for the derivation of experimentally calibrated fragility curves. The comparison between frames equipped with the seismic dissipative components and a reference model showed that the former can be repaired more quickly and are more cost-effective at the same probability of failure.

Giulia Giuliani.